SUBSPACE BASED RADAR SIGNAL PROCESSING METHODS FOR ARRAY TAPERING AND SIDELOBE BLANKING

A THESIS SUBMITTED TO
THE GRADUATE SCHOOL OF NATURAL AND APPLIED SCIENCES
OF
MIDDLE EAST TECHNICAL UNIVERSITY

BY

DOĞANCAN DİNLER

IN PARTIAL FULFILLMENT OF THE REQUIREMENTS
FOR
THE DEGREE OF MASTER OF SCIENCE
IN
ELECTRICAL AND ELECTRONICS ENGINEERING

SEPTEMBER 2017

Approval of the thesis:

SUBSPACE BASED RADAR SIGNAL PROCESSING METHODS FOR ARRAY TAPERING AND SIDELOBE BLANKING

submitted by **DOĞANCAN DİNLER** in partial fulfillment of the requirements for the degree of **Master of Science in Electrical and Electronics Engineering Department, Middle East Technical University** by,

Prof. Dr. Gülbin Dural Ünver
Dean, Graduate School of **Natural and Applied Sciences** ____

Prof. Dr. Tolga Çiloğlu
Head of Department, **Electrical and Electronics Engineering** ____

Prof. Dr. Çağatay Candan
Supervisor, **Electrical and Electronics Eng., METU** ____

Prof. Dr. Sencer Koç
Co-supervisor, **Electrical and Electronics Eng., METU** ____

Examining Committee Members:

Prof. Dr. Ali Özgür Yılmaz
Electrical and Electronics Engineering Dept., METU ____________

Prof. Dr. Çağatay Candan
Electrical and Electronics Engineering Dept., METU ____________

Prof. Dr. Sencer Koç
Electrical and Electronics Engineering Dept., METU ____________

Prof. Dr. Orhan Arıkan
Electrical and Electronics Engineering Dept., BILKENT ____________

Assist. Prof. Dr. M. Gökhan Güvensen
Electrical and Electronics Engineering Dept., METU ____________

Date: ____________

I hereby declare that all information in this document has been obtained and presented in accordance with academic rules and ethical conduct. I also declare that, as required by these rules and conduct, I have fully cited and referenced all material and results that are not original to this work.

Name, Last Name: DOĞANCAN DİNLER

Signature :

ABSTRACT

SUBSPACE BASED RADAR SIGNAL PROCESSING METHODS FOR ARRAY TAPERING AND SIDELOBE BLANKING

DİNLER, DOĞANCAN
M.S., Department of Electrical and Electronics Engineering
Supervisor : Prof. Dr. Çağatay Candan
Co-Supervisor : Prof. Dr. Sencer Koç

September 2017, 85 pages

The discretization of the signal impinging on several hundreds, even thousands, of receiving elements has become a common problem in modern phased array radar systems along with the developments in the digital signal processing. The spatial and temporal processing of such large dimensional data is too challenging for all steps of signal processing. This thesis is focused on the subspace methods that making the processing of the full dimensional data feasible at reduced dimensions. The first objective of the thesis is to develop a proper subspace such that the essence of the signal coming from a predefined sector is captured at reduced dimensions. To realize that aim, eigenvector and Fourier bases of the sector are studied and evaluation of these bases are performed considering the detection and parameter estimation performances. The second objective is to apply some conventional radar signal processing methods, namely array tapering and sidelobe blanking, at reduced dimensions. The main contributions are subspace construction and reduced dimensional implementations of array tapering and sidelobe blanking. Numerical results are provided to evaluate the performance of suggested methods in different scenarios.

Keywords: Radar Signal Processing, Dimension Reduction, Beamforming, Sub-

space Based Detection and Parameter Estimation, Array Tapering, Sidelobe Blanking

ÖZ

DİZİ PENCERELEME VE YAN HÜZME KARARTMA İÇİN ALT UZAY TABANLI RADAR SİNYAL İŞLEME METOTLARI

DİNLER, DOĞANCAN
Yüksek Lisans, Elektrik ve Elektronik Mühendisliği Bölümü
Tez Yöneticisi : Prof. Dr. Çağatay Candan
Ortak Tez Yöneticisi : Prof. Dr. Sencer Koç

Eylül 2017 , 85 sayfa

Sayısal sinyal işleme alanındaki gelişmelerle birlikte, yüzlerce hatta binlerce elemanlı modern radar sistemlerinin aldığı sinyalin ayrıklaştırılması yaygın bir problem haline gelmiştir. Bu kadar büyük boyutlu verilerin uzamsal ve zamansal olarak işlenmesi çok zorlayıcıdır. Bu tezde, tüm elemanlardaki verilerin işlenmesini azaltılmış boyutlarda mümkün kılan alt uzay metotları üzerine odaklanılmıştır. Tezin ilk amacı, önceden tanımlanmış bir sektörden gelen sinyalin özünün azaltılmış boyutlarda yakalanacağı bir alt uzay geliştirmektir. Bu amacı gerçekleştirmek için, sektörün özvektör ve Fourier bazlarına çalışılmış, tespit ve parametre kestirim performansları dikkate alınarak bu metotların değerlendirilmesi gerçekleştirilmiştir. Tezin ikinci amacı, dizi pencereleme ve yan hüzme karartma gibi bazı radar sinyal işleme yöntemlerinin indirilmiş boyutlarda uygulanmasıdır. Tezin sağladığı katkılar alt uzay oluşturma ve alt uzayda dizi pencereleme ve yan hüzme karartma uygulamalarını gerçekleştirmektir. Yöntemlerin performansları farklı senaryolar altında sayısal sonuçlar sağlanarak değerlendirilmiştir.

Anahtar Kelimeler: Radar Sinyal İşleme, Boyut Azaltma, Hüzme Oluşturma, Alt Uzayda Tespit ve Parametre Kestirimi, Dizi Pencereleme, Yan Hüzme Karartma

To my family

ACKNOWLEDGMENTS

I would like to express my sincere gratitude to Prof. Çağatay Candan and Prof. Sencer Koç for their progressive guidance, encouragement and advice throughout my study. Their immense knowledge and experience have been the assets for the completion of this thesis.

I would also like to thank my friends and colleagues, especially Yankı Aslan, for their continuous support and understanding which kept me motivated even in the tough moments.

I would like to indicate my appreciation to ASELSAN Inc. for the supports and opportunities on academic studies.

I would also like to thank TÜBİTAK for their financial support during my research.

I could not end this section without conveying my gratitude to our current as well as former RSP group members Prof. Yalçın Tanık, Prof. Fatih Canatan who although no longer with us, Prof. Mete Severcan, Prof. Mustafa Kuzuoğlu, Assist. Prof. Gökhan Güvensen, Assist. Prof. Sevinç Figen Öktem and Seçil Özdemir, for their fruitful comments and discussions during our project meetings.

Finally yet importantly, I would like to thank my family for their help, support and trust they have given me all along my life.

TABLE OF CONTENTS

LIST OF TABLES

TABLES

LIST OF FIGURES

FIGURES

LIST OF ABBREVIATIONS

AWGN	Additive White Gaussian Noise
CRB	Cramer Rao Lower Bound
CRI	Coherent Repeater Interference
DFT	Discrete Fourier Transform
DKLT	Discrete Karhuenen Loeve Transform
DPSS	Discrete Prolate Spheroidal Sequence
INR	Interference to Noise Ratio
LCMP	Linear Constrained Minimum Power
LCMV	Linear Constrained Minimum Variance
MPDR	Minimum Power Distortionless Response
MSE	Mean Square Error
MUSIC	Multiple Signal Classification
MVDR	Minimum Variance Distortionless Response
NLI	Noise Like Interference
PSL	Peak to Sidelobe
SLB	Sidelobe Blanker
SLC	Sidelobe Canceller
SNR	Signal to Noise Ratio
ULA	Uniform Linear Array

CHAPTER 1

INTRODUCTION

1.1 Motivation

Until the mid-1960s, the digital signal processing methods had been used for data simulation and offline analysis of recorded data since the digital processors of time had limited potentials. Indeed, analog systems had typically been preferred to implement the signal processing algorithms in real time applications. Fortunately, the rapid evolution of digital computing has made it possible to use digital signal processing in real time applications. Radar was one of the applications that has taken advantage of the digital signal processing and its knowledge base has grown rapidly by employing more sophisticated signal processing algorithms.

Recent technological developments have enabled radar systems having several hundreds of elements to sample the continuous time signals impinging on the array. Unfortunately, further processing of large amount of data collected at every second is very challenging even with the today's technology. Therefore, the sampled data needs a dimension reduction pre-processing stage before further processing. With the evolution of the digital systems, the concept of dimension reduction has become a common topic in several fields. However, very few of the studies under the title of reduced dimension beamspace processing, exist in the literature. The reduced dimension beamspace processing is defined as creating a set of non-adaptive beams to enable further processing of the signal at the elements of a very large array in [1]. Hence, it is preferred to use the phrase ‘beamspace processing’, compatible with its analog counterpart, (for compactness, the phrase ‘reduced dimension’ is removed from the expression) as a short hand title for dimension reduction operation in the scope of this thesis.

The motivation of the thesis is to transform the original signal to the reduced dimensions and then apply radar signal processing methods on the reduced dimensional signal. The concept of beamspace processing is considered with the specifications of a phased array radar having hundreds of elements. Moreover, implementation of spatial domain operations, namely tapering and sidelobe blanking, into beamspace processing is not present in the radar literature, to the best of our knowledge. Therefore, it is intended to fill this gap by examining the applicability of these methods in beamspace.

In this thesis, a digital phased array radar is used to study spatial signal processing techniques. As in a typical radar scenario, a predefined region of the space, also referred as the sector, is assumed to be illuminated by a transmitter. The main objective is to design a practical receiver that is able to capture the essence of the information in the predefined region and present a way to apply some required spatial operations, namely tapering and sidelobe blanking on the reduced dimensional signal.

1.2 Literature Review

In this section of the thesis, the studies in the literature regarding with the subspace based array processing, array tapering, and sidelobe blanking are presented, in the given order.

In [2], the large dimensional data was mapped into lower dimensional space to reduce the computational burden. The detection performance of the subspace was considered as a design criterion and the average signal to noise ratio (SNR) was aimed to be maximized. It was found that transformation matrix that constructs the subspace consists of the significant eigenvectors of the covariance matrix belonging to a desired region of the space. Besides, subspace versions of some direction finding algorithms, namely Multiple Signal Classification (MU-

SIC) and Min Norm, were presented. It was shown that due to the decrease in noise power, dimension reduction improves the performance of both parameter estimation algorithms.

In [3], sensitivity of eigenvector source localization method on errors, which is caused by modelling the noise space with insufficient precision, was aimed to be decreased by employing discrete prolate spheroidal sequences (DPSS) as spatial filters to reduce dimensions. DPSS was introduced in [4] and power maximizing property of DPSS was demonstrated on band-limited time series. In fact, DPSS was achieved by maximizing the energy confined within the bandwidth of the signal. This power maximization property of DPSS was used in [3] and it was shown that DPSS corresponds to the eigenvectors of the sector covariance matrix with the largest eigenvalues.

In [1], various topics on the dimension reduction were brought together and beamspace processing was discussed in detail. The parameter estimation, i.e. direction finding, performances of subspace methods were evaluated. Both adaptive and non-adaptive subspace methods were introduced. Adaptive methods were investigated under the eigenspace concept. It was explained that eigenspace is constructed by eigendecomposing the data covariance matrix calculated using received data at the array elements. In other words, on the fly calculated eigenvectors were used to map the received data into the eigenspace. Another work on the adaptive subspace construction was also conducted in [5]. Some direction finding algorithms, namely deterministic maximum likelihood, ESPRIT, and multidimensional signal subspace method, were formulated in a subspace that was created by the eigenvectors of the data covariance matrix. In a typical radar scenario, however, the receiver pattern is steered towards the sector illuminated by the transmitter pattern. In other words, sector (the region of the space that is to be interested in) is given as a priori information as in this thesis. Therefore, non-adaptive methods, which assume that the sector is completely known, are employed instead of the adaptive methods.

A similar work to this thesis was conducted in [6]. In order to reduce computational requirements, dimension reduction was performed as a preliminary process in the element space. Design of the subspace was performed by maximizing the parameter estimation performance of the array. In addition, the number of the reduced space dimensions was determined considering the parameter estimation performance as well. It was stated that there is not a certain rule to decide the number of subspace dimensions. It can be chosen according to the maximum possible computational burden that can be handled. In this thesis, the detection ability of the subspace is considered to be more important than the parameter estimation accuracy because the direction finding cannot be performed without detecting the target in typical radars. Therefore, the number of subspace dimension is determined based on the achievable SNR instead of the parameter estimation accuracy, which is in contrast to [6].

The Cramer Rao Lower Bound (CRB) derivation of random signals for parameter estimation problem was presented in [7]. In this thesis, a subspace CRB formulation is achieved using the derivation in [7]. CRB analyses of beamspace methods were also performed in [1]. However, they were compared with element space performance for a limited number of scenarios. Furthermore, a certain rule was not defined to determine the number of reduced space dimension. As expected, analyses indicate that an increase in subspace dimension results in better estimation accuracy. It was also quantitatively illustrated that a proper subspace operation can provide almost the same parameter estimation performance with the element space performance in [1].

In [8], minimizing the average error between true covariance matrix and the implied structured covariance model was taken as the criterion for subspace construction. It was found that the transformation matrix, which projects data onto the subspace, is formed by the eigenvectors corresponding to the largest eigenvalues of the sector covariance matrix. Additionally, under the name of partially adaptive beamforming, derivation of adaptive beamforming weights, which are used to eliminate interferers, were examined for reduced dimensions. A similar work was also conducted in [1]. Element space interference suppression methods, namely Minimum Power Distortionless Response (MPDR), Linear Constrained Minimum Variance (LCMV) and Linear Constrained Minimum Power (LCMP) beamformers were implemented in subspace. Results demonstrate that interference cancellation can be realized in reduced dimensions with an appropriate selection of beamspace matrices. Another subspace design that takes interference cancellation into consideration was recently studied in [9]. Generalized eigenvector subspace was found as the optimum solution for several criteria such as mutual information preserving, reconstruction error minimizing, and detection probability maximizing. It is worthy of note that when there are no interferers, generalized eigenvector weights equal to the eigenvectors of the sector covariance matrix. Therefore, the detection performance of this method can be considered as similar to the methods derived in [3],[2], [1], and [8] in the absence of interferers. Besides, it can be computationally complex to implement generalized eigenvector method for large dimensional arrays. Therefore, it is not studied in the scope of this thesis.

It has to be underlined that described works from literature are closely related to each other and there is not a variety of sources on the comparison of different subspace performances. Moreover, there have not been any guideline for how much dimension have to be reduced in order to provide a predetermined detection loss in subspace.

Besides the optimum eigenvector beamformer, which has been widely used in the literature, detection and parameter estimation performance of another subspace construction method, namely conventional Discrete Fourier Transform (DFT) beamformer, is studied in this thesis. An analogous work that investigate the relation between eigenvector and DFT bases on time signals were presented in [10] under the name of Discrete Karhuenen Loeve Transform and Discrete Fourier Transform. It was shown that DKLT is the most efficient representation when the dimension is reduced. It was also noted that DKLT is practically equivalent to DFT if the correlation function becomes smaller in magnitude within a short interval or observation interval is long with respect to the reciprocal of process bandwidth (assuming a low pass process with well defined bandwidth). This fact can be interpreted as DFT and eigenvector beamformers are expected to achieve similar performance results if the magnitude of the sector covariance matrix's off-diagonal elements decay rapidly enough.

As very well appreciated, the low sidelobe patterns provide better performance in case of high clutter and interferer scearios and can be provided by array tapering which has been studied by a number of authors, [11], [1], [12], [13], and [14]. In these sources, tapered array patterns were illustrated for different tapering classes yet there have not been any guideline for application of tapering in the subspace. In [1], tapered beamspace matrix was suggested to achieve subspace with low sidelobes; however, the concept was not covered in detail. To clarify, the effect of tapering on the number of dimension or detection performance of such system was not examined. The concept of tapering and dimension reduction were discussed recently in [15]. A novel tapering method, tapering after dimension reduction, was suggested and detection performance of the proposed method was analyzed. It was seen that tapering can be performed in reduced dimensions contrary to the conventional approach that is to apply tapering to the full dimensional array. Nevertheless, the relation between tapering and number of dimensions were not investigated in [15].

In order to prevent the acquisition of targets and pulsed interference originating in the antenna sidelobe, a sidelobe blanker system is typically aplied, [16]. The basic sidelobe blanker system was introduced for a conventional two channel system, namely main and auxiliary channel, and probability of detection formula was derived according to the proposed structure. It was stated that the trade-off between detecting targets in the mainlobe and in the sidelobe can be handled with a high gain sidelobe suppression antenna. This challenge was also expressed in [17]. In this thesis, a novel auxiliary pattern design which is easily implemented after beamspace processing is proposed to overcome this trade-off.

In [16], the nonfluctuating target model was used to evaluate the SLB performance. In [18], the performance evaluations of SLB structure was extended to the fluctuating targets. In [12], the SLB system was investigated in detail and various sources on SLB system were gathered. Furthermore, the probability of blanking the target in the mainlobe and the probability of blanking the interferer in a sidelobe were derived for Swerling-0 model. Performance of the SLB structure was evaluated for different scenarios. In [19], previous work in [12] was improved by deriving the closed-form expression of the probability of blanking the interferer in a sidelobe for Swerling-1 model.

A more recent work on SLB was presented in [20]. In this study, an optimal SLB detector was developed. The performance of the proposed detector was compared with the conventional SLB structure for Swerling-1 and Swerling-0 models. This study showed that the conventional SLB structure results in a similar performance with the optimal detector. In this thesis, a practically implementable conventional SLB structure is to be investigated. Moreover, application of SLB structure in reduced dimensions is to be presented that is perceived as a gap in the literature.

1.3 Organization

The remaining part of the thesis is organized as follows:

Chapter 2 introduces signal models that is used throughout the thesis. The matrices are represented in bold and uppercase letters whereas vectors are represented in bold and lowercase letters.

The working principle of the beamspace processing is explained in Chapter 3. Here, two beamspace construction methods, namely eigenvector and DFT beamformers are introduced. Moreover, the detection and parameter estimation, i.e. direction finding, performances of the methods are compared. Besides, determining the number of reduced dimensions is studied in Chapter 3.

In Chapter 4, implementation of dimension reduction with tapering is studied in detail. Two methods, namely tapering before dimension reduction and tapering after dimension reduction, are examined. In addition, a brief comparison of these methods is given considering their detection performances.

In Chapter 5, a well-known operation, sidelobe blanking, is studied. A novel approach to the design of the auxiliary antenna pattern is presented. The advantages of the approach are demonstrated. Besides, the design of the sidelobe blanker in the beamspace is performed.

In Chapter 6, concluding remarks on the design of a properly functioning subspace for the spatial operations mentioned in Chapters 4 and 5 are presented.

CHAPTER 2

ARRAY SIGNAL MODEL

Arrays are used to filter the signals in the spatial domain in order to suppress the interfering signals and reduce the background noise. The design of arrays depends on the geometry and placement of the elements. The geometry of the array is classified in [1] as follows:

- Linear
- Planar
- Volumetric

In this thesis, linear arrays are utilized. The placement of the elements in linear arrays can be classified as follows:

- Uniform
- Non-Uniform
- Random

A uniform linear array (ULA) consisting of equally spaced elements is used for this thesis work. A sample array geometry for a ULA of N elements is shown in Figure 2.1.

Array elements are placed with an equal distance, d, as shown in Figure 2.1. In this thesis, the coordinate system of interest is taken as spherical coordinates as visualized in Figure 2.2.

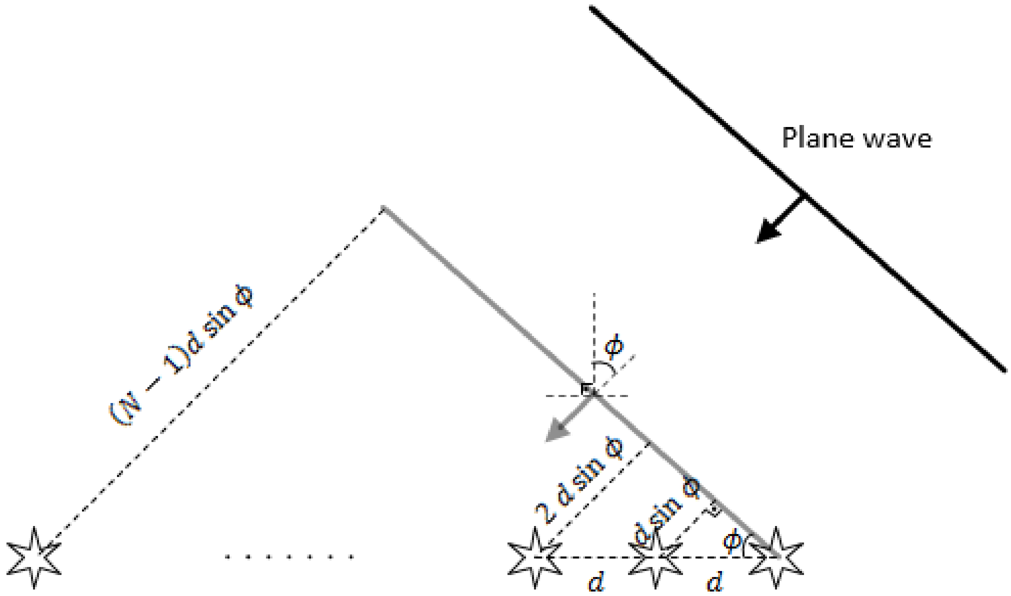

Figure 2.1: ULA with N elements.

The signal model is established considering the case of a single target whose echo impinges upon an array of N elements. Received signals at the output of each array elements are denoted by $\mathbf{y}(t)$, where t refers the time at which the received signals are sampled. Array output, for narrowband impinging signals, can be expressed as

$$\mathbf{y}(t) \;=\; \mathbf{a}(\phi)\mathrm{s}(t) \;+\; \mathbf{n}(t) \tag{2.1}$$

where $\mathbf{y}(t) \;=\; \begin{bmatrix} y_1 \; y_2 \; y_3 \; \ldots \; y_N \end{bmatrix}^{\mathbf{T}} \in C^{N\times 1}$, $\mathbf{a}(\phi) \in C^{N\times 1}$ is the response of the array for the source coming from ϕ, $s(t) \in C^{1\times 1}$ is the complex amplitude of the echo signal at time t and $\mathbf{n}(t)$ is the additive white gaussian noise. Array steering vector, $\mathbf{a}(\phi)$, can be modeled as

$$\mathbf{a}(\phi) \;=\; \begin{bmatrix} e^{-j2\pi f\tau_1} \\ e^{-j2\pi f\tau_2} \\ \vdots \\ e^{-j2\pi f\tau_N} \end{bmatrix} \tag{2.2}$$

where f is the carrier frequency, τ_i is the time delay corresponding to the time of arrival at the i^{th} sensor. With the far field assumption, τ_i can be expressed

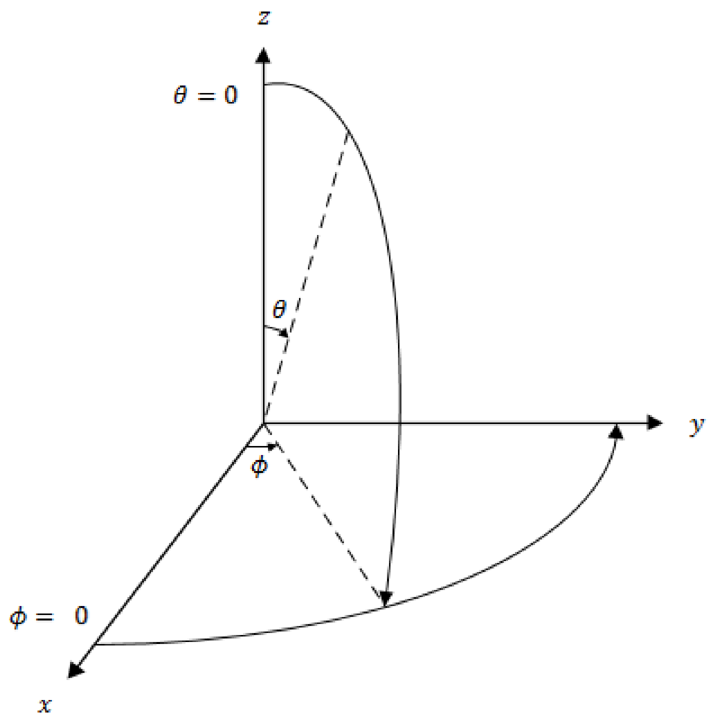

Figure 2.2: Representation of spherical coordinates.

as follows:

$$\tau_i = -\frac{x_i \sin\theta \cos\phi + y_i \sin\theta \sin\phi + z_i \cos\theta}{c}. \tag{2.3}$$

where c refers to the speed of light, x_i, y_i, and z_i denote the positions of the elements in the array, θ and ϕ represent the elevation and the azimuth angles given in Figure 2.2.

In this thesis, the array is placed on the x-y plane. This means that θ in Figure 2.2 is taken as 90°. The elements of the array are placed on y-axis as shown in Figure 2.3.

Considering Figure 2.3 and inserting (2.3) into (2.2), $\mathbf{a}(\phi)$ can be rewritten as

$$\mathbf{a}(\phi) = \begin{bmatrix} e^{j\frac{2\pi}{\lambda}\left(-\frac{N-1}{2}\right)d\sin\phi} \\ e^{j\frac{2\pi}{\lambda}\left(-\frac{N-3}{2}\right)d\sin\phi} \\ \vdots \\ e^{j\frac{2\pi}{\lambda}\left(\frac{N-1}{2}\right)d\sin\phi} \end{bmatrix} \tag{2.4}$$

where $\lambda = f \,/\, c$. Array steering vector, $\mathbf{a}$, can also be represented by defining

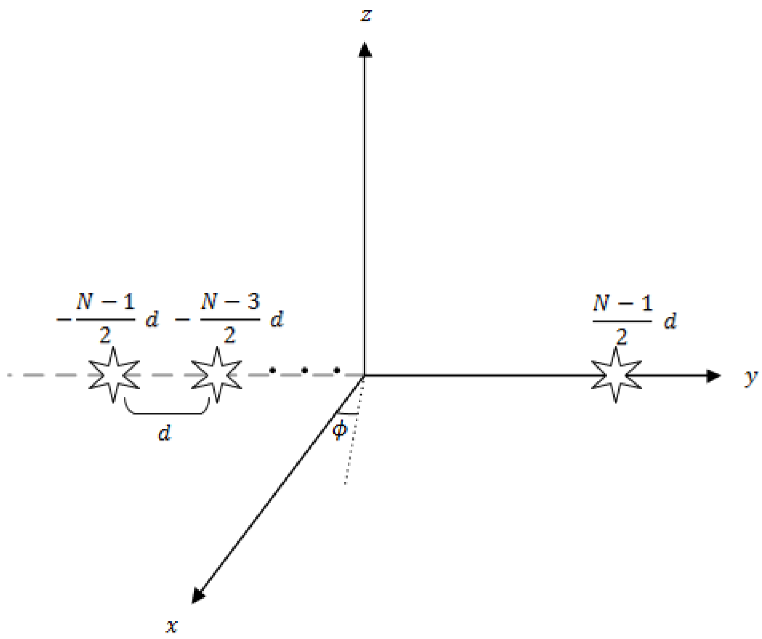

Figure 2.3: Array placed on y-axis.

the cosine terms with respect to each axis as

$$
\begin{aligned}
u_x &= \sin\theta \ \cos\phi, \\
u_y &= \sin\theta \ \sin\phi, \\
u_z &= \cos\theta,
\end{aligned}
\tag{2.5}
$$

and employing the wavenumber which is defined as

$$
\mathbf{k} = -\frac{2\pi}{\lambda}\begin{bmatrix} \sin\theta \ \cos\phi \\ \sin\theta \ \sin\phi \\ \cos\theta \end{bmatrix} = -\frac{2\pi}{\lambda}\begin{bmatrix} u_x \\ u_y \\ u_z \end{bmatrix} = -\frac{2\pi}{\lambda}\ \mathbf{u}. \tag{2.6}
$$

The resultant array steering vector, $\mathbf{a}$, as a function of wavenumber, $\mathbf{k}$, can be written as

$$
\mathbf{a}(\mathbf{k}) = \begin{bmatrix} e^{-j\mathbf{k}^T\mathbf{p}_1} \\ e^{-j\mathbf{k}^T\mathbf{p}_2} \\ \vdots \\ e^{-j\mathbf{k}^T\mathbf{p}_3} \end{bmatrix}, \tag{2.7}
$$

where $\mathbf{p}$ refers to the positions of the elements.

$$\mathbf{p}_i = \begin{bmatrix} x_i \\ y_i \\ z_i \end{bmatrix}. \tag{2.8}$$

Considering the fact that the array is placed on the y-axis as indicated in Figure 2.3, array steering vector, $\mathbf{a}$ can be rewritten as a function of the wavenumber as follows:

$$\mathbf{a}(\mathrm{k_y}) = \begin{bmatrix} e^{-j\mathrm{k_y}\left(-\frac{N-1}{2}\right)d} \\ e^{-j\mathrm{k_y}\left(-\frac{N-3}{2}\right)d} \\ \vdots \\ e^{-j\mathrm{k_y}\left(\frac{N-1}{2}\right)d} \end{bmatrix}, \tag{2.9}$$

where $\mathrm{k_y}$ is the resultant wavenumber shown as

$$\mathrm{k_y} = -\frac{2\pi}{\lambda} \sin\phi. \tag{2.10}$$

In order to further simplify the array steering vector, $\mathbf{a}$, it is useful to define

$$\psi = -\mathrm{k_y}\, d. \tag{2.11}$$

Inserting (2.11) into (2.9), $\mathbf{a}$ can be rewritten as

$$\mathbf{a}(\psi) = \begin{bmatrix} e^{j\psi\left(-\frac{N-1}{2}\right)} \\ e^{j\psi\left(-\frac{N-3}{2}\right)} \\ \vdots \\ e^{j\psi\left(\frac{N-1}{2}\right)} \end{bmatrix}. \tag{2.12}$$

In this thesis, assumptions that the signal model is based on are defined as follows:

1. The targets are assumed to be located in the far field of the array. Under the far field assumption, signal impinging on the array propagates as a plane wave as shown in Figure 2.1.

2. The narrowband assumption is defined in [21] as the time variations in the amplitude and phase modulations of the signal being larger than the time delay between any two sensors. Under the narrowband assumption, signal impinging on the array can be written as

$$\mathrm{s}(t - \tau_k) \;\approx\; \mathrm{s}(t)\; e^{-j\omega_c \tau_k}, \tag{2.13}$$

   where ω_c denotes the center frequency.

3. The center frequency of the signal, ω_c, is assumed to be known.

4. The number of elements in the array is taken as 100.

5. The array and the targets are placed on the x-y plane. This means that $\theta = 90°$.

6. Interelement spacing between the elements of the array is defined as $d = \lambda \, / \, 2$.

7. Noise is assumed to be independent identically distributed circularly symmetric complex zero mean Gaussian distributed.

CHAPTER 3

REDUCED DIMENSION BEAMSPACE PROCESSING

Reduced dimension beamspace processing decreases the rank of the processor, which is necessary in systems with the large number of antenna elements in order to detect and estimate the signal of interest. In other words, beamspace processing is used to construct a subspace in reduced dimension which is spanned by columns of the beamspace matrix (range space of the matrix). In [2], the beamspace processing is defined as a linear transformation from element space into a lower dimensional space. In this thesis, beamspace is formed by projecting the received array signal onto the beamspace matrix generated using presumed steering vectors .

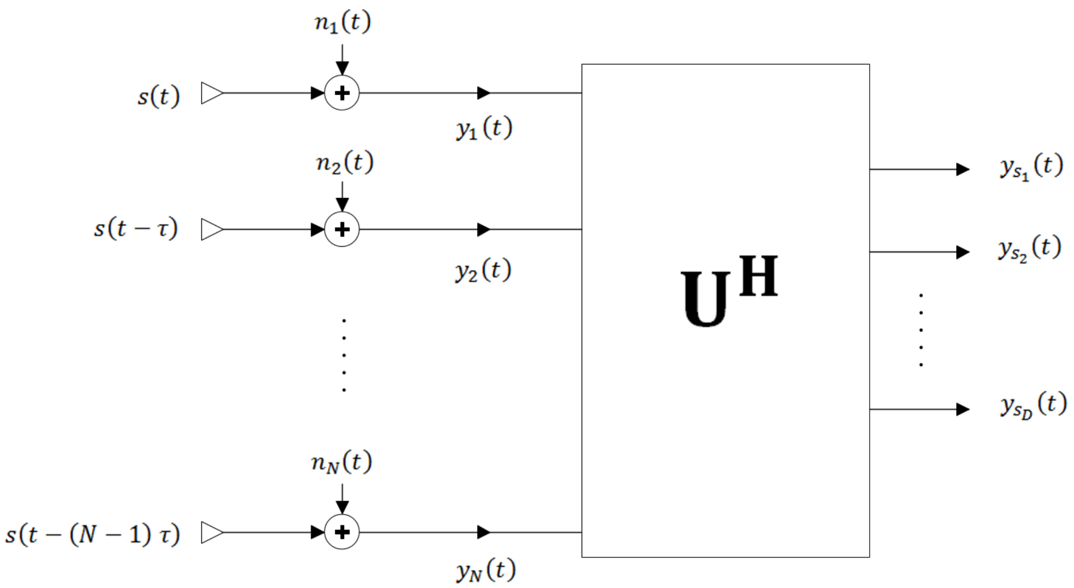

Figure 3.1: Beamspace processing chain.

In Figure 3.1, beamspace processing is illustrated, where $\mathbf{U}$ is the beamspace matrix of size $N \times D$, N is the number of elements in the array, D is the dimension of the reduced space, $s(t)$ is the echo signal impinging on the array, $(i-1)\tau$ is the time delay of the received signal at i^{th} array element, $n_i(t)$ is the additive white gaussian noise (AWGN) at the i^{th} array element, $y_i(t)$ is the i^{th} element's noisy signal and $y_{s_i}(t)$ is the i^{th} beamspace signal.

The columns of $\mathbf{U}$ are assumed to be orthonormal, if not they can be orthonormalized with the operation of

$$\mathbf{U} \leftarrow \mathbf{U}\,(\mathbf{U^H}\,\mathbf{U})^{-1/2}. \tag{3.1}$$

In (3.2), $\mathbf{y}(t)$ and $\mathbf{y_s}(t)$ correspond to the received signal impinging on the array under AWGN and the beamspace signal achieved after beamspace processing, respectively

$$\mathbf{y_s}(t) = \mathbf{U^H}\,\mathbf{y}(t). \tag{3.2}$$

Presumed steering vectors are utilized to generate the projection matrix, $\mathbf{U}$. They are chosen according to the sector that is, in the scope of this thesis work, defined as the region in space where all the signals of interest are contained.

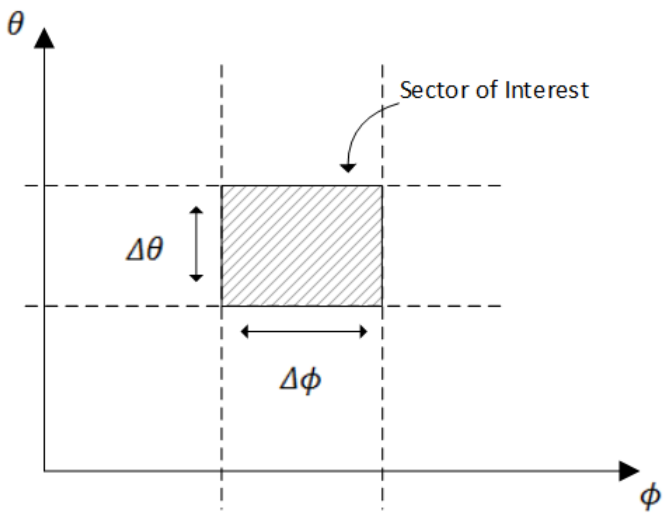

Figure 3.2: Illustration of a 2D sector of interest (Despite the use of one dimensional sector throughout the thesis, 2D sector is preferred to be shown in terms of the intelligibility of the sector concept).

The main advantages of beamspace processing are listed in [22] as: reducing data, increasing computational efficiency and reducing noise. However, if beamspace processing is not performed properly, detection and estimation performance of the array might become poorer. For clarity, information related with the signal of interest might be lost after dimension reduction.

In this chapter, dimension reduction methods, which are referred as eigenvector beamformer and DFT beamformer, are presented. To evaluate the detection performance of these methods, SNR is considered as a beamspace design objective. Moreover, in order to demonstrate that whether the proposed methods provide good statistics for the parameter estimation, i.e. direction finding, problem or not, Cramer Rao Lower Bounds (CRB) of beamspace methods are compared with the element space ones. Depending on these two objectives, the importance of choosing a proper beamspace matrix and criteria for determining the number of beamspace dimensions are discussed.

3.1 Eigenvector Beamformer

The beamspace matrix, $\mathbf{U}$ of size $N \times D$, is used to form a beamspace for sector angles from ϕ_{min} to ϕ_{max}

$$\mathbf{U} \;=\; [\ \mathbf{u}_1\ \mathbf{u}_2 ...\ \mathbf{u}_D\ ] \tag{3.3}$$

where, $\mathbf{u}_i$ is the i^{th} column of $\mathbf{U}$, the beamspace matrix. Then, the ratio of the energy represented in the i^{th} beam in the sector to the energy of the i^{th} beam in space is defined as

$$\begin{aligned} c_i &= \frac{\int_{\phi_{min}}^{\phi_{max}} |\mathbf{u}_i^{\mathbf{H}}\ \mathbf{a}(\phi)|^2 d\phi}{\int_{-\pi/2}^{\pi/2} |\mathbf{u}_i^{\mathbf{H}}\ \mathbf{a}(\phi)|^2 d\phi}\ , \\ &= \frac{\mathbf{u}_i^{\mathbf{H}}\ \int_{\phi_{min}}^{\phi_{max}} \mathbf{a}(\phi)\mathbf{a}^{\mathbf{H}}(\phi) d\phi\ \mathbf{u}_i}{\mathbf{u}_i^{\mathbf{H}}\ \int_{-\pi/2}^{\pi/2} \mathbf{a}(\phi)\mathbf{a}^{\mathbf{H}}(\phi) d\phi\ \mathbf{u}_i}. \end{aligned} \tag{3.4}$$

To simplify the integral calculations, ψ-space, which was explained in Chapter 2, is used for the representation of the steering vectors. Therefore, (3.4) can be rewritten as

$$c_i = \frac{\mathbf{u}_i^{\mathbf{H}}\ \int_{\psi_{min}}^{\psi_{max}} \mathbf{a}(\psi)\mathbf{a}^{\mathbf{H}}(\psi) d\psi\ \mathbf{u}_i}{\mathbf{u}_i^{\mathbf{H}}\ \int_{-\pi}^{\pi} \mathbf{a}(\psi)\mathbf{a}^{\mathbf{H}}(\psi) d\psi\ \mathbf{u}_i}. \tag{3.5}$$

The integral in the numerator of (3.5) can be expressed as

$$\mathbf{R} = \frac{1}{\psi_{max} - \psi_{min}} \int_{\psi_{min}}^{\psi_{max}} \mathbf{a}(\psi)\mathbf{a}^{\mathbf{H}}(\psi) d\psi. \tag{3.6}$$

where $\mathbf{R}$ is the covariance matrix of the sector. The element corresponding the m^{th} row and n^{th} column of the covariance matrix can be found as

$$\begin{aligned}
\mathbf{R}_{mn} &= \frac{1}{\psi_{max} - \psi_{min}} \int_{\psi_{min}}^{\psi_{max}} e^{j\psi m} e^{-j\psi n} d\psi \\
&= \frac{1}{\psi_{max} - \psi_{min}} \int_{\psi_{min}}^{\psi_{max}} e^{j\psi(m-n)} d\psi \\
&= \frac{1}{\psi_{max} - \psi_{min}} \frac{e^{j\psi_{max}(m-n)} - e^{j\psi_{min}(m-n)}}{j(m-n)} \\
&= \frac{1}{\psi_{max} - \psi_{min}} e^{j\psi_{max}(m-n)} \frac{1 - e^{-j(\psi_{max}-\psi_{min})(m-n)}}{j(m-n)} \\
&= \frac{1}{\psi_{max} - \psi_{min}} e^{\frac{j(\psi_{max}+\psi_{min})(m-n)}{2}} \frac{2\sin\left[\frac{(\psi_{max}-\psi_{min})}{2}(m-n)\right]}{m-n}.
\end{aligned} \tag{3.7}$$

Assuming a symmetric sector of interest, implying that $\psi_{max} = -\psi_{min}$, the sector covariance matrix can be further simplified as,

$$\mathbf{R}_{mn} = \begin{cases} \frac{1}{2\psi_{max}} \frac{2\sin\left[\psi_{max}(m-n)\right]}{m-n}, & \text{if } m \neq n, \\ 1, & \text{if } m = n. \end{cases} \tag{3.8}$$

Using (3.8), the integral in the denominator of (3.5) results in

$$\int_{-\pi}^{\pi} \mathbf{a}(\psi)\mathbf{a}^{\mathbf{H}}(\psi) d\psi = 2\pi\mathbf{I}. \tag{3.9}$$

Considering (3.9), the denominator of (3.5) is calculated as $2\pi\mathbf{u}_i^{\mathbf{H}}\mathbf{u}_i$. Combining (3.9) and (3.6), (3.5) can be rewritten as

$$c_i = \frac{\left(\psi_{max} - \psi_{min}\right) \mathbf{u}_i^{\mathbf{H}} \ \mathbf{R}\mathbf{u}_i}{2\pi\mathbf{u}_i^{\mathbf{H}}\mathbf{u}_i}. \tag{3.10}$$

c_i is desired to be maximized subject to the orthonormality condition:

$$\underset{\mathbf{u}_i}{\text{maximize}} \ c_i \quad \text{subject to} \quad \mathbf{u}_i^{\mathbf{H}}\mathbf{u}_i = 1. \tag{3.11}$$

Equation (3.11), a well known optimization problem, results in $\mathbf{u}_i$ being the eigenvector of R corresponding to the i^{th} largest eigenvalue.

This approach was first encountered in [4] under the name of discrete prolate spheroidal functions (DPSS). Mathematical properties of DPSS was discussed in detail and utilized to represent time series with a finite index set in [4]. In [3], DPSS was applied to array processing for the first time [1] and used in order to form beamspace as shown in this section.

The same beamspace matrix, **U**, can also be achieved by maximizing the SNR of an angular sector at the output of a spatial filter.

Assume that the sources are taken as uniformly distributed throughout the sector with the probability density function (pdf) given in Figure 3.3.

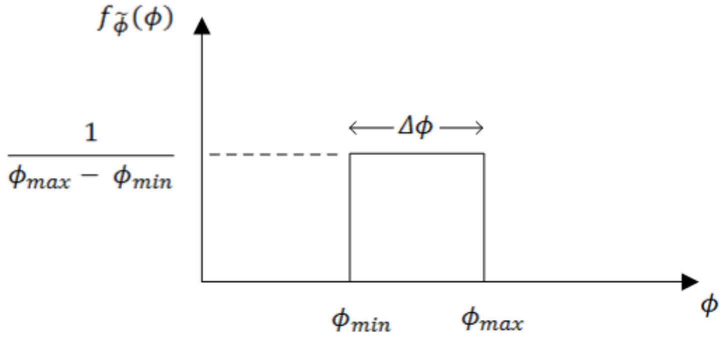

Figure 3.3: Probability density function of the sources in space

The beamformer operation can be defined as in Figure 3.4.

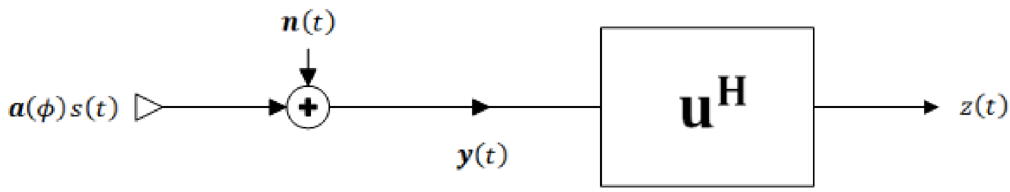

Figure 3.4: The spatial filtering operation

The beamforming process shown in Figure 3.4 can be formulated as

$$\begin{aligned} \mathbf{y}(t) &= \mathbf{a}(\phi)\mathrm{s}(t) + \mathbf{n}(t), \\ \mathrm{z}(t) &= \mathbf{u}^{\mathbf{H}}\, \mathbf{y}(t), \\ &= \mathbf{u}^{\mathbf{H}}\mathbf{a}(\phi)\mathrm{s}(t) + \mathbf{u}^{\mathbf{H}}\mathbf{n}(t), \end{aligned} \tag{3.12}$$

where $\mathrm{s}(t)$ is the received echo signal, $\mathbf{a}(\phi)$ is the steering vector of the source, $\mathbf{n}(t)$ is the additive white gaussian noise (AWGN) at the antenna elements, $\mathbf{y}(t)$

is the received signal at the antenna elements under AWGN, $\mathbf{u}$ is the spatial filter, and z(t) is the output of the beamformer.

The SNR at the output of the beamformer can be written as

$$\begin{aligned}
\mathrm{SNR}(\phi) &= \frac{E\Big\{\big(\mathbf{u}^H\ \mathbf{a}(\phi)\ \mathrm{s}(t)\big)\ \big(\mathbf{u}^H\ \mathbf{a}(\phi)\ \mathrm{s}(t)\big)^H\Big\}}{E\Big\{\big(\mathbf{u}^H\ \mathbf{n}(t)\big)\ \big(\mathbf{u}^H\ \mathbf{n}(t)\big)^H\Big\}}, \\
&= \frac{\mathbf{u}^H\ \mathbf{a}(\phi)\ E\Big\{\mathrm{s}(t)\ \mathrm{s}(t)^{\mathbf{H}}\Big\}\mathbf{a}(\phi)^{\mathbf{H}}\ \mathbf{u}}{\mathbf{u}^{\mathbf{H}}\ E\Big\{\mathbf{n}(t)\ \mathbf{n}(t)^{\mathbf{H}}\Big\}\mathbf{u}}, \qquad (3.13)\\
&= \frac{\sigma_s^2}{\sigma_n^2}\ \frac{\mathbf{u}^H\ \mathbf{a}(\phi)\ \mathbf{a}(\phi)^{\mathbf{H}}\ \mathbf{u}}{\mathbf{u}^{\mathbf{H}}\ \mathbf{u}},
\end{aligned}$$

where expectation, $E\{.\}$, is taken over the time, t, σ_s^2 and σ_n^2 are the variances of the signal and noise, respectively. The SNR value in (3.13) is calculated for a specific angular point, ϕ, in space. In order to design a spatial filter for the sector, the pdf of the sources, given in Figure 3.4, is needed to be considered. Taking expectation of the point SNR expression over ϕ yields the concept of average signal to noise ratio, $\mathrm{SNR}_{\mathrm{avg}}$, of the sector,

$$\begin{aligned}
\mathrm{SNR}_{\mathrm{avg}} &= E\left\{\frac{\sigma_s^2}{\sigma_n^2}\ \frac{\mathbf{u}^H\ \mathbf{a}(\phi)\ \mathbf{a}(\phi)^{\mathbf{H}}\ \mathbf{u}}{\mathbf{u}^{\mathbf{H}}\ \mathbf{u}}\right\}, \\
&= \frac{\sigma_s^2}{\sigma_n^2}\ \frac{\mathbf{u}^H\ E\Big\{\mathbf{a}(\phi)\ \mathbf{a}(\phi)^{\mathbf{H}}\Big\}\mathbf{u}}{\mathbf{u}^{\mathbf{H}}\ \mathbf{u}}, \qquad (3.14)
\end{aligned}$$

where,

$$\begin{aligned}
E\Big\{\mathbf{a}(\phi)\ \mathbf{a}(\phi)^{\mathbf{H}}\Big\} &= \int_{-\pi/2}^{\pi/2} \mathbf{a}(\phi)\mathbf{a}^{\mathbf{H}}(\phi) f_\phi(\phi) d\phi, \\
&= \frac{1}{\phi_{max} - \phi_{min}} \int_{\phi_{min}}^{\phi_{max}} \mathbf{a}(\phi)\mathbf{a}^{\mathbf{H}}(\phi) d\phi. \qquad (3.15)
\end{aligned}$$

The expectation of the steering vectors over ϕ results in the sector covariance matrix, $\mathbf{R}$, as found in (3.6). Inserting (3.15) into (3.14), $\mathrm{SNR}_{\mathrm{avg}}$ can be rewritten as

$$\mathrm{SNR}_{\mathrm{avg}} = \frac{\sigma_s^2}{\sigma_n^2}\ \frac{\mathbf{u}^H\ \mathbf{R}\ \mathbf{u}}{\mathbf{u}^{\mathbf{H}}\ \mathbf{u}}. \qquad (3.16)$$

In order to find the appropriate spatial weights, $\mathbf{u}$, $\mathrm{SNR}_{\mathrm{avg}}$ value is to be maximized as

$$\underset{\mathbf{u}}{\text{maximize}}\ \mathrm{SNR}_{\mathrm{avg}} \quad \text{subject to} \quad \mathbf{u}^{\mathbf{H}}\ \mathbf{u} = 1. \qquad (3.17)$$

Equation (3.17) is the same constrained maximization problem with the one derived in (3.11). The solution of this problem is the eigenvector of the sector covariance matrix corresponding to the largest eigenvalue. If more than one beamformer, $\mathbf{u}_i$, are to be used, then they will be equal to the eigenvectors of the sector covariance matrix corresponding to the i^{th} maximum eigenvalues.

Thus far, the same beamspace matrix is found by maximizing the ratio of the energy of the sector to the energy in the space and maximizing the average SNR of a sector at the output of a beamformer. Now, the beamspace matrix will be calculated by applying the optimal representation property of the Discrete Karhuenen Loeve Transform (DKLT), [10], into the array signal processing.

Assume that an orthonormal set of functions is generated to form a beamspace

$$\mathbf{a}(\phi) = \sum_{i=0}^{N-1} \kappa_i \mathbf{u}_i, \tag{3.18}$$

where $\mathbf{a}(\phi)$ is the true steering vector involved in the sector, κ_i is the ith coefficient in the expansion and $\mathbf{u}_i$ is the i^{th} basis function.

Due to the practical concerns, D out of N many basis vectors are used to represent the subspace

$$\tilde{\mathbf{a}}(\phi) = \sum_{i=0}^{D-1} \kappa_i \mathbf{u}_i, \tag{3.19}$$

where $\tilde{\mathbf{a}}(\phi)$ refers to the approximate steering vector. The error, due to approximating an N dimensional space with D basis functions, can be defined as,

$$\mathbf{e}(\phi) = \mathbf{a}(\phi) - \tilde{\mathbf{a}}(\phi) = \sum_{i=D}^{N-1} \kappa_i \mathbf{u}_i, \tag{3.20}$$

where $\mathbf{e}(\phi)$ is the error vector. In order to find an appropriate set of basis functions, mean square error (MSE) is to be minimized

$$\begin{aligned} \epsilon &= E\Big\{ \mathbf{e}(\phi)^{\mathbf{H}}\, \mathbf{e}(\phi) \Big\}, \\ &= E\Bigg\{ \Big(\sum_{i=D}^{N-1} \kappa_i \mathbf{u}_i \Big)^{\mathbf{H}} \Big(\sum_{j=D}^{N-1} \kappa_j \mathbf{u}_j \Big) \Bigg\}, \end{aligned} \tag{3.21}$$

where ϵ is the MSE. It is worth to underline that the basis functions to be obtained by means of minimizing MSE can also be achieved by minimizing the average energy of the error in the sector. Using the orthonormality property of the basis functions, expression in (3.21) can be simplified as

$$\epsilon = \sum_{i=D}^{N-1} E\Big\{|\kappa_i|^2\Big\}, \tag{3.22}$$

where

$$\kappa_i = \mathbf{u}_i^{\mathbf{H}} \, \mathbf{a}(\phi). \tag{3.23}$$

In (3.23), orthonormality property of the basis functions is used. Inserting (3.23) into (3.22), MSE can be rewritten as

$$\begin{aligned} \epsilon &= \sum_{i=D}^{N-1} E\Big\{ \left(\mathbf{u}_i^{\mathbf{H}} \, \mathbf{a}(\phi)\right) \left(\mathbf{u}_i^{\mathbf{H}} \, \mathbf{a}(\phi)\right)^{\mathbf{H}} \Big\}, \\ &= \sum_{i=D}^{N-1} \mathbf{u}_i^{\mathbf{H}} \, E\Big\{ \mathbf{a}(\phi) \, \mathbf{a}(\phi)^{\mathbf{H}} \Big\} \, \mathbf{u}_i, \\ &= \sum_{i=D}^{N-1} \mathbf{u}_i^{\mathbf{H}} \, \mathbf{R} \, \mathbf{u}_i, \end{aligned} \tag{3.24}$$

The expectation operation over ϕ gives the sector covariance matrix, $\mathbf{R}$, as found in (3.15). Instead of minimizing MSE, ϵ, $1 - \epsilon$ expression can be maximized. Therefore, the expression to be maximized will be

$$1 - \epsilon = \sum_{i=0}^{D-1} \mathbf{u}_i^{\mathbf{H}} \, \mathbf{R} \, \mathbf{u}_i. \tag{3.25}$$

The maximization of (3.25) is a well known constrained maximization problem and results in $\mathbf{u}_i$ being the eigenvector of $\mathbf{R}$ corresponding to the i^{th} largest eigenvalue. Thus, the basis functions of the beamspace corresponds to the eigenvectors of the sector covariance matrix with D largest eigenvalues.

The algorithm steps of constructing a beamspace matrix are as follows:

1. Define a sector in space.

2. Calculate sector covariance matrix,$\mathbf{R}$.

3. Eigendecompose $\mathbf{R}$.
4. Choose D many eigenvectors corresponding the largest eigenvalues.
5. Construct beamspace matrix of size $N \times D$ by defining these eigenvectors as the columns of that matrix.

3.2 DFT Beamformer

DFT beams, also known as the conventional beams, are the most commonly used spatial filters in array signal proccessing. DFT beams correspond to the array steering vectors defined in (2.4). These beams provide a channel steered towards a desired point in space to maximize SNR [22].

The algorithm steps of constructing a beamspace matrix are as follows:

1. Define a sector in space.
2. Choose D many angles in the sector with equal intervals.
3. Construct D many DFT beams steered towards the selected angles.
4. Construct beamspace matrix of size $N \times D$ by defining these DFT beams as the columns of that matrix.
5. Orthonormalize the beamspace matrix using (3.1).

3.3 On the Relation Between Eigenvector and DFT Beamformers

For a proper illustration of the behaviour and a better understanding on the characteristics of the eigenvector beamformer, the following case is studied.

Assume that only a single point in space is taken as the signal of interest; and therefore, sector is defined as that point. Then, the covariance matrix of the sector is calculated as

$$\mathbf{R} \; = \; \mathbf{a}(\phi_0) \; \mathbf{a}^{\mathbf{H}}(\phi_0). \tag{3.26}$$

If D is choosen as 1, $\mathbf{U}$ has only one column and the resultant pattern is shown in Figure 3.5. The resultant pattern exactly corresponds to the pattern of the array

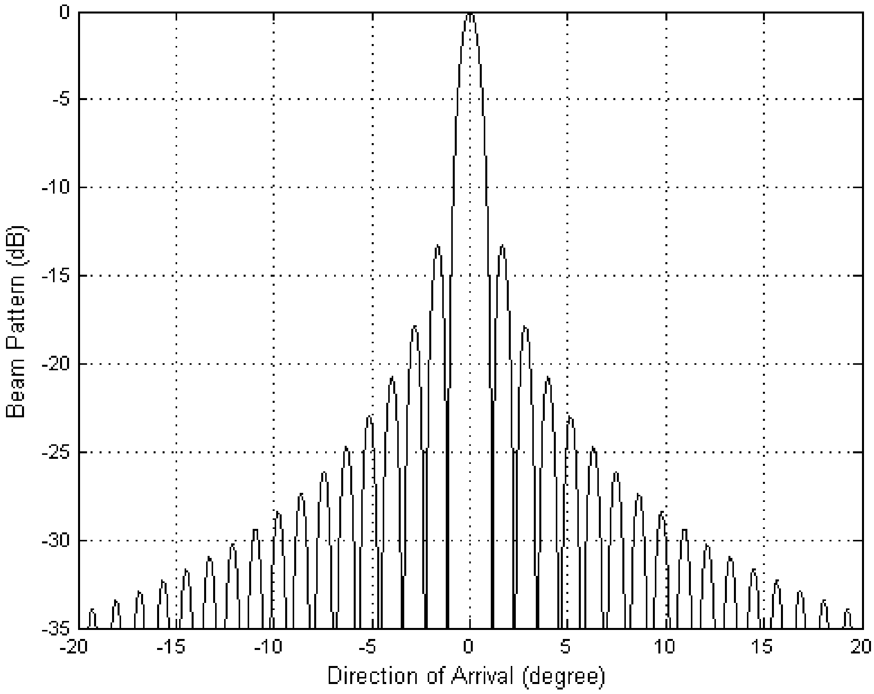

Figure 3.5: The first beamspace beam pattern of the array.

steered towards that direction. This phenomenon can also be seen from Mercer's theorem. According to the Mercer's theorem, a symmetric, non-negative definite matrix can be expanded as:

$$\mathbf{R} = \sum_{k=1}^{\infty} \lambda_k \, \boldsymbol{\zeta}_k \, \boldsymbol{\zeta}_k^{\mathbf{H}} \tag{3.27}$$

where λ_k and ζ_k refer the k^{th} eigenvalue and corresponding eigenfunction, respectively. In fact, $\boldsymbol{\zeta}$ represents an orthonormal basis including eigenfunctions whose eigenvalues are non-zero and positive. Karhunen Loeve Transform of the sector covariance matrix shows that there is only a single eigenvalue, λ_k, whose value is nonzero and statistic for that sector thus can be achieved with the eigenfunction corresponding to that eigenvalue. Indeed, that eigenfunction gives the conventional sum beamformer as expected.

If D is chosen as 2, the beamspace pattern of the second column of $\mathbf{U}$ will become as in Figure 3.6. Since the first column of the beamspace matrix corresponds

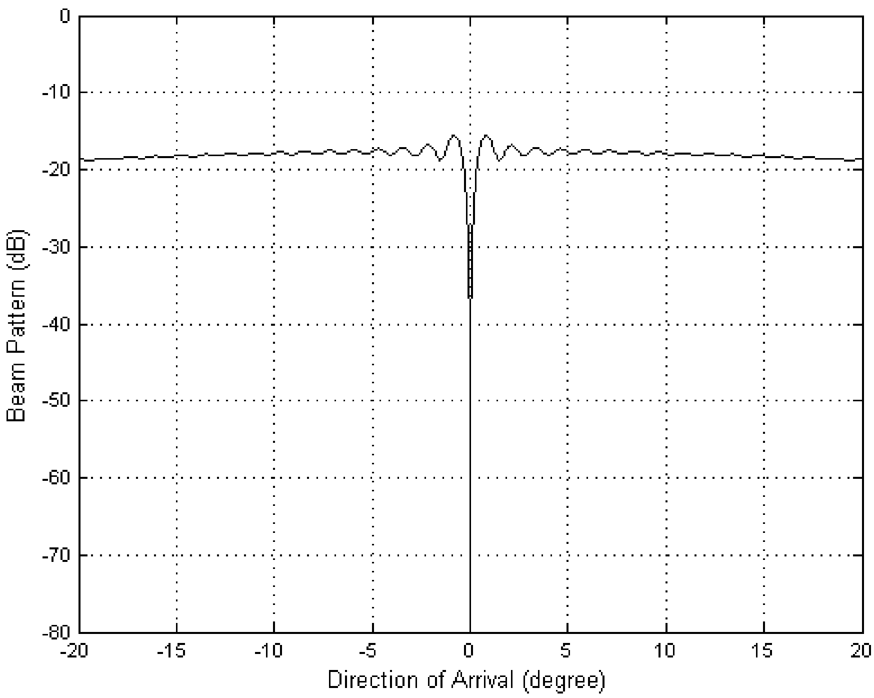

Figure 3.6: Beamspace beam pattern for the 2nd column of beamspace matrix.

to the desired statistics, second and the other columns of the beamspace matrix are orthogonal to the signal of interest and have a null at that point.

In a single point case, it is shown that the optimal statistic can be achieved with the first eigenvector of the sector covariance matrix or with the conventional sum beamformer steering at that point. The relation between the eigenvector and the conventional beamformer is analogous to that of the Discrete Karhunen Loeve Transform and the Discrete Fourier Transform. In [23], it was stated that the eigenfunctions of any circulant matrix, a special type of Toeplitz matrix where each row is a circularly rotated version of the preceding row vector as in (3.28), consist of complex exponentials

$$\mathbf{R} = \begin{bmatrix} \mathrm{r}_0 & \mathrm{r}_{-1} & \mathrm{r}_{-2} & \dots & \mathrm{r}_{1-N} \\ \mathrm{r}_{1-N} & \mathrm{r}_0 & \mathrm{r}_{-1} & \dots & \mathrm{r}_{2-N} \\ \mathrm{r}_{2-N} & \mathrm{r}_{1-N} & \mathrm{r}_0 & \dots & \mathrm{r}_{3-N} \\ \vdots & \vdots & \vdots & \ddots & \vdots \\ \mathrm{r}_{-1} & \mathrm{r}_{-2} & \mathrm{r}_{-3} & \dots & \mathrm{r}_0 \end{bmatrix}. \tag{3.28}$$

In other words, the Fourier basis functions and the eigenfunctions of such matrices turn out to be identical. Consequently, it is inevitable to achieve the exactly same subspace with both beamspace construction methods for a circulant covariance matrix.

The foregoing relation between the DFT and the DKLT was proven in [10] for a covariance matrix comprised of real coefficients: $\mathbf{u}_i$ is the eigenvector consisting of complex exponentials

$$\mathbf{u}_i = \frac{1}{\sqrt{N}} \begin{bmatrix} 1 \\ e^{j\frac{2\pi}{N}i} \\ e^{j\frac{2\pi}{N}2i} \\ \vdots \\ e^{j\frac{2\pi}{N}(N-1)i} \end{bmatrix}, \tag{3.29}$$

where N is the number of array elements. The eigenvalue equation can be written as

$$\mathbf{R}\ \mathbf{u}_i = \mathrm{S[i]}\ \mathbf{u}_i, \tag{3.30}$$

where S[i] refers to the resultant eigenvalue which is also assumed to correspond to the power density at frequency $\frac{2\pi}{N}i$. Conjugating both sides of (3.30) yields

$$\begin{bmatrix} \mathrm{r}_0 & \mathrm{r}_1 & \mathrm{r}_2 & \dots & \mathrm{r}_{N-1} \\ \mathrm{r}_{N-1} & \mathrm{r}_0 & \mathrm{r}_1 & \dots & \mathrm{r}_{N-2} \\ \mathrm{r}_{N-2} & \mathrm{r}_{N-1} & \mathrm{r}_0 & \dots & \mathrm{r}_{N-3} \\ \vdots & \vdots & \vdots & \ddots & \vdots \\ \mathrm{r}_1 & \mathrm{r}_2 & \mathrm{r}_3 & \dots & \mathrm{r}_0 \end{bmatrix} \begin{bmatrix} 1 \\ e^{-j\frac{2\pi}{N}i} \\ e^{-j\frac{2\pi}{N}2i} \\ \vdots \\ e^{-j\frac{2\pi}{N}(N-1)i} \end{bmatrix} = \mathrm{S[i]} \begin{bmatrix} 1 \\ e^{-j\frac{2\pi}{N}i} \\ e^{-j\frac{2\pi}{N}2i} \\ \vdots \\ e^{-j\frac{2\pi}{N}(N-1)i} \end{bmatrix} \tag{3.31}$$

where conjugate symmetric property, $\mathbf{r}[l] = \mathbf{r}^*[-l]$, of the autocorrelation function is utilized. In fact, as its name indicates, power spectral density -PSD-, S[i] takes only the real values due to that property.

The equation (3.31) points out N linear equations and the first equation is given as

$$\mathrm{S[i]} = \sum_{k=0}^{N-1} \mathbf{r}_k\ e^{-j\frac{2\pi}{N}ki}. \tag{3.32}$$

The other equations are the circularly shifted versions of the first equation, (3.32), and thereby multiplied by $e^{j\frac{2\pi}{N}\xi i}$, where ξ represents the integer amount of shifts.

In this way, the equations are satisfied for all values of i and this illustrates that the complex exponentials, $\mathbf{u}_i$, are the eigenvectors of the covariance matrix given in (3.28).

The foregoing discussion points out that if the sector has a circulant covariance matrix, both beamspace construction methods will give the same basis functions. However, such circulant sector covariance matrices is only possible for the periodic processes, i.e. process with line spectra. In [23], it was explained that, the asymptotic properties of the Toeplitz matrices having off diagonal terms approaching to zero are asymptotically equivalent to the circular matrices. In fact, the DKLT and the DFT basis of a covariance matrix having decaying terms with further lags can be considered as similar, [10]. This means that, it is not surprising to observe similar but not exactly the same performance results while evaluating eigenvector and DFT beamformers with increasing dimensions.

3.4 Computational Cost

In this part of the thesis, several algorithms for implementing the eigenvector and the DFT beamformers are discussed. In addition, complexity and efficiency of these implementations are compared. It has to be underlined that there are many ways to measure efficiency and complexity; however, in the scope of this thesis, the number of arithmetic multiplications and additions are used as a measure of computational cost.

Matrix multiplication, which is given in (3.2), can be used to implement the eigenvector and the DFT beamformers. It can be considered as a direct form of constructing the beamspace. For D subspace dimensions, it would cost $4DN$ operations.

Besides the matrix multiplication, the DFT beamformer can also be applied by more efficient algorithms. In fact, there is a set of algorithms to evaluate the

DFT beamformer. Briefly, these algorithms reformulate the Fourier transform in terms of a convolution in order to achieve efficiency [24]. As examples of such methods, Goertzel and chirp-z transform algorithms are studied to evaluate the DFT beamformer.

In [25], the computational cost of Goertzel algorithm, which is used to calculate any desired set of samples of the DTFT of a finite-length sequence, was given by $3ND$. Moreover, the computational cost of chirp-z transform algorithm, which is widely used to compute a limited range of spectral frequencies [26], was also given by $4\left[\alpha N\log_2(N)+N(\alpha+6)\right]$, where N refers to the number of elements in full dimensions. It is worthy of note that these computations were presented for real input data in [25] and the same assumption is also followed in this section. With the analysis in [27], the cost was reduced to $4\alpha N\log_2(D)+\mathrm{N}(4\alpha+25)-D$, where D refers to the number of elements in reduced dimensions. In [25], it was stated that the value for α ranges from 4 to 5, depending on the implementation.

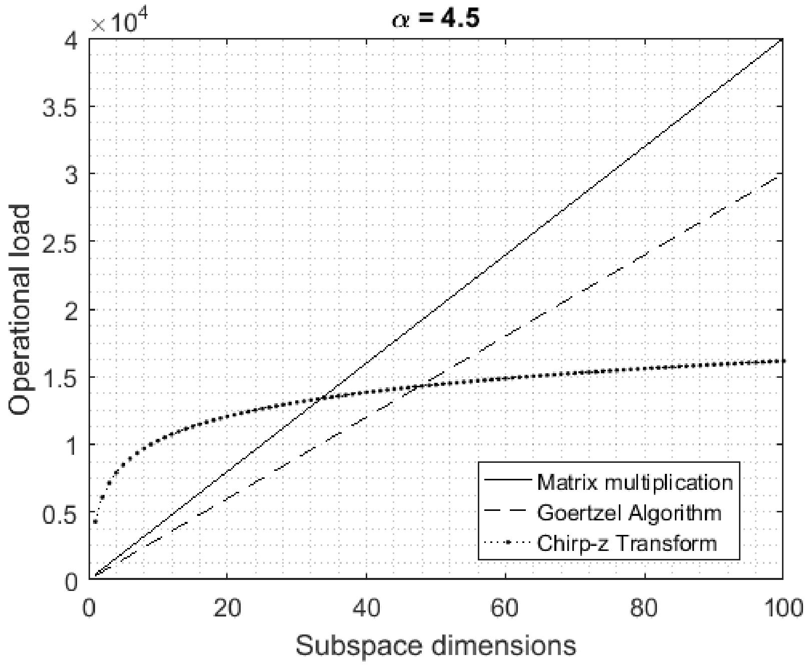

Figure 3.7: Computational complexity for DFT and eigenvector beamformers.

In Figure 3.7, computational costs of the methods are plotted as a function of reduced space dimensions for $N = 100$ and $\alpha = 4.5$.

Figure 3.7 shows that the implementation of DFT beamformer can be efficiently performed by using Goertzel algorithm for $D < 48$. For D > 48, implementation of dimension reduction operation with the chirp-z transform algorithm achieves more efficient results in terms of computational complexity.

As very well appreciated, these methods may not provide orthogonal beams at the output. Considering the criterion given in (3.1), orthogonality can be provided by multiplying the data with a DxD Gram-Schmidt matrix after beamspace processing. Orthogonalization process applied to the subspace data increases the computational cost with the addition of $4D^2$ operations. The revised computational costs are plotted as a function of reduced space dimensions in Figure 3.8.

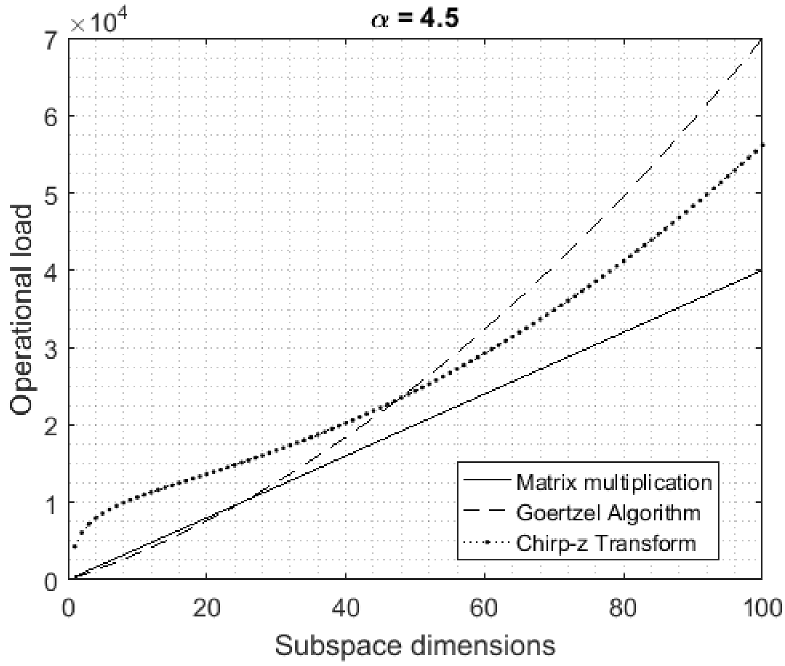

Figure 3.8: Computational complexity for DFT and eigenvector beamformers with orthogonalization process in beamspace.

Figure 3.8 indicates that the addition of the orthogonalization operation increases the computational complexity of the studied methods. For $D < 25$, the Goertzel algorithm gives the best performance concerning operational load. However, the costs are very similar to the ones achieved by straightforward implementation of the beamspace processing. In fact, the lowest results for all other values of D are achieved by the matrix multiplication method as observed in Figure 3.8.

It has to be underlined that a final assessment for computational load depends on the implementation technology and the application. These analyses are performed in order to develop an insight about the computational complexities of the beamspace operations. According to the analysis, it can be inferred that the DFT beamformer implemented with the Goertzel and the chirp-z transform can be advantageous regarding the operational load against eigenvector beamformer when orthogonality is not needed. However, when the orthogonality is required between channels, matrix multiplication method achieves the lowest computational cost for $D > 25$. Moreover, it performs similar to the Goertzel algorithm for $D < 25$.

3.5 On the Choice for the Reduced Space Dimension

In a case where the sector includes only a single point in space, determining the number of subspace dimension is straightforward as shown in Section 3.3; however, this is not the case in general. To establish a relationship between subspace dimension and the sector, eigenvalues belonging to that sector can be used. In fact, the relation between eigenvalues of the sector and the average power loss of the sector is presented and the number of the reduced space dimension is determined in this part of the thesis.

Average power of the sector can be calculated as

$$\begin{aligned} \mathrm{P_{avg}} &= \frac{1}{\phi_{max} - \phi_{min}} \int_{\phi_{min}}^{\phi_{max}} \|\mathbf{a}(\phi)\|^2 \, d\phi. \\ &= \frac{1}{\phi_{max} - \phi_{min}} \int_{\phi_{min}}^{\phi_{max}} \mathbf{a}(\phi)^{\mathbf{H}} \mathbf{a}(\phi) d\phi. \end{aligned} \tag{3.33}$$

Using the well known property, $\mathbf{t}^{\mathbf{H}}\mathbf{t} = \mathrm{tr}\{\mathbf{t}\mathbf{t}^{\mathbf{H}}\}$ where $\mathbf{t}$ is of size $N \times 1$, (3.33) can also be written as

$$\mathrm{P_{avg}} = \mathrm{tr}\left\{ \frac{1}{\phi_{max} - \phi_{min}} \int_{\phi_{min}}^{\phi_{max}} \mathbf{a}(\phi)\mathbf{a}(\phi)^{\mathbf{H}} d\phi \right\}. \tag{3.34}$$

The expression given in the curly brackets in (3.34) is the covariance matrix of the sector found in (3.15). The average power of the sector can be calculated by the trace of the sector covariance matrix

$$\mathrm{P_{avg}} = \mathrm{tr}\big\{\mathbf{R}\big\}. \tag{3.35}$$

Covariance matrix, $\mathbf{R}$, is known to be a Hermitian matrix and any Hermitian matrix can be expanded as

$$\mathbf{R} = \mathbf{V}\ \mathbf{\Lambda}\ \mathbf{V^H}. \tag{3.36}$$

where $\mathbf{V}$ includes the eigenvectors as columns in order and $\mathbf{\Lambda}$ consists of corresponding eigenvalues in its diagonal terms. In facts, (3.36) indicates the eigendecomposion of the matrix $\mathbf{R}$. The columns of $\mathbf{V}$ in (3.36) are orthonormal. The trace of the covariance matrix can be calculated as

$$\begin{aligned} \mathrm{tr}\big\{\mathbf{R}\big\} &= \mathrm{tr}\big\{\mathbf{V}\ \mathbf{\Lambda}\ \mathbf{V^H}\big\}, \\ &= \mathrm{tr}\big\{\mathbf{\Lambda}\ \mathbf{V^H}\ \mathbf{V}\big\}. \end{aligned} \tag{3.37}$$

In the second line of (3.37) cyclic property of the trace is used. Considering the orthonormality property of $\mathbf{V}$ matrix, (3.37) can be simplified as

$$\begin{aligned} \mathrm{tr}\big\{\mathbf{R}\big\} &= \mathrm{tr}\big\{\mathbf{\Lambda}\big\}, \\ &= \sum_{k=1}^{N} \lambda_k, \end{aligned} \tag{3.38}$$

where λ_k is the kth eigenvalue of the covariance matrix. (3.38) represents the average power in the sector when full dimension is used. If the number of channels is reduced by beamspace operation, the average power of the sector can then be calculated as

$$\mathrm{P}_{\mathrm{avg}_D} = \sum_{k=1}^{D} \lambda_k, \tag{3.39}$$

where D is the number of the reduced space dimension. Dividing the average power achieved with the reduced space dimension, (3.39), by the average power in full dimension, (3.38), the normalized average power in the sector is calculated as

$$\mathrm{P}_{\mathrm{avg}_{\mathrm{norm}}} = \frac{\sum_{k=1}^{D} \lambda_k}{\sum_{k=1}^{N} \lambda_k}. \tag{3.40}$$

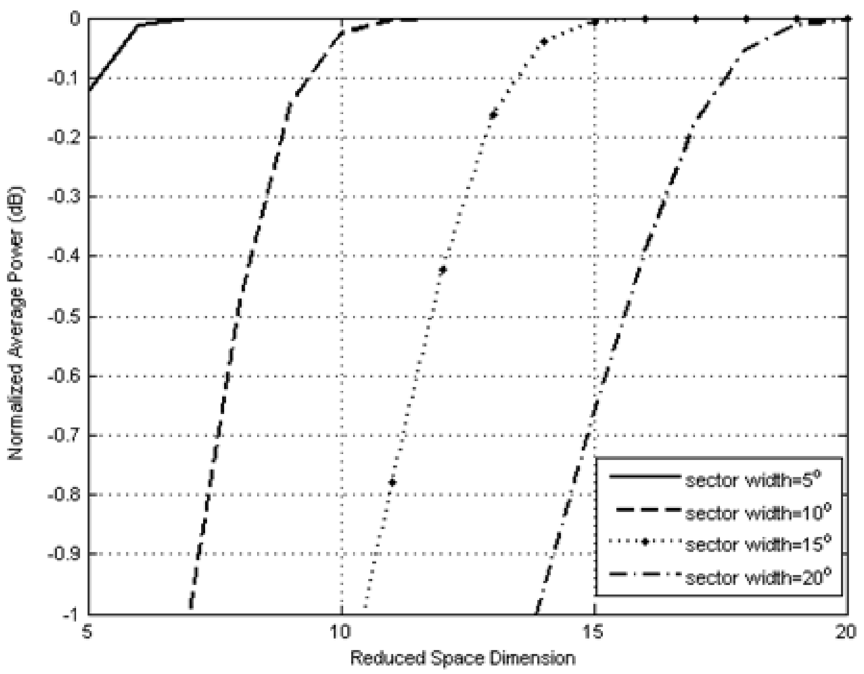

Figure 3.9: Average power for different sector widths and reduced space dimensions.

Using (3.40), the normalized average power in the sector is shown for various sector widths and reduced space dimensions in Figure 3.9.

In Figure 3.9 the sector widths are taken as 5°, 10°, 15°, 20°; and the dimensions of the reduced space are varied from 5 to 20. Average power loss increases with enlarging sector width for any reduced space dimension. It is an expected result to lose energy with increasing sector widths and decreasing the number of dimensions. Furthermore, increasing subspace dimension can retain wider sector's energy.

The main advantage of beamspace processing was stated as the reduction of data. Figure 3.9 indicates that beamspace processing exposes a certain loss with reduced space dimensions. In this part of the thesis, average power loss of the beamspace processing is taken as %1. In other words, reduced space dimension is determined to provide an average power loss of at most %1. In order to calculate the reduced space dimension, a threshold is assigned and sum of the eigenvalues are compared with it.

$$\eta = \frac{\sum_{k=1}^{D} \lambda_k}{\sum_{l=1}^{N} \lambda_l} \tag{3.41}$$

where η is the threshold value, λ_k is the k^{th} eigenvalue of the sector covariance matrix, D is the subspace dimension and N is the number of elements in the array. An average loss of %1 makes threshold, η, in (3.41) be equal to -0.0436 dB.

For the rest of this chapter, the sector is taken as in Table 3.1, which contains angles from $-5°$ to $5°$. Considering the array specifications defined in Chapter 2, and the sector having $10°$ angular width, (3.41) results in 10 reduced space channels. Thus, analyses in the following sections are made for the sector with $10°$ angular width and 10 reduced space dimensions.

Table 3.1: Sector parameters

Value	**Explanation**
100	Number of elements in the array
$10°$	Angular width of the sector
$0°$	Center of the sector
10	Reduced space dimension

3.6 Beamspace Signal to Noise Ratio

Beamspace beamformer processing is illustrated in Figure 3.10.

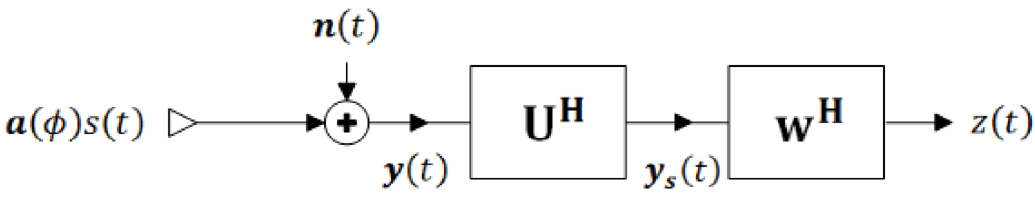

Figure 3.10: Processing chain of the beamspace beamforming.

The vector $\mathbf{w}$ refers to the spatial weights to form the beam in the beamspace. In fact, it enables the generation of the beam anywhere within the sector. The signal model given in (3.2) is revised for beamspace beamformer processing as

$$\begin{aligned}
\mathbf{y}(t) &= \mathbf{a}(\phi)\mathrm{s}(t) \ + \ \mathbf{n}(t), \\
\mathbf{y}_s(t) &= \mathbf{U^H}\ \mathbf{y}(t) \\
&= \mathbf{U^H}\ \mathbf{a}(\phi)\mathrm{s}(t) \ + \ \mathbf{U^H}\ \mathbf{n}(t), \\
\mathrm{z}(t) &= \mathbf{w^H}\ \mathbf{y}_s(t), \\
&= \mathbf{w^H}\ \mathbf{U^H}\ \mathbf{a}(\phi)\mathrm{s}(t) \ + \ \mathbf{w^H}\ \mathbf{U^H}\ \mathbf{n}(t).
\end{aligned} \tag{3.42}$$

The SNR of a point source at the end of the beamspace processing can then be calculated as

$$\begin{aligned}
\mathbf{SNR}(\phi) &= \frac{E\Big\{\mathbf{w^H}\ \mathbf{U^H}\ \mathbf{a}(\phi)\ \mathrm{s}(t)\ \mathrm{s}^{\mathbf{H}}(t)\mathbf{a^H}(\phi)\ \mathbf{U}\ \mathbf{w}\Big\}}{E\Big\{\mathbf{w^H}\ \mathbf{U^H}\ \mathrm{n}(t)\ \mathrm{n}^{\mathbf{H}}(t)\ \mathbf{U}\ \mathbf{w}\Big\}}, \\
&= \frac{\mathbf{w^H}\ \mathbf{U^H}\ \mathbf{a}(\phi)\ E\Big\{\mathrm{s}(t)\ \mathrm{s}^{\mathbf{H}}(t)\Big\}\ \mathbf{a^H}(\phi)\ \mathbf{U}\ \mathbf{w}}{\mathbf{w^H}\ \mathbf{U^H}\ E\Big\{\mathrm{n}(t)\ \mathrm{n}^{\mathbf{H}}(t)\Big\}\ \mathbf{U}\ \mathbf{w}}, \\
&= \frac{\sigma_s^2}{\sigma_n^2}\ \frac{|\mathbf{w^H}\ \mathbf{U^H}\ \mathbf{a}(\phi)|^2}{\left\|\mathbf{w^H}\ \mathbf{U^H}\right\|^2},
\end{aligned} \tag{3.43}$$

where σ_n^2 and σ_s^2 refers to the noise and signal variances, respectively. In addition, the first fractional expression in the last line of (3.43) corresponds to the SNR at each array element. To maximize SNR value at ϕ, $\mathbf{w}$ is taken as

$$\mathbf{w} \ = \ \mathbf{U^H}\ \mathbf{a}(\phi). \tag{3.44}$$

Inserting (3.44) into (3.43), SNR formula under AWGN reduces into

$$\begin{aligned}
\mathbf{SNR}(\phi) &= \frac{\sigma_s^2}{\sigma_n^2}\ \frac{|\mathbf{a^H}(\phi)\ \mathbf{U}\ \mathbf{U^H}\ \mathbf{a}(\phi)|^2}{\left\|\mathbf{a^H}(\phi)\ \mathbf{U}\ \mathbf{U^H}\right\|^2}, \\
&= \frac{\sigma_s^2}{\sigma_n^2}\ \frac{|\mathbf{a^H}(\phi)\ \mathbf{U}\ \mathbf{U^H}\ \mathbf{a}(\phi)|^2}{\|\mathbf{a^H}(\phi)\ \mathbf{U}\ \|^2}, \\
&= \frac{\sigma_s^2}{\sigma_n^2}\ |\mathbf{a^H}(\phi)\ \mathbf{U}\ \mathbf{U^H}\ \mathbf{a}(\phi)|, \\
&= \frac{\sigma_s^2}{\sigma_n^2}\ \left\|\mathbf{a^H}(\phi)\ \mathbf{U}\ \right\|^2.
\end{aligned} \tag{3.45}$$

In the second line of (3.45), the orthonormality of the columns of $\mathbf{U}$ matrix, (3.1), is used.

The equation (3.45) points out that SNR depends on the relation between beamspace matrix and the signal impinging on the array. SNR can be provided in a lossless manner, if the signal succesfully projects on the beamspace. Since the sector contains infinitely many points in space, and the rank of the processor is limited to a finite number, D, it is inevitable to encounter with SNR loss after dimension reduction. However, considering the sector width, a proper selection of beamspace matrix size can keep that loss negligibly small. That was studied in Section 3.3 and threshold, η, given in (3.41), was assigned as -0.0436 dB.

In this part of the thesis, SNR performances of the dimension reduction methods are examined qualitatively. Table 3.1 depicts the sector parameters used to compare SNR performances of the methods.

SNR performances of the beamspace construction methods are given in Figure 3.11. According to Figure 3.11, eigenvector beamformer gives the best performance, considering the minimum average SNR loss in the sector, which can also be related with the minimization of L_1-norm of the point SNR at the output of the beamspace beamformer. However, the performance of the eigenvector beamformer is decreasing at the edges of the sector. In fact, performance degradation is observed at the edges of the sector for all methods. The best performance at the edges of the sector is achieved by the DFT beamformer with $0.95°$ intervals succeeding in minimax criteria which can also be considered as the minimization of L_∞-norm of the point SNR in the sector. The DFT beamformer with $1.05°$ intervals exhibits a visible performance difference compared to the other methods because it enlarges out of the sector by $0.5°$. Therefore, it can be inferred even a small enlargement can cause such visible performance degradation in the sector.

Figure 3.11 also exhibits the performance of the methods in the center of the sector. The closely sampled DFT method having an interval of $0.9°$ achieves the best performance. On the other hand, the worst performance at the edges of the sector also belongs to that DFT method.

In summary, SNR performances of eigenvector and DFT beamformers having

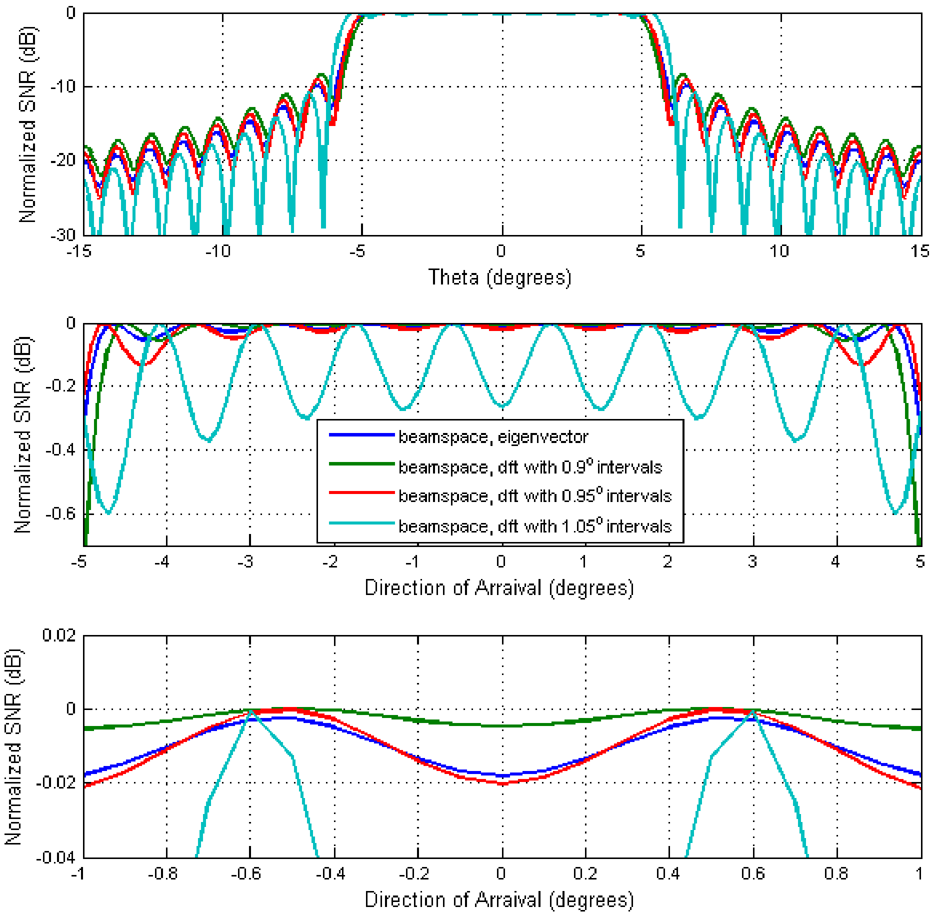

Figure 3.11: SNR performances of beamspace methods versus direction of arrival.

different intervals are investigated. It is qualitatively observed that different methods are able to perform successfully for different design criteria. Due to the close theoretical results, it can be inferred that SNR performance of the eigenvector beamformer and a properly selected DFT beamformer cannot be distinguished from each other in practice.

3.7 Beamspace Cramer Rao Lower Bound

In this part of thesis, the CRB of the beamspace parameter estimation problem is derived and the beamspace CRBs are compared with the element space CRB, which is the CRB for the full size array.

$$\mathbf{CRB} = \frac{\sigma_n^2}{2\ K} \left\{ \mathrm{Re}\Big[(\mathbf{D^H}\ \mathbf{P_a^\perp}\ \mathbf{D})\ \odot\ (\mathbf{R_s}\ \mathbf{A^H}\ \mathbf{R_y^{-1}}\ \mathbf{A}\ \mathbf{R_s})^T \Big] \right\}^{-1}, \tag{3.46}$$

The expression given in (3.46), is obtained from [7], where σ_n^2 is the noise variance, K is the number of snapshot, $\mathbf{R_s}$ is the covariance matrix of the signal coming from the source(s),$\mathbf{R_y}$ is the covariance matrix of the received signal on the array, $\mathbf{A}$ is the transfer matrix consisting of steering vectors and $\mathbf{D}$ is the derivative matrix of steering vectors in $\mathbf{A}$,

$$\begin{aligned} \mathbf{D} &= [\mathbf{d}_1\ \mathbf{d}_2\ \cdots\ \mathbf{d}_L], \\ \mathbf{d}_i &= \frac{\partial \mathbf{a}(\phi_i)}{\partial \phi}. \end{aligned} \tag{3.47}$$

The second term in brackets can be simplified by using the matrix inversion lemma

$$\mathbf{R_y^{-1}} \ = \frac{1}{\sigma_n^2} \Big[\mathbf{I}\ -\ \mathbf{A}\ (\mathbf{A^H}\ \mathbf{A}\ + \sigma_n^2\ \mathbf{R_s}^{-1}) \mathbf{A^H} \Big]. \tag{3.48}$$

Employing the matrix inversion lemma, the CRB expression in (3.46) can be rewritten in a well known form [1]

$$\mathbf{CRB} = \frac{\sigma_n^2}{2\ K} \left\{ \mathrm{Re}\Big\{ \Big[(\mathbf{D^H}\ \mathbf{P_a^\perp}\ \mathbf{D})\ \odot\ \mathbf{R_s}\ \Big[(\mathbf{I}\ + \mathbf{A^H}\ \mathbf{A}\ \frac{\mathbf{R_s}}{\sigma_n^2})^{-1}\ (\mathbf{A^H}\ \mathbf{A}\ \frac{\mathbf{R_s}}{\sigma_n^2}) \Big] \Big] \Big\} \right\}^{-1}. \tag{3.49}$$

The equation (3.46) is first derived in [7] assuming the complex amplitudes to be random. In this thesis, rank-one target assumption is made. Thus, (3.49) turns into

$$\mathbf{CRB} = \frac{\sigma_n^2}{2} \left\{ \mathrm{Re}\Big\{ \mathbf{d^H}\ (1\ -\ \mathbf{a}\ \mathbf{a^H})\ \mathbf{d}\ \sigma_s^2\ \Big[(1 + \mathbf{a^H}\ \mathbf{a}\ \frac{\sigma_s^2}{\sigma_n^2})^{-1}\ \mathbf{a^H}\ \mathbf{a}\ \frac{\sigma_s^2}{\sigma_n^2}\ \Big] \Big\} \right\}^{-1}. \tag{3.50}$$

where σ_s^2 is the variance of the signal. Moreover, only single snapshot is utilized while estimating the direction of arrival; therefore, K can be taken as 1. Considering $\mathbf{a^H a}\ = N$, the expression in (3.50) can be further simplified to

$$\mathbf{CRB} = \frac{1}{2}\ \frac{\sigma_n^2}{\sigma_s^2} \Big(\frac{\sigma_n^2}{N\ \sigma_s^2}\ +\ 1 \Big)\ \frac{1}{\big\| \mathbf{d}^2 \big\|}, \tag{3.51}$$

where N is the number of elements in the array. Equation (3.51) gives the element space CRB formula. In the following part, the beamspace CRB formula is to be derived. Since the beamspace matrix is assumed to have orthonormality property (3.1), the expression can be revised for beamspace processing as

$$\mathbf{CRB} = \frac{\sigma_n^2}{2}\left\{\mathrm{Re}\left\{\ \mathbf{H}\ \sigma_s^2\ \left[(1\ +\ \mathbf{a^H}\ \mathbf{U}\ \mathbf{U^H}\ \mathbf{a}\ \frac{\sigma_s^2}{\sigma_n^2})^{-1}\ \mathbf{a^H}\ \mathbf{U}\ \mathbf{U^H}\ \mathbf{a}\ \frac{\sigma_s^2}{\sigma_n^2}\ \right]\right\}\right\}^{-1},$$
$$\mathbf{H} = \mathbf{d^H}\ \mathbf{U}\ (\mathbf{I}\ -\ \mathbf{U^H}\ \mathbf{a}\ (\mathbf{a^H}\ \mathbf{U}\ \mathbf{U^H}\ \mathbf{a})^{-1}\ \mathbf{a^H}\ \mathbf{U})\ \mathbf{U^H}\ \mathbf{d}. \tag{3.52}$$

If the beamspace matrix is chosen as identity, CRB expression in (3.52) yields the expression in (3.50). Furthermore, if a proper beamspace matrix is used, (3.50) and (3.52) are expected to give approximate results for the parameter estimation problem in the sector. For the rest of this part, two different types of beamspace method and the element space methods are compared qualitatively. The same scenario as in the SNR analysis, which is given in Table 3.1, is studied for parameter estimation problem.

The CRBs of the dimension reduction methods are compared with the CRB of the full size array, i.e. the element space, in Figure 3.12. They exhibit similar characteristics with the SNR performances shown in Figure 3.11. The DFT beamformer with 1.05° intervals experiences oscillations due to the expansion of the sector by 0.5°. At the edges of the sector, the direction estimation performance of all methods decreases as observed in the SNR performances. Contrary to the SNR case, the best performance at the edges of the sector is achieved by DFT beamformer with 1.05° intervals. Other methods present similar performances to each other. Figure 3.12 also indicates the CRB results of the methods around the center of the sector. In that scenario, closely sampled DFT method having interval of 0.9° shows the best performance as in the SNR case.

To sum up, derivations of the CRB for the dimension reduction methods are studied in this part of the thesis and results are qualitatively compared with the CRB of the full size array. It is inferred that the eigenvector beamformer and a properly selected DFT beamformer show similar theoretical results and thereby may not be easily distinguished from each other in practice.

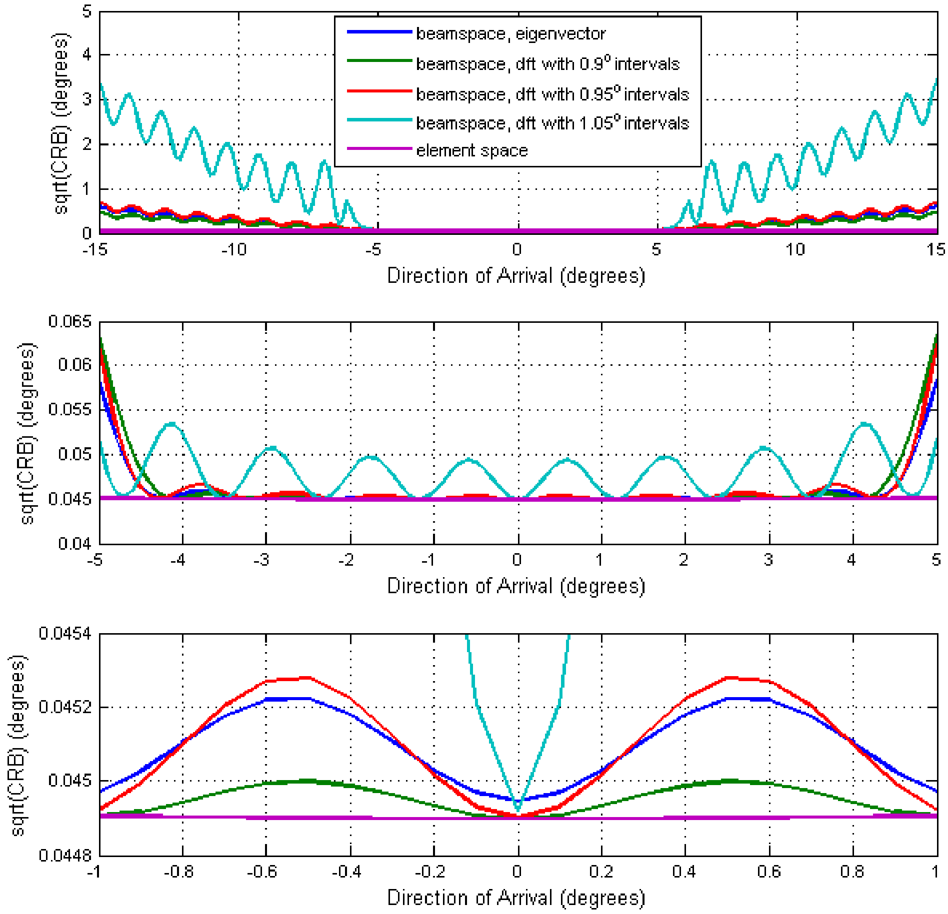

Figure 3.12: CRB analyses of the beamspace methods versus direction of arrival for SNR = 20 dB.

CHAPTER 4

ARRAY TAPERING

It is important for radar systems to be equipped with the low sidelobe antenna pattern to deal with the high clutter and jammer scenarios [28]. In [12], it was stated radars having low sidelobe receiver patterns are exposed to less clutter, chaff, and jamming power. Since adjusting the spatial distribution of the electric field across the antenna provides the control over the sidelobe structure of an antenna's radiation pattern [13], radiation patterns with low sidelobe levels can be achieved by an additional amplitude taper to array elements.

This phenomenon, tapering, has been studied in detail in the literature by a number of authors [11], [1], [12], [13], and [14]. Therefore, the aim of this chapter is not to compare different tapering classes or to discuss the advantages of tapering, but to describe the concept of tapering in subspace and to present the implementation methods of this phenomenon in reduced dimensions.

The organization of this chapter is as follows: First, the conventional tapering method is introduced. Then, a novel method, tapering after dimension reduction, is presented. Finally, the performances of both implementation methods are compared in various scenarios.

4.1 Conventional Tapering: Tapering Before Dimension Reduction

In this method, tapering is applied to the antenna elements in a conventional manner. To clarify, any antenna element is included an additional amplitude taper in the element space. Tapering before dimension reduction is applied in

[1] to reduce the sidelobe levels of radiation pattern. In Figure 4.1, the block diagram of this method is illustrated where $\mathbf{T}$ is a diagonal matrix consisting of the tapering coefficients in its diagonal terms, $\mathbf{U}$ is the beamspace matrix and $\mathbf{w}(\phi_s)$ is the beamspace beamformer looking towards ϕ_s direction.

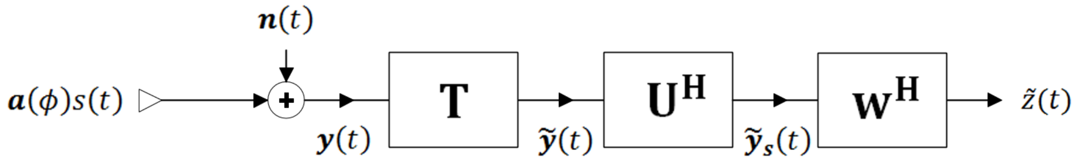

Figure 4.1: Processing chain for tapering before dimension reduction

Beamspace beamformer weights, $\mathbf{w}(\phi_s)$, are chosen to maximize SNR at ϕ_s under AWGN

$$\mathbf{w}(\phi_s) \;=\; \mathbf{U^H}\;\mathbf{a}(\phi_s). \tag{4.1}$$

Beamspace signal model given in (3.2) is revised as

$$\begin{aligned} \tilde{\mathbf{y}}(t) &= \mathbf{T}\;\mathbf{y}(t), \\ \tilde{\mathbf{y}}_s(t) &= \mathbf{U^H}\;\tilde{\mathbf{y}}(t), \\ \tilde{\mathrm{z}}(t) &= \mathbf{w^H}(\phi_s)\;\tilde{\mathbf{y}}_s(t), \end{aligned} \tag{4.2}$$

where $\tilde{\mathbf{y}}(\mathrm{t})$ is the tapered received signal at the antenna elements, $\tilde{\mathbf{y}}_s(\mathrm{t})$ is the tapered reduced dimensional signal vector, and $\tilde{\mathrm{z}}(\mathrm{t})$ is the beamspace beamformer output. SNR of a rank-one target at the output of the beamspace beamformer under AWGN is given as

$$\begin{aligned} \mathbf{SNR}_{\phi_s}(\phi) &= \frac{\mathbf{w^H}(\phi_s)\;\mathbf{U^H}\;\mathbf{T}\;\mathbf{a}(\phi)\;\sigma_s^2\;\mathbf{a^H}(\phi)\;\mathbf{T}\;\mathbf{U}\;\mathbf{w}(\phi_s)}{\mathbf{w^H}(\phi_s)\;\mathbf{U^H}\;\mathbf{T}\;\mathbf{R}_n\;\mathbf{T}\;\mathbf{U}\;\mathbf{w}(\phi_s)}, \\ &= \frac{|\;\mathbf{a^H}(\phi_s)\;\mathbf{U}\;\mathbf{U^H}\;\mathbf{T}\;\mathbf{a}(\phi)\;|^2\;\sigma_s^2}{\left\|\;\mathbf{a^H}(\phi_s)\;\mathbf{U}\mathbf{U^H}\;\mathbf{T}\;\right\|^2\;\sigma_n^2}, \end{aligned} \tag{4.3}$$

where $\mathbf{R}_n$ is the noise covariance matrix, and ϕ is the direction of the point target. In the second line of (4.3), SNR formula is shortened in a more compact form considering the AWGN. By simply extracting the σ_s^2 and σ_n^2 terms from (4.3), the normalized pattern of the beamspace beamformer steered towards ϕ_s

can be calculated as

$$\mathbf{P}_{\phi_s}(\phi) \;=\; \frac{\mid \mathbf{a^H}(\phi_s)\ \mathbf{U}\ \mathbf{U^H}\ \mathbf{T}\ \mathbf{a}(\phi) \mid^2}{\left\| \mathbf{a^H}(\phi_s)\ \mathbf{U}\mathbf{U^H}\ \mathbf{T} \right\|^2}. \tag{4.4}$$

4.2 Tapering After Dimension Reduction

Employing tapering in the element space, that is before dimension reduction, results in a tapered beamspace as expected. However, the dimension reduction is not a reversible operation; and therefore, any spatial filter applied in a tapered beamspace will not be able to reflect the characteristics of the non-tapered beams. That may lead to a deficiency and may not be desired in some applications. To overcome this drawback of the conventional method, a novel method of tapering after beamspace construction is studied in this chapter.

In this method, beamspace is constructed as in Chapter 3 without any tapering information. Then, in the reduced space, tapered beamspace weights are used to obtain the desired receiver pattern. Figure 4.2 shows the block diagram of tapering after dimension reduction method.

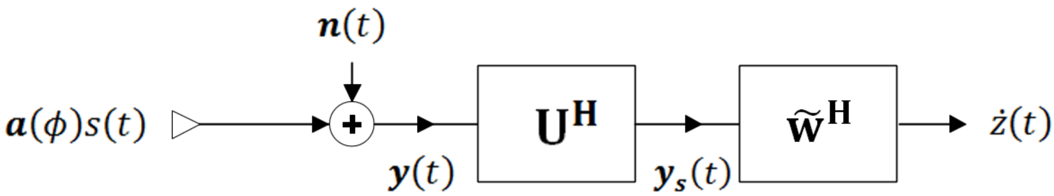

Figure 4.2: Processing chain of the tapering after dimension reduction method

$\tilde{\mathbf{w}}$ refers to the beamspace beamformer including taper characteristics

$$\tilde{\mathbf{w}}(\phi_s) \;=\; \mathbf{U^H}\ \mathbf{T}\ \mathbf{a}(\phi_s), \tag{4.5}$$

where ϕ_s is the direction that the beamformer is steered towards. In this section, beamspace signal is remodelled as follows:

$$\begin{aligned} \mathbf{y}_s(t) \;&=\; \mathbf{U^H}\ \mathbf{y}(t), \\ \dot{z}(t) &= \tilde{\mathbf{w}}^{\mathbf{H}}(\phi_s)\ \mathbf{y}_s(t), \end{aligned} \tag{4.6}$$

where $\dot{z}(t)$ is the tapered beamspace beamformer output. The SNR expression for a rank-one target coming from the ϕ direction under AWGN is calculated as

$$\begin{aligned} \mathbf{SNR}_{\phi_s}(\phi) &= \frac{\tilde{\mathbf{w}}^{\mathbf{H}}(\phi_s)\ \mathbf{U}^{\mathbf{H}}\ \mathbf{a}(\phi)\ \sigma_s^2\ \mathbf{a}^{\mathbf{H}}(\phi)\ \mathbf{U}\ \tilde{\mathbf{w}}(\phi_s)}{\tilde{\mathbf{w}}^{\mathbf{H}}(\phi_s)\ \mathbf{U}^{\mathbf{H}}\ \mathbf{R}_n^2\ \mathbf{U}\ \tilde{\mathbf{w}}(\phi_s)}, \\ &= \frac{|\ \mathbf{a}^{\mathbf{H}}(\phi_s)\ \mathbf{T}\ \mathbf{U}\ \mathbf{U}^{\mathbf{H}}\ \mathbf{a}(\phi)\ |^2\ \sigma_s^2}{\left\|\ \mathbf{a}^{\mathbf{H}}(\phi_s)\ \mathbf{T}\ \mathbf{U}\ \mathbf{U}^{\mathbf{H}}\ \right\|^2\ \sigma_n^2}, \end{aligned} \tag{4.7}$$

where ϕ_s refers to the steering direction of the beamspace beamformer and $\mathbf{R}_n$ corresponds to the noise covariance matrix. Then, the pattern of the beamspace beamformer can be written as

$$\mathbf{P}_{\phi_s}(\phi) = \frac{|\ \mathbf{a}^{\mathbf{H}}(\phi_s)\ \mathbf{T}\ \mathbf{U}\ \mathbf{U}^{\mathbf{H}}\ \mathbf{a}(\phi)\ |^2}{\left\|\ \mathbf{a}^{\mathbf{H}}(\phi_s)\ \mathbf{T}\ \mathbf{U}\ \mathbf{U}^{\mathbf{H}}\ \right\|^2}. \tag{4.8}$$

4.3 Performance Comparison of Tapering Methods

In this section of the thesis, performance comparisons of tapering before dimension reduction and tapering after dimension reduction methıds are made for different reduced space dimensions. Note that the eigenvector beamformer is employed to form the beamspace throughout the study. Taylor weights are used to achieve patterns having low sidelobes. Table 4.1 describes the first case to be studied:

Table 4.1: Scenario for comparing the performances of the beamspace tapering methods

Value	**Explanation**
10	Reduced space dimension
0°	ϕ_s, steering direction
30	Sidelobe suppression level (dB)

In Figure 4.3, it is shown that the receiver patterns of tapering before and after dimension reduction methods which are drawn by employing (4.4) and (4.8), respectively. Additionally, element space - full dimension- tapering pattern is presented in Figure 4.3 and calculated using (4.4), where beamspace matrix -**U**- is taken as the identity matrix of size $N \times N$.

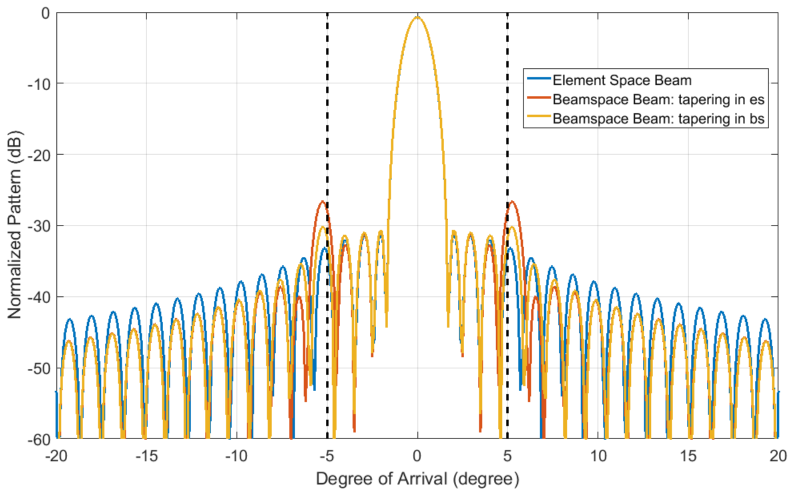

Figure 4.3: Receiver patterns of the tapering methods, ϕ_s is taken as $0°$.

Figure 4.3 points out that both beamspace tapering methods steered towards $0°$, $\phi_s = 0$, generate almost the same pattern with the element space one within the sector. In contrast, at the edges of the sector, a spiky behaviour is observed for the beamspace methods.

In Chapter 3, it was observed that Eigenvector beamformer has better performance around the center of the sector in the SNR sense. Thus, in the following case, ϕ_s is chosen as $-5°$ to observe the pattern performance of the beamspace methods at the edge of the sector.

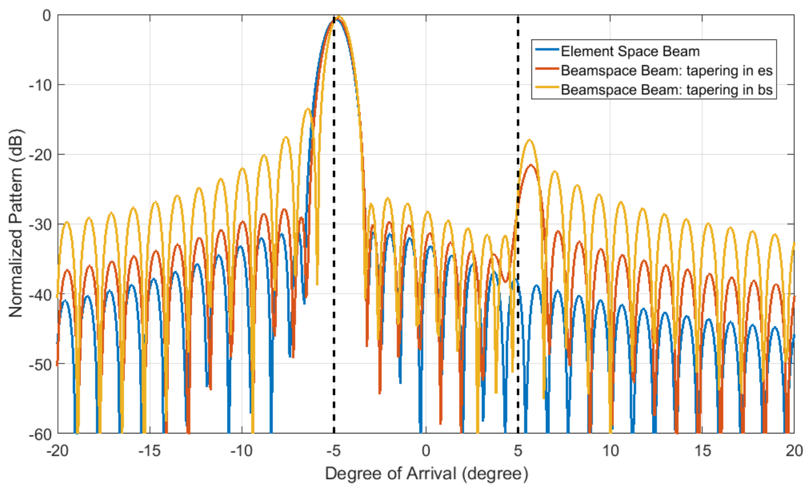

Figure 4.4: Receiver patterns of tapering methods, ϕ_s is taken as $-5°$.

In Figure 4.4, the decrease in the performance is observed not only outside the sector but also within the sector. This means that the beamspace dimension chosen considering the criteria in Section 3.5 is insufficient for tapering operation. In other words, tapering with beamspace processing needs additional reduced space dimensions.

Thus far, %99 threshold criterion has been suitable for non-tapered beams; however, Figure 4.3 and 4.4 clarify that if an additional process is applied to the beamspace beams, then the numerical value of the reduced dimensional space is required to be increased. Considering this requirement, both beamspace tapering methods are investigated with increased dimensions. Patterns of the tapering before dimension reduction method for various dimensions are plotted in Figure 4.5. Since the performance of the beamspace methods degrade at the edges of the sector, ϕ_s is chosen as $-5°$.

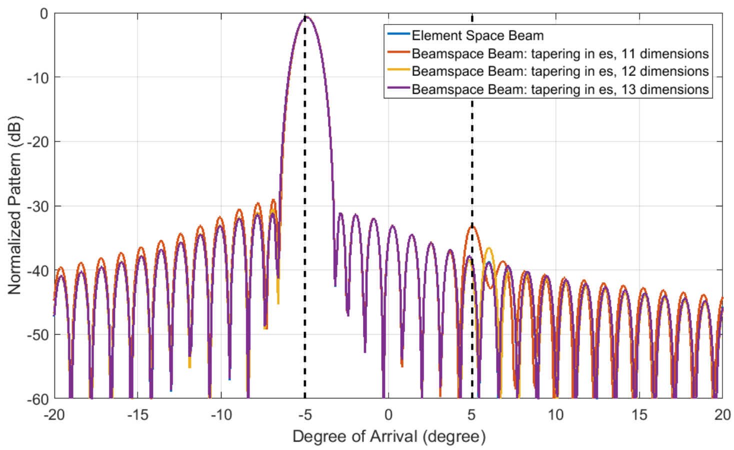

Figure 4.5: Receiver patterns of the tapering before dimension reduction method, ϕ_s is taken as $-5°$.

According to Figure 4.5, the main lobe pattern almost match the element space pattern with only one additional dimension; however, sidelobe pattern is still higher than the desired element space pattern. When an additional reduce space dimension is also utilized, both mainlobe and sidelobe patterns almost match but a spiky behaviour is observed around the other edge of the sector. Finally, beamspace with 3 additional dimensions, which makes the number of the total reduced space dimension 13, achieves the generation of the desired tapered beamspace pattern.

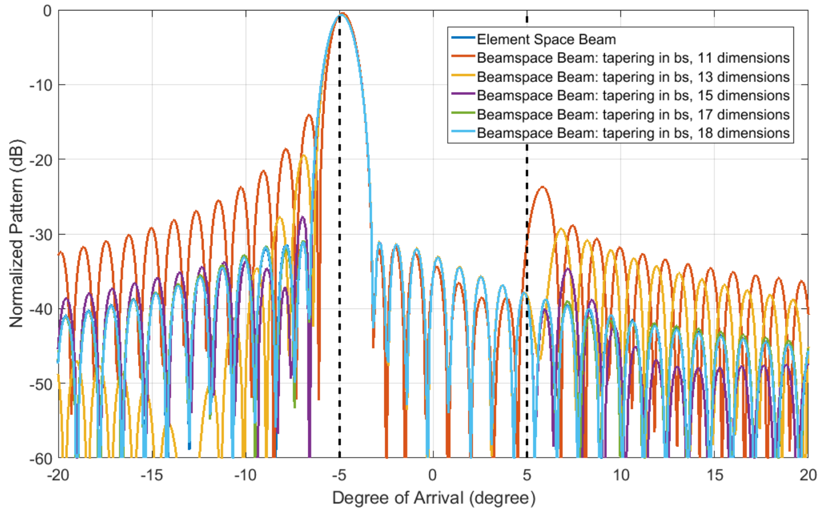

Figure 4.6: Receiver pattern of the tapering after dimension reduction method, ϕ_s is taken as $-5°$.

In Figure 4.6, patterns of the tapering after dimension reduction method are plotted for various beamspace dimensions. Since tapering in beamspace method uses reduced dimensions for tapering, it requires more dimensions than the tapering in element space. This fact can also be seen from the Figure 4.6. Mainlobe of the beamspace pattern is almost identical to the element space one after 5 additional dimensions; on the other hand, the sidelobe pattern of the beamspace method still does not match the desired one and the spiky behaviour is observed outside the sector. Beamspace with 17 dimensions produces a similar pattern to the desired one. In contrast, small differences can be spotted outside the sector when compared to the actual -full dimension- pattern. Beamspace with 8 additional dimensions finally succeeds in generation of the desired pattern.

Until now, the beamspace tapering methods are evaluated qualitatively by indicating their pattern construction performance. In order to develop a feeling for the importance of a proper tapering, SNR analysis is performed considering the case in Table 4.2.

Signal to interference ratios (SINR) in Figure 4.7 are plotted employing equations (4.3) and (4.7). When $\mathbf{R}_n$ is taken as the summation of both interference covariance and the noise covariance as in (4.9), the first lines in (4.3) and (4.7)

Table 4.2: Scenario for comparing the performances of the beamspace tapering methods.

Value	Explanation
15 dB	SNR
$-7°$	ϕ_{j_1}, Angular placement of the first interference source
30 dB	JNR of the first interference source
$2°$	ϕ_{j_2}, Angular placement of the second interference source
30 dB	JNR of the second interference source

define the SINR formula.

$$\begin{aligned} \mathbf{R}_n &= \mathbf{R}_j + \sigma_n^2 \mathbf{I}, \\ \mathbf{R}_j &= \sigma_{j_1}^2 \mathbf{a}(\phi_{j_1}) \mathbf{a}(\phi_{j_1})^{\mathbf{H}} + \sigma_{j_2}^2 \mathbf{a}(\phi_{j_2}) \mathbf{a}(\phi_{j_2})^{\mathbf{H}}, \end{aligned} \tag{4.9}$$

where, σ_j^2 refers to the interference power, ϕ_{j1} and ϕ_{j2} corresponds to the angular placements of the interference sources, respectively.

Figure 4.7 identifies that even if the additional dimensions are not used, tapered beamspace processing performs better than the non-tapered one. When the reduced space dimension is increased, SINR performance of both tapered beamspace methods improves. 3 additional dimensions seem sufficient for tapering before dimension reduction method to achieve the performance of the element space tapering method; however, the tapering after dimension reduction method experiences performance deficiency at the edges. The tapering after beamspace processing reaches to the desired performance with an addition of 7 dimensions. Increasing the dimension further does not make any change in the performance of the methods for that case.

Thus far, array signal model is accepted as flawless; but, it is inevitable to confront with imperfections in practice. The reason of these imperfections can be listed as follows [12]:

1. Phase and amplitude errors due to the feed network and the phase shifters;
2. Deflections in the element placement;
3. Mutual coupling effects and failed elements.

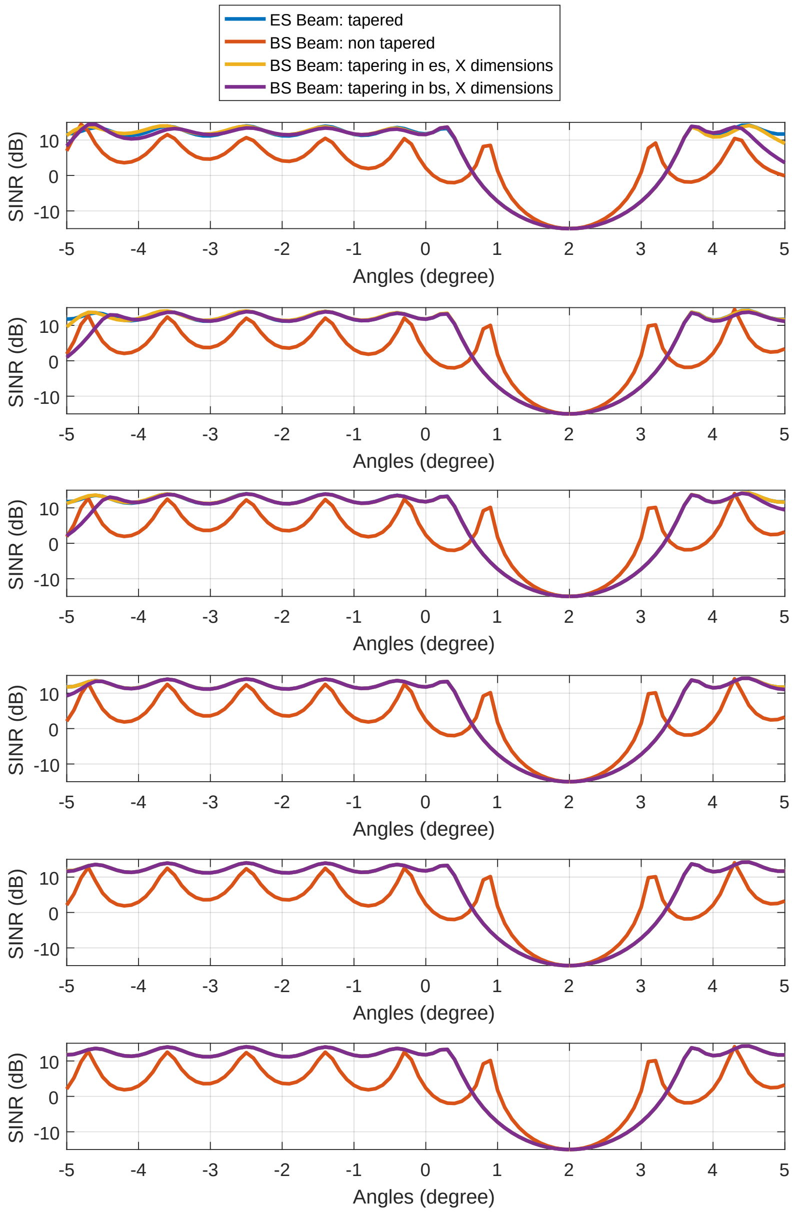

Figure 4.7: SINR performances of the tapering methods within the sector. X is taken as 10, 11, 13, 15, 17 and 18 respectively.

In [29], it was stated that these random errors restrict the sidelobe level and hence average sidelobe performance of the antenna. In order to develop an insight about the robustness of the referred beamspace methods, both pattern and the SINR analysis are repeated considering the array imperfections. Random phase errors are evaluated for the array imperfections in the scope of this thesis.

In the analysis, true steering vectors are used to design spatial filters, including the beamspace matrix and the beamspace beamformer. Imperfections are added to the received echo signal at the receiver and thereby to the steering vectors of the signal and interferences. Uniformly drawn phases from the interval [-5°,5°] are used to make random phase errors.

The pattern performances of the tapering before and after dimension reduction methods with the increasing number of reduced space dimensions are shown in Figures 4.8 and 4.9, respectively.

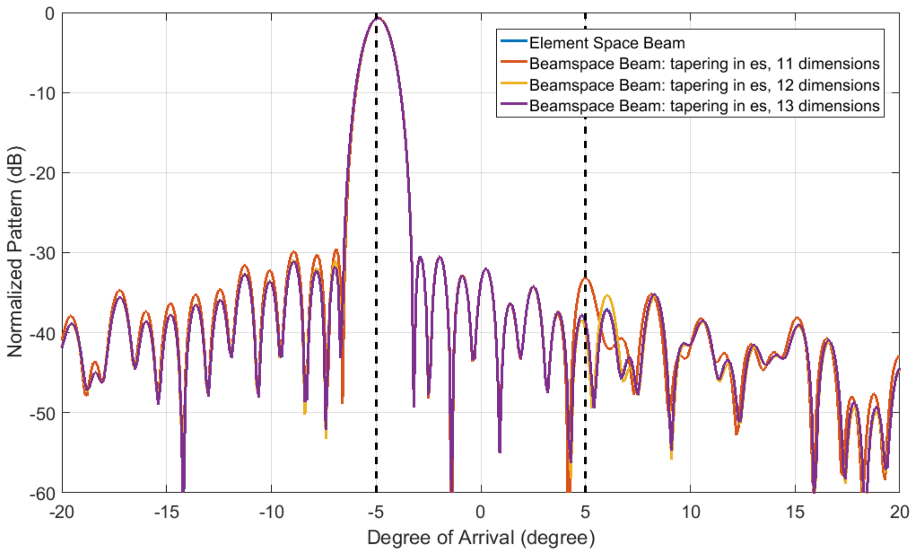

Figure 4.8: Receiver pattern of the tapering before dimension reduction method with random phase errors, ϕ_s is taken as $-5°$.

Considering the challenges occurred in previous cases, ϕ_s is selected from the edge of the sector again. The pattern performances of the beamspace methods with the phase mismatches reduce by the same amount with the performance of the corresponding beamformer in element space. This means that the mismatches do not necessitate an additional dimension in beamspace.

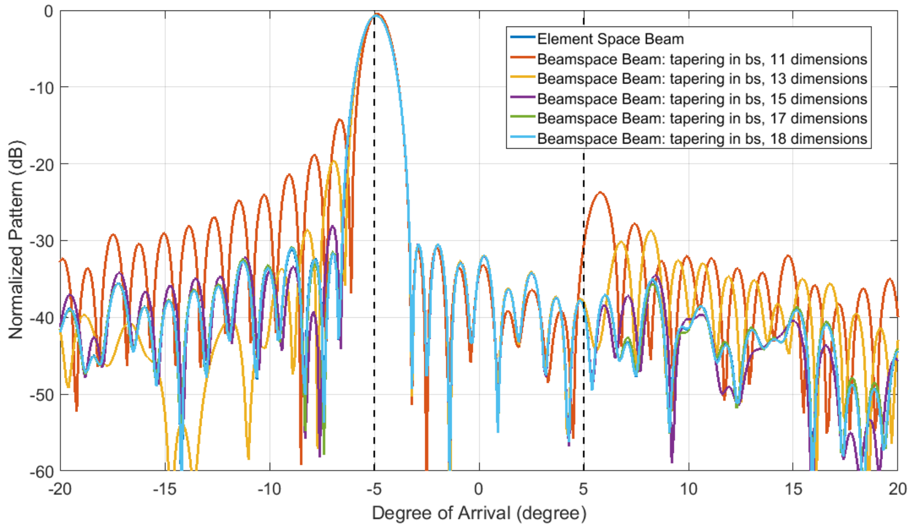

Figure 4.9: Receiver pattern of the tapering after dimension reduction method with random phase errors, ϕ_s is taken as $-5°$.

This can also be inferred from the SINR analysis in Figure 4.10. The SINR performances of the beamspace methods follow the same characteristics with increasing dimensions as in 4.7.

In summary, the tapering phenomenon has been examined in this chapter with the beamspace concept. The performances of tapering before and after beamspace processing have been evaluated. It was seen that tapering requires additional dimensions for the beamspace domain operations. Indeed, the dimension demand depends on the processing chain of tapering in beamspace. For clarity, tapering in element space combined with the beamspace processing gives the same performance compared to the tapering after beamspace processing by using less number of reduced space dimensions. Contrary to the dimension disadvantage, the advantage of the tapering after dimension reduction is to apply tapering coefficients in the beamspace. By doing so, beamspace can be constructed with non-tapered beams and tapering can only be used to form a detection channel after beamspace processing.

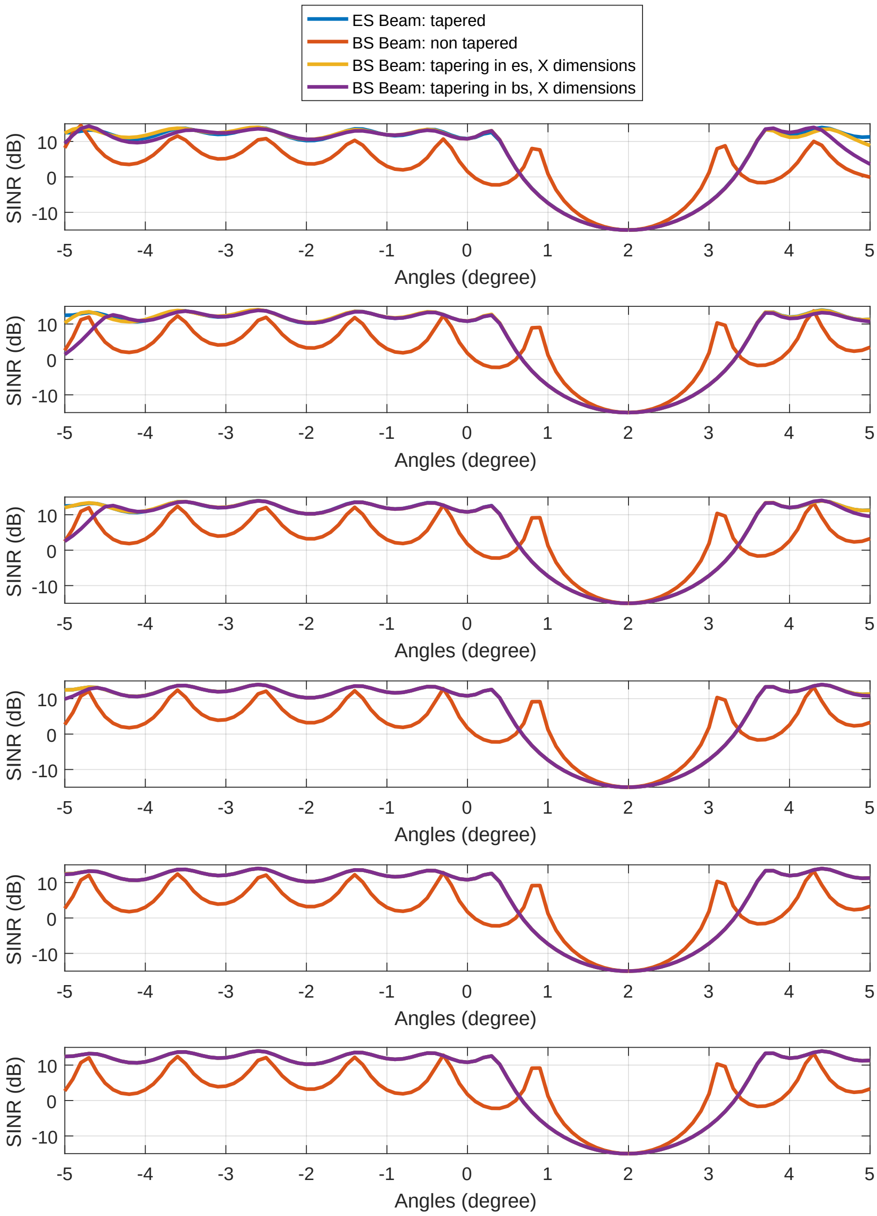

Figure 4.10: SINR performances of the tapering methods within the sector considering random phase errors. X is taken as 10, 11, 13, 15, 17 and 18 respectively.

CHAPTER 5

SIDELOBE BLANKER

In radar receivers, detected signals are assumed to belong to a target in the main beam of the antenna. However, a strong echo might enter from the sidelobe region of the antenna pattern and it might also be perceived as a target located in the main beam. This phenomenon causes major direction finding errors [12]. One way to deal with this problem is to have low sidelobe antenna patterns; but, this may be an insufficient solution against stronger echos. In [16], it was stated that sidelobe blanking (SLB) systems can prevent detections captured by sidelobes. In order to realize that a two-channel receiver system was proposed [16]: main channel and auxiliary channel in which the pattern of the auxiliary channel is larger than the sidelobes of the main channel as in Figure 5.1.

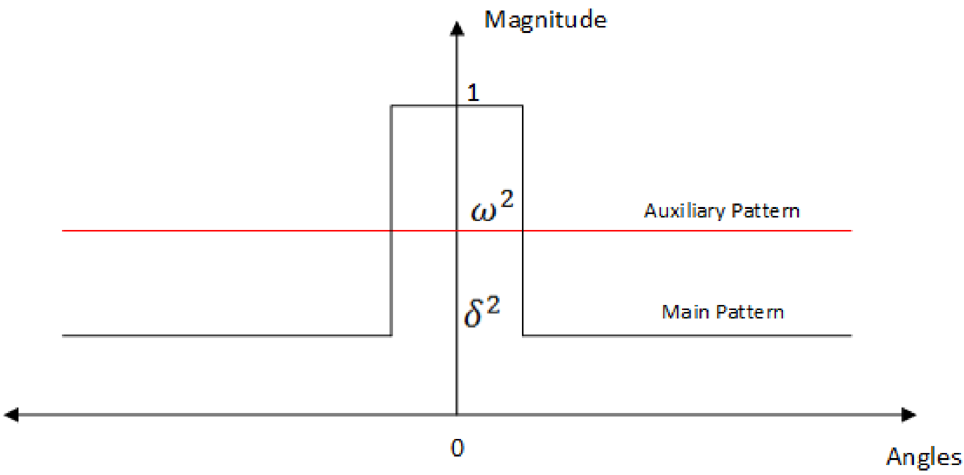

Figure 5.1: Ideal main and auxiliary pattern proposed by Maisel.

The working principle of the proposed system depends on the relation between samples of the main and auxiliary channels downstream from the detector block as in Figure 5.2 [16]. If the magnitude square of the sample under test in the auxiliary channel is larger than that in the main channel, it will be gated. On the other hand, if the magnitude square of the sample in the main channel is larger than that in the auxiliary channel, the sample will be processed with detection algorithms.

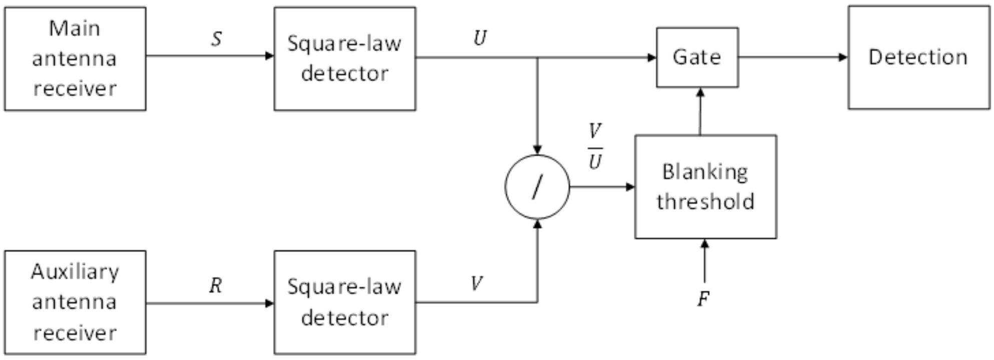

Figure 5.2: Basic sidelobe blanking system.

This system seems extremely simple for the noise free case. However, when it is realized in noisy channels, the probability of detection and thereby the system performance might be reduced. To clarify, even if a target appears in the main beam, the magnitude square of the sample in the auxiliary channel can be larger than that in the main channel due to the system noise. This undesired effect of SLB system is called as target blanking. In order to decrease the probability of target blanking, a threshold, F, is assigned while comparing the main and auxiliary channels.

It is worthy of note that some authors prefer to use the phrase 'jammer' as the signal entering from sidelobe of the antenna. This is also acceptable, because some electronic countermeasure (ECM) systems can delay and transmit the signal coming from the radar. This type of interference is known as coherent repeated interference (CRI) [30]. SLB systems can be employed as a precaution to this type of ECM techniques. However, it should be noted that SLB systems cannot handle with the noise-like interferences (NLI) where all the received samples are affected [31]. To deal with these type of interferences, sidelobe canceller (SLC) systems have been suggested in the literature. The 'jammer' phrase used here only refers to the CRI type jammers. To clarify, SLB systems cope with the targets and CRI type jammers interfering from the sidelobe. In order not to cause any confusion, sidelobe targets and jammers are referred as interferers in the following parts of this chapter.

The main aim of the SLB structure is to increase the probability of blanking, P_B, and to decrease the probability of target blanking, P_{TB}. Considering the main and auxiliary channel patterns in Figure 5.1 and assuming a fixed main channel pattern, improvement on P_B can be achieved by increasing the auxiliary antenna pattern level; on the other hand, reducing P_{TB} can be handled with decreasing auxiliary antenna pattern level. Coupling between P_B and P_{TB} makes the SLB structure complicated. In other words, the trade-off between P_B and P_{TB} may degrade the system performance. In the next section of this chapter, it is aimed to present a way to decouple P_B and P_{TB}. Besides, implementation of the SLB systems in subspace will be examined in this chapter.

5.1 Proposed Auxiliary Antenna Pattern for Sidelobe Blanking

In order to decouple P_B and P_{TB}, a new auxiliary pattern is proposed as shown in Figure 5.3.

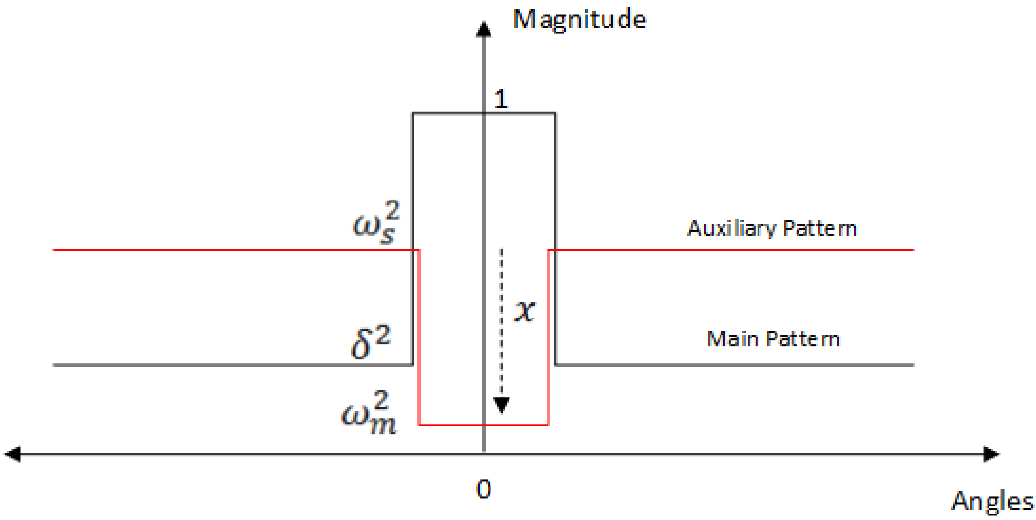

Figure 5.3: Proposed auxiliary channel pattern and main channel pattern.

In Figure 5.3, auxiliary pattern is divided into two parts, namely the main and sidelobe part. Contrary to the classical patterns, proposed auxiliary pattern has nulls, ω_m, in its main part and peaks, ω_s, in its sidelobe part which is analogous to a bandstop filter in space. Note that the aim of the auxiliary antenna is to provide information for sidelobe targets or jammers. In addition, the desired response of the auxiliary channel against main lobe targets is to give small values compared to the main channel. In fact, if an ideal mechanism is to be designed, auxiliary pattern should include zeros in its main part and the maximum gain in its sidelobe part. To realize that, the sidelobe part of the auxiliary pattern is kept higher while keeping the pattern of the main part lower.

When the SLB structure was first proposed in [16] in 1968, the design of the suggested pattern was probably too challenging. However, such an auxiliary antenna pattern can be designed, relatively easily, with today's modern phased array radar systems having hundreds of elements.

5.2 Calculation of Performance Criteria

The performance of the SLB system can be evaluated by means of the probability of blanking an interference, P_B, and blanking a mainlobe target, P_{TB}. Probability calculation for SLB systems was examined in detail in [12] and [19]. In this part of the thesis, evaluation of SLB systems is revised for proposed auxiliary pattern design. The performance is analyzed for Swerling 1 target model which assumes the amplitude is Rayleigh distributed and phase is uniformly distributed over $(0, 2\pi)$ [32]. Probability of blanking, P_B, and probability of target blanking, P_{TB}, are derived following [19].

The performance of the system is evaluated by testing three hypotheses:

- H_0: Null hypothesis corresponding to the noise in the channels.
- H_1: Target in the main lobe and no interference, i.e. no target or jammer in sidelobe.
- H_2: Interference in the sidelobe and no target in the main lobe.

In Figure 5.2, complex valued samples of the main and auxiliary channel signals upstream from the square-law detector are denoted by S and R. Considering the three hypothesis, S and R can be written as

$$
\begin{aligned}
\mathrm{H}_0 &: \begin{cases} S = W_s \\ R = W_r \end{cases} \\
\mathrm{H}_1 &: \begin{cases} S = Ae^{j\phi_A} + W_s \\ R = \omega_m A e^{j\phi_A} + W_r \end{cases} \\
\mathrm{H}_2 &: \begin{cases} S = Ce^{j\phi_C} + W_s \\ R = \frac{\omega_s}{\delta} C e^{j\phi_C} + W_r \end{cases}
\end{aligned}
\tag{5.1}
$$

where W_s and W_r refer to the circular complex white Gaussian distributed noise samples with zero mean and σ_s^2 and σ_r^2 variance, respectively. ϕ_A and ϕ_C are the phases of the target in the mainlobe and target or jammer in the sidelobe. Both ϕ_A and ϕ_C are uniformly distributed over $(0, 2\pi)$. A and C are the magnitude of the target in the mainlobe and interference in the sidelobe, respectively. Both A and C are Rayleigh distributed,

$$
\begin{aligned}
p_C(c) &= \frac{c}{\sigma_C^2} \exp\left(\frac{-c^2}{2\sigma_C^2}\right), \quad c > 0, \\
p_A(a) &= \frac{a}{\sigma_A^2} \exp\left(\frac{-a^2}{2\sigma_A^2}\right), \quad a > 0,
\end{aligned}
\tag{5.2}
$$

where σ_A^2 and σ_C^2 are the average power of the target in the main lobe and interference in the sidelobe, respectively. U and V denote the samples downstream from the square-law detector of the main and auxiliary channels, respectively. The distributions of U and V can be given as

$$
\begin{aligned}
p_U(u|H_0) &= \frac{1}{2\sigma^2} \exp\left(\frac{-u}{2\sigma^2}\right), \\
p_U(u|H_1, A) &= \frac{1}{2\sigma^2} \exp\left(-\frac{u + a^2}{2\sigma^2}\right) I_0\left(\frac{a\sqrt{u}}{\sigma^2}\right), \\
p_U(u|H_2, C) &= \frac{1}{2\sigma^2} \exp\left(-\frac{u + c^2}{2\sigma^2}\right) I_0\left(\frac{c\sqrt{u}}{\sigma^2}\right),
\end{aligned}
\tag{5.3}
$$

$$
\begin{aligned}
p_V(v|H_0) &= \frac{1}{2\sigma^2}\exp\bigg(\frac{-v}{2\sigma^2}\bigg), \\
p_V(v|H_1,A) &= \frac{1}{2\sigma^2}\exp\bigg(-\frac{u+(\omega_m a)^2}{2\sigma^2}\bigg)\, I_0\bigg(\frac{\omega_m a\sqrt{v}}{\sigma^2}\bigg), \\
p_V(v|H_2,C) &= \frac{1}{2\sigma^2}\exp\bigg(-\frac{v+((\omega_s/\delta)c)^2}{2\sigma^2}\bigg)\, I_0\bigg(\frac{(\omega_s/\delta)c\sqrt{v}}{\sigma^2}\bigg),
\end{aligned}
\tag{5.4}
$$

where, noise variance in the main and auxiliary channels, σ_s^2 and σ_r^2, are taken as $2\sigma^2$. Considering the SLB structure given in 5.2, P_{B} as a function of C, which is the amplitude of the interference signal in sidelobe, can be written as

$$
\begin{aligned}
P_{\mathrm{B}}(c) = &\ \mathrm{Prob}\bigg\{\frac{V}{U} > F|H_2, C\bigg\} \\
= &\int_0^\infty \int_0^{v/F} p_{U,V}(u,v|\mathrm{H}_2,C)dudv.
\end{aligned}
\tag{5.5}
$$

Equation (5.5) indicates that $P_{\mathrm{B}}(c)$ depends on the joint probability distribution function of U and V, $p_{U,V}(u,v)$, conditioned on H_2 hypothesis. Following to the results given in [19], P_{B} is derived as a function of C. Then, pdf of C is employed and $P_{\mathrm{B}}(c)$ is averaged with respect to C to derive P_{B} as follows

$$
P_{\mathrm{B}} = \int_0^\infty P_{\mathrm{B}}(c)p_C(c)dc. \tag{5.6}
$$

$P_{\mathrm{B}}(c)$ can be calculated as

$$
\begin{aligned}
P_{\mathrm{B}}(c) &= \int_0^\infty \int_0^{v/F} p_{U,V}(u,v|H_2,C)dudv, \\
&= \int_0^\infty p_V(v|H_2,C)dv \int_0^{v/F} p_U(u|H_2,C)du, \\
&= \int_0^\infty p_V(v|H_2,C)dv\bigg[1 - \int_{v/F}^\infty p_U(u|H_2)du\bigg].
\end{aligned}
\tag{5.7}
$$

In the second line of (5.7) independence of U and V are used since the noise in main and auxiliary channels, namely W_s and W_r are independent. The integral in the last line of the (5.7) can be written as

$$
\int_{v/F}^\infty p_U(u|H_2)du = \int_{v/F}^\infty \frac{1}{2\sigma^2}\exp\bigg(-\frac{u+c^2}{2\sigma^2}\bigg)\, I_0\bigg(\frac{c\sqrt{u}}{\sigma^2}\bigg), \tag{5.8}
$$

Using the definition of Marqum Q-function given in [33],

$$Q(a,b) = \int_{b^2}^{\infty} \frac{1}{2} \exp\left(-\frac{x+a^2}{2} \right) I_0\big(a\sqrt{x}\big)dx, \tag{5.9}$$

(5.8) can be written as

$$\int_{v/F}^{\infty} p_U(u|H_2)du = Q\left(\frac{c}{\sigma}, \sqrt{\frac{v}{F\sigma^2}} \right). \tag{5.10}$$

Inserting (5.10) into (5.5), $P_B(c)$ can be expressed as

$$P_{\mathrm{B}}(c) = \\ 1 - \int_0^{\infty} Q\left(\frac{c}{\sigma}, \sqrt{\frac{v}{F\sigma^2}} \right) \frac{1}{2\sigma^2} \exp\left(-\frac{v + ((\omega_s/\delta)c)^2}{2\sigma^2} \right) I_0\left(\frac{(\omega_s/\delta)c\sqrt{v}}{\sigma^2} \right) dv. \tag{5.11}$$

Then, using the following equation given in [33],

$$\begin{aligned} &\int_0^{\infty} \frac{1}{2\sigma_1^2} \exp\left(-\frac{x+\alpha_1^2}{2\sigma_1^2} \right) I_0\left(\frac{\alpha_1\sqrt{x}}{\sigma_1^2} \right) Q\left(\frac{\alpha_2}{\sigma_2}, \sqrt{\frac{x}{\sigma_2^2}} \right) dx = \\ &\frac{\sigma_1^2}{\sigma_1^2+\sigma_2^2} \left[1 - Q\left(\sqrt{\frac{\alpha_1^2}{\sigma_1^2+\sigma_2^2}}, \sqrt{\frac{\alpha_2^2}{\sigma_1^2+\sigma_2^2}} \right) \right] + \\ &\frac{\sigma_2^2}{\sigma_1^2+\sigma_2^2} \left[1 - Q\left(\sqrt{\frac{\alpha_2^2}{\sigma_1^2+\sigma_2^2}}, \sqrt{\frac{\alpha_1^2}{\sigma_1^2+\sigma_2^2}} \right) \right], \end{aligned} \tag{5.12}$$

where $\sigma_1 = \sigma$, $\sigma_2 = \sigma\sqrt{F}$, $\alpha_1 = \frac{\omega_s}{\delta}c$, $\alpha_2 = c\sqrt{F}$ and $x = v$; (5.11) can be simplified as

$$\begin{aligned} P_{\mathrm{B}}(c) = &\frac{F}{1+F} \left[1 - Q\left(\sqrt{\frac{2F\ \mathrm{INR}_0}{1+F}}, \frac{\omega_s}{\delta}\sqrt{\frac{2\ \mathrm{INR}_0}{1+F}} \right) \right] + \\ &\frac{1}{1+F}\, Q\left(\frac{\omega_s}{\delta}\sqrt{\frac{2\ \mathrm{INR}_0}{1+F}}, \sqrt{\frac{2F\ \mathrm{INR}_0}{1+F}} \right). \end{aligned} \tag{5.13}$$

The interference to noise ratio, INR_0, given in (5.13) is defined as

$$\mathrm{INR}_0 = \frac{c^2}{2\sigma^2}. \tag{5.14}$$

To derive P_{B} for Swerling 1 target model, (5.6) is employed,

$$\begin{aligned} P_{\mathrm{B}} = \int_0^{\infty} &\frac{F}{1+F} \left[1 - Q\left(\sqrt{\frac{2F\ \mathrm{INR}_0}{1+F}}, \frac{\omega_s}{\delta}\sqrt{\frac{2\ \mathrm{INR}_0}{1+F}} \right) \right] + \\ &\frac{1}{1+F}\, Q\left(\frac{\omega_s}{\delta}\sqrt{\frac{2\ \mathrm{INR}_0}{1+F}}, \sqrt{\frac{2F\ \mathrm{INR}_0}{1+F}} \right) \frac{c}{\sigma_C^2} \exp\left(\frac{-c^2}{2\sigma_C^2} \right) dc. \end{aligned} \tag{5.15}$$

Result of (5.15) can be turned into a closed form expression, as proven in [30],

$$P_{\mathrm{B}} = \frac{1}{2}\Bigg[1 - \frac{1}{1+F}\frac{\mathrm{INR}(F-(\omega_s/\delta)^2)-(F+1)}{\sqrt{\big[\,\mathrm{INR}(F-(\omega_s/\delta)^2)+F+1\big]^2+4\,\mathrm{INR}(F+1)F}} - \frac{F}{1+F}\frac{\mathrm{INR}(F-(\omega_s/\delta)^2)+F+1}{\sqrt{\big[\mathrm{INR}(F-(\omega_s/\delta)^2)-(F+1)\big]^2+4\,\mathrm{INR}(F+1)F}}\Bigg]. \tag{5.16}$$

Note that interference to noise ratio is now taken as

$$\mathrm{INR} = \frac{E\{c^2\}}{2\sigma^2} = \frac{\sigma_C^2}{2\sigma^2}, \tag{5.17}$$

where σ_C^2 is the average power of the fluctuating interference in the sidelobe as shown in (5.2).

To evaluate the performance of the SLB structure, P_{TB} is also to be derived. Considering the SLB structure, P_{TB} as a function of A, which is the amplitude of the target in the mainlobe, can be written as

$$\begin{aligned} P_{TB}(a) &= \mathrm{Prob}\left\{\frac{V}{U} > F|H_1, A\right\} \\ &= \int_0^{\infty}\int_0^{v/F} p_{U,V}(u, v|\mathrm{H}_1, A)\,du\,dv. \end{aligned} \tag{5.18}$$

Following the same steps with the derivation of P_{B}, a closed form expression for P_{TB} can be found as ,[30]

$$P_{TB} = \frac{1}{2}\Bigg[1 - \frac{1}{1+F}\frac{\mathrm{SNR}(F-\omega_m^2)-(F+1)}{\sqrt{\big[\,\mathrm{SNR}(F-\omega_m^2)+F+1\big]^2+4\,\mathrm{SNR}(F+1)F}} - \frac{F}{1+F}\frac{\mathrm{SNR}(F-\omega_m^2)+F+1}{\sqrt{\big[\,\mathrm{SNR}(F-\omega_m^2)-(F+1)\big]^2+4\,\mathrm{SNR}(F+1)F}}\Bigg]. \tag{5.19}$$

SNR denotes the signal to noise ratio and it can be written as

$$\mathrm{SNR} = \frac{E\{a^2\}}{2\sigma^2} = \frac{\sigma_A^2}{2\sigma^2}, \tag{5.20}$$

where σ_A^2 is the average power of the fluctuating target in the mainlobe.

5.3 Numerical Results

In this part of the thesis, performance of the proposed auxiliary antenna pattern is presented quantitatively for various cases. To examine the efficiency of the proposed pattern, a new parameter, x (shown in Figure 5.3), is employed. This parameter denotes the ratio between the sidelobe and the mainlobe level of the auxiliary pattern

$$x = \frac{\omega_s^2}{\omega_m^2}. \tag{5.21}$$

When $x = 1$, the results correspond to the conventional SLB performance, and the proposed SLB performance will be observed when $x > 1$.

During the analyses, main antenna gain is kept at 0 dB. The effect of x on the system performance is investigated for varying SNR, INR, δ^2 and ω_s^2.

The first example demonstrates the probability of blanking, P_B, against the parameter x by setting the probability of target blanking, P_{TB} at a desired value for the Swerling-1 target model which is given in (5.16). In fact, having the probability of target blanking, P_{TB}, constant and INR as a parameter, the probability of blanking, P_B, is plotted as a function of x for different cases. The desired value for the probability of target blanking, P_{TB}, is obtained considering the value of the minimum detectable target SNR and applying (5.18).

In the first case to be evaluated, the minimum detectable target SNR is assumed to be 20 dB. The probability of target blanking, P_{TB}, is calculated as a function of threshold, F, for that SNR value and for the antenna parameters given in Table 5.1 in a conventional SLB structure, i.e. when $x = 0$ dB.

Table 5.1: Antenna parameters

Value	**Explanation**
-20 dB	δ_s^2
-10 dB	ω_s^2

It is desired to have the minimum target blanking probability. Considering Figure 5.4, that can be realized when the threshold, F, is at its maximum. Note that the maximum value of the threshold is limited to β^2, i.e. $F_{max} = \beta^2$.

Otherwise, blanking performance of the SLB degrades in a considerable manner [12].

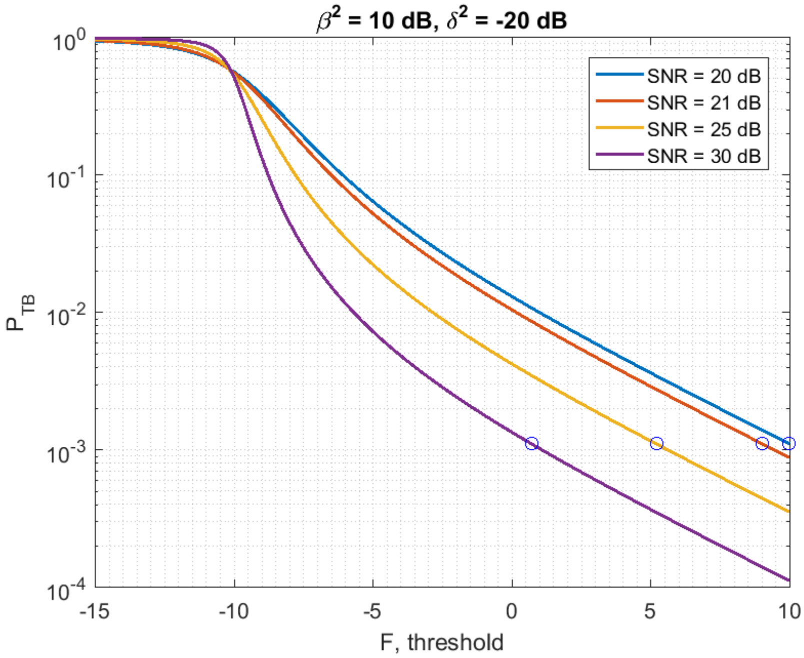

Figure 5.4: Probability of target blanking, P_{TB}, as a function of threshold, F.

In the first case, the performance of the proposed SLB is studied with an antenna having a poor peak to sidelobe (PSL) ratio as defined in Table 5.1. The minimum value of the probability of target blanking, P_{TB}, is found as 0.001 at $F = \beta^2$ for 20 dB SNR.

In Figure 5.5, SNR is increased while keeping the probability of target blanking, P_{TB}, constant at 0.001. This causes SLB structure to be over-designed as SNR is increased over 20 dB.

Figure 5.5 also indicates that the larger the parameter x is, the higher the probability of blanking, P_B is to be reached. Especially for the value of the minimum detectable SNR, the effect of the parameter x on the blanking performance of the system can be observed clearly. This effect is decreasing with increasing SNR for a constant P_{TB}.

INR values given in Figure 5.5 refer to the interference to noise ratio of the interfering source in the main channel. It is also observed from Figure 5.5 that

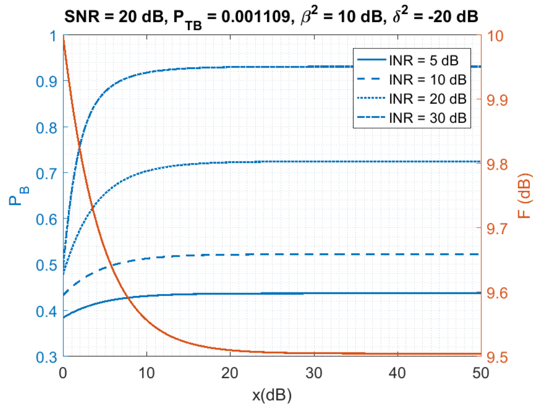

(a) P_B vs x at SNR = 20 dB

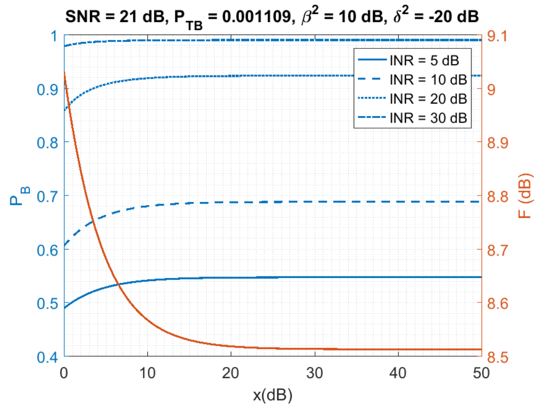

(b) P_B vs x at SNR = 21 dB

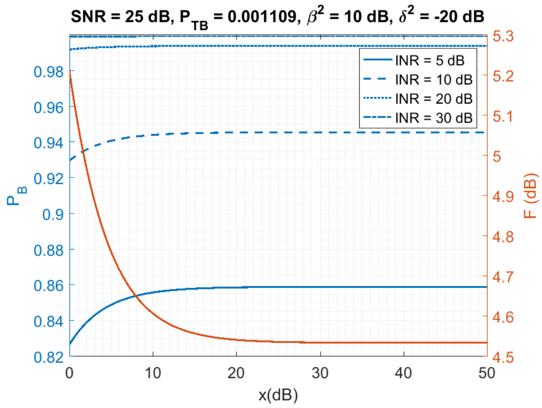

(c) P_B vs x at SNR = 25 dB

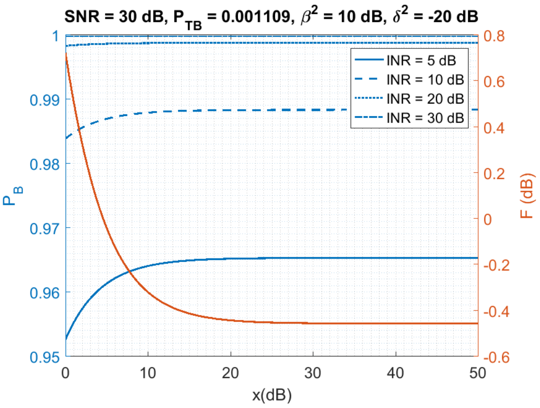

(d) P_B vs x at SNR = 30 dB

Figure 5.5: Probability of blanking, P_B, as a function of x for various INR. Left y-axes denotes the probability of blanking, P_B, and the right y-axes indicates the threshold values for the same x-axes.

the blanking probability, P_B, increases as INR gets larger. This is quite expected since the presence of an interference is more obvious with increasing INR in a noisy channel. Another result that can be drawn from the Figure 5.5 is that improving the value of x over 20 dB does not change the performance in a significant manner.

Figure 5.5c and Figure 5.5d show over-designed SLB structures because more appropriate values for probability of target blanking, P_{TB}, could be selected for that values of SNR. In a real scenario, the threshold, F, is set to a fixed value. Therefore, to show the blanking performance for a fixed threshold, F, Figure 5.6 is plotted.

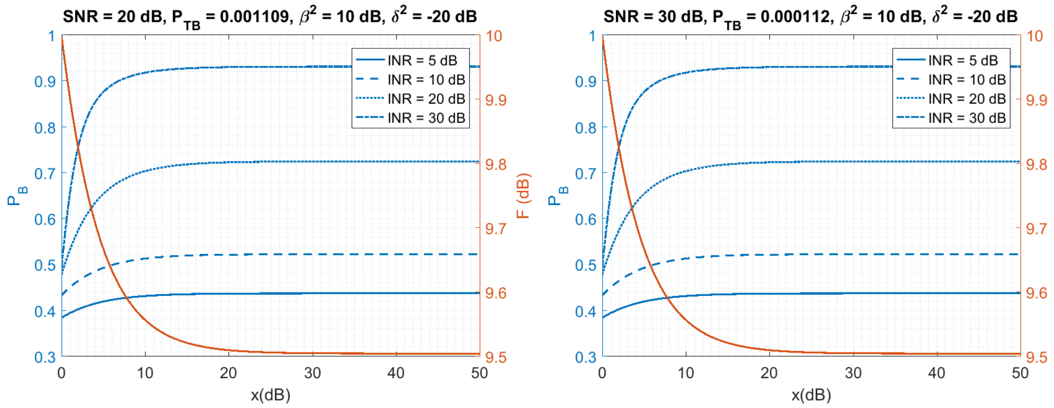

(a) P_B vs x at SNR $=$ 20 dB

(b) P_B vs x at SNR $=$ 30 dB

Figure 5.6: Probability of blanking, P_B, as a function of x for various INR. Left y-axes denotes the probability of blanking, P_B, and the right y-axes indicates the threshold values for the same x-axes.

Figure 5.6 points out that the increment in SNR causes a decrease in P_{TB} due to the constant threshold values. The only parameter changing threshold, F, is the ratio between the sidelobe and the mainlobe level of the auxiliary antenna, x.

It is observed from Figure 5.6 that if the threshold is selected as $F = \beta^2$, the effect of the proposed method will be dramatic. In addition, this effect does not depend on the target SNR when the threshold, F, is fixed.

In Figure 5.6, the threshold is selected as the maximum possible value, $F = \beta^2$, when $x = 0$ dB. Hereby, that value of the threshold, F, is lowered and Figure 5.7 is plotted.

In Figure 5.7, the improvement in blanking probability is not as drastic as in Figure 5.6. Hence, it can be inferred that the performance of the SLB is sensitive to the value of the parameter x when the threshold, F, is selected close to β^2.

Another way to investigate the effect of x on the system performance when the threshold, F, is taken as constant is to plot the probability of target blanking, P_{TB}, as a function of SNR for different values of x. In Figure 5.8, the probability of target blanking, P_{TB}, is drawn for the antenna parameters given in Table 5.1.

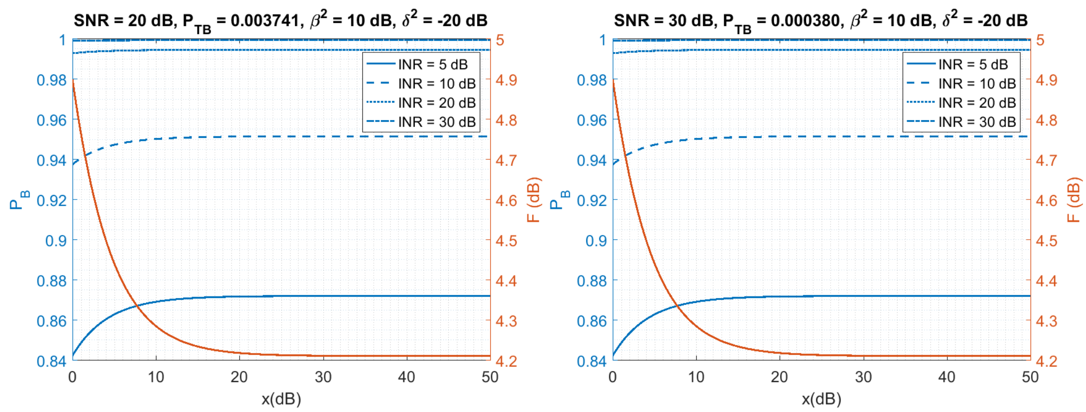

(a) P_B vs x at SNR = 20 dB

(b) P_B vs x at SNR = 30 dB

Figure 5.7: Probability of blanking, P_B, as a function of x for various INR.Left y-axes denotes the probability of blanking, P_B, and the right y-axes indicates the threshold values for the same x-axes.

In Figure 5.8, it can be observed that increasing the value of the parameter x creates a performance gap. This gap is decreasing for improved values of SNR. The effect of x can be seen more clearly in Figure 5.8b which is more detailed version of Figure 5.8a around 20 dB SNR. According to Figure 5.8b, 5 dB increment on x, will improve the performance 0.35 dB, i.e. the same probability of target blanking, P_{TB}, can be provided with targets having 0.35 dB smaller SNR. In addition, 10 dB increase on x, will improve the target blanking performance approximately by 0.45 dB. The improvement on x over 20 dB does not contribute to the system performance beyond 0.5 dB.

It is worthy of note that the foregoing results belong to an antenna having a poor PSL ratio. Now, the antenna parameters are improved to a typical radar example that are given in Table 5.2. Note that β^2 is still kept at 10 dB.

Table 5.2: Antenna parameters

Value	**Explanation**
−30 dB	δ_s^2
−20 dB	ω_s^2

In Figure 5.9, the probability of target blanking performance of the antenna is plotted as a function of threshold. The maximum threshold, F, gives the value

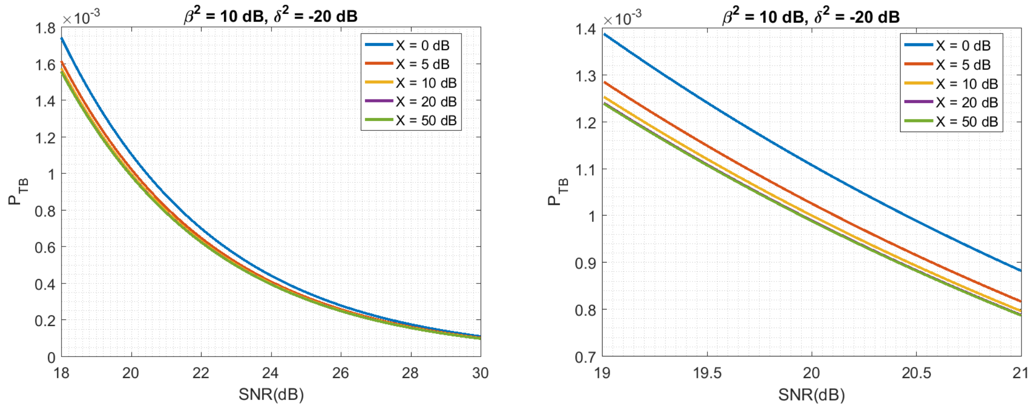

(a) P_{TB} vs SNR for various x (b) P_{TB} vs SNR for various x

Figure 5.8: Probability of target blanking, P_{TB}, as a function of SNR, F.

of minimum probability of target, P_{TB}. P_{TB} is found as 0.001 for 20 dB SNR and $F = \beta^2$.

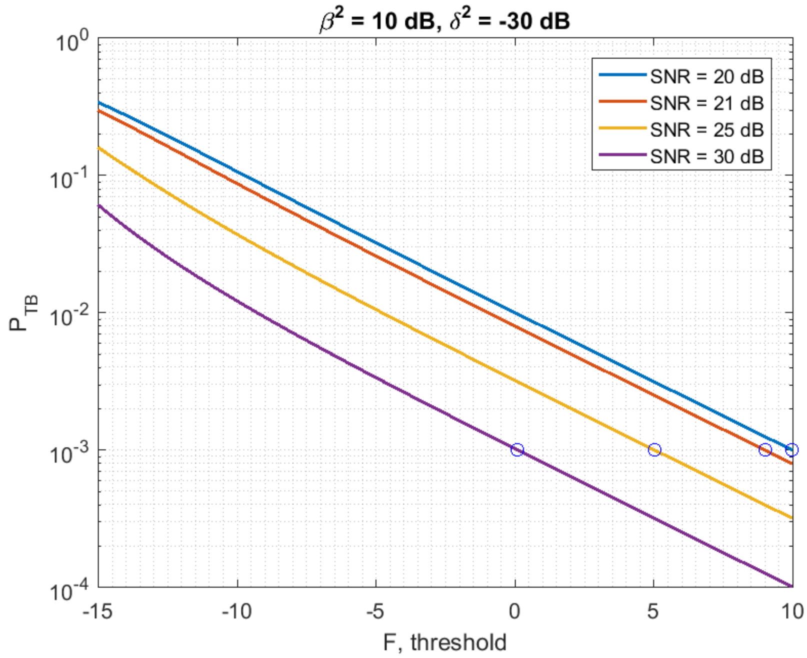

Figure 5.9: Probability of target blanking, P_{TB}, as a function of threshold, F.

In Figure 5.10, the probability of target blanking, P_{TB} is kept constant at 0.001 for various SNR values. This makes the threshold, F, decrease as SNR is increased. As in 5.5, the system becomes overdesigned when SNR is improved.

In Figure 5.10a improvement on blanking performance is apparent. However, it

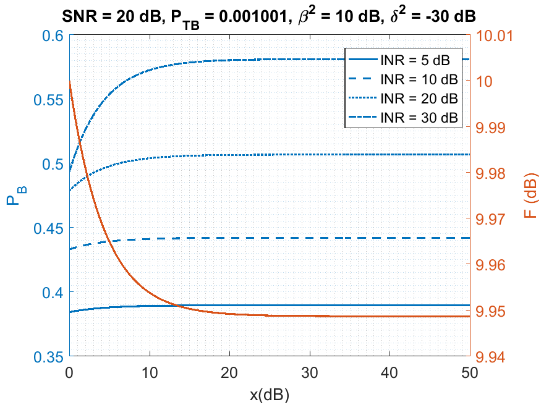

(a) P_B vs x at SNR $=$ 20 dB

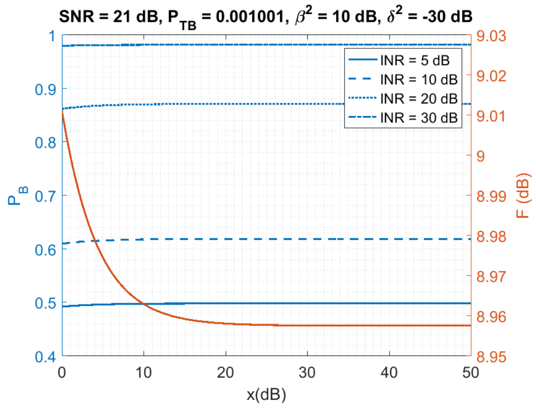

(b) P_B vs x at SNR $=$ 21 dB

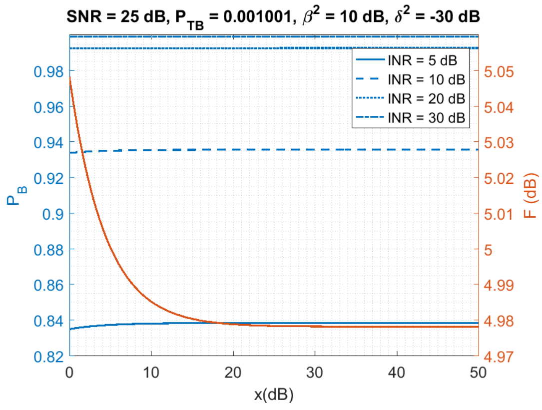

(c) P_B vs x at SNR $=$ 25 dB

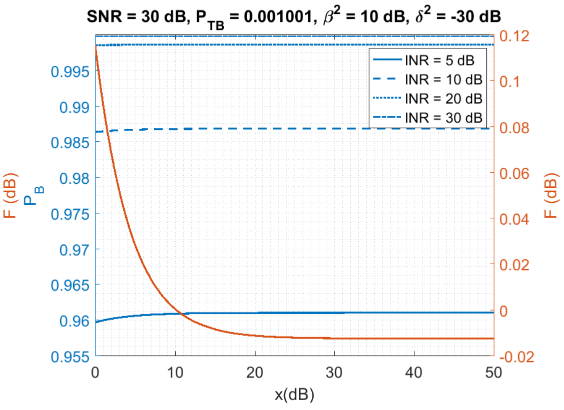

(d) P_B vs x at SNR $=$ 30 dB

Figure 5.10: Probability of blanking, P_B, as a function of x for various INR. Left y-axes denotes the probability of blanking, P_B, and the right y-axes indicates the threshold values for the same x-axes.

is degraded when compared to Figure 5.5a. Since the antenna parameters are improved, the effect of x on the system performance is substantially reduced for high SNR values. Especially in Figure 5.10b, 5.10c and 5.10d, amelioration provided by the parameter x is almost negligible.

It is also observed that the probability of blanking, P_B, is increased when compared to Figure 5.5 at $x = 0$ dB. It is an expected result due to the development on the antenna PSL. This result shows that the parameter x is more functional when the PSL is low and the threshold, F, is set close to β^2.

Note that the effect of constant threshold on blanking performance for various

SNR was studied and it was shown that the probability of blanking, P_B, depends on the threshold, F, rather than the SNR. Therefore, in Figure 5.6 and 5.7, the same probability of blanking, P_B, performances were observed against different SNR values. The effect of x when the threshold, F, is kept constant is shown by means of drawing the probability of target blanking, P_{TB}, performance as a function of SNR in Figure 5.11.

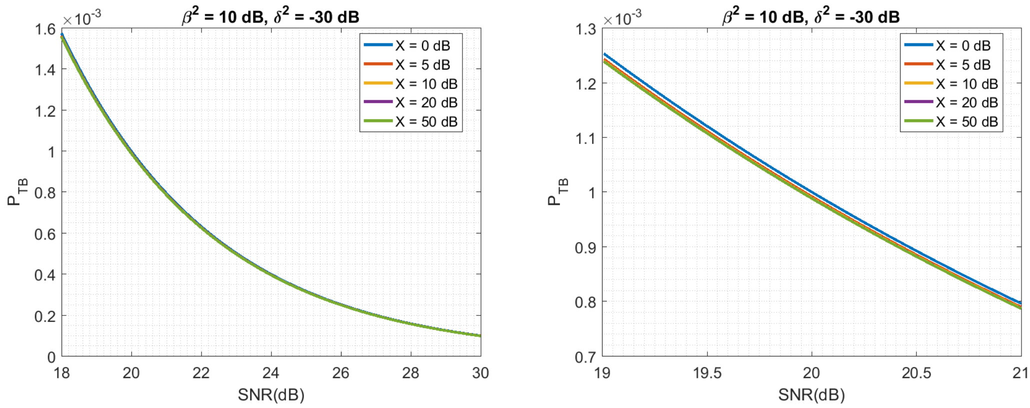

(a) P_{TB} vs SNR for various x (b) P_{TB} vs SNR for various x

Figure 5.11: Probability of target blanking, P_{TB}, as a function of SNR, F.

In Figure 5.11, performance gap induced by parameter x is very small compared to the Figure 5.8. It can be observed that there is no contribution of improving the parameter x beyond 10 dB to the probability of target blanking, P_{TB}. The advantage provided by 10 dB improvement on x is 0.05 dB. This result shows that the contribution of x on the system performance is negligible for antennas having good PSLs.

In summary, the proposed auxiliary pattern better the performance of the SLB in terms of the probability of blanking, P_B, and the probability of target blanking, P_{TB}, when antenna sidelobe levels are poor. However, its gain is reduced in a significant manner when antenna sidelobe levels are improved. It is also observed that if the threshold, F, is not kept at the maximum level, the effect of the parameter x on the system performance will be small.

5.4 Implementation of SLB in Subspace

This section deals with the SLB design in beamspace which is formed by eigenvector beamformer studied in Chapter 3. The conventional Maisel's SLB structure is to be implemented in the beamspace. However, the design of an auxiliary antenna pattern is the main problem. Using an auxiliary antenna may not be feasible due to complexity in practice. Another solution could be the implementation of the auxiliary antenna using the full dimension. In fact, auxiliary pattern can be assigned to one of the beamspace channels having the minimum eigenvalue. This means that the column of the beamspace matrix with the minimum eigenvalue can be used for the generation of the auxiliary pattern. In contrast, losing dimensions, even only one, might degrade the performance of detection as discussed in Chapter 3 and 4. In order to avoid such performance degradations, an extra column can be added to beamspace matrix instead of removing a detection channel. In fact, that channel is used to represent SLB auxiliary pattern. In this way, computational work is increased and that might cause problems in practical systems.

Taking the foregoing discussion into account, design of the auxiliary pattern in beamspace will be studied in this part of the thesis. This approach reduces computational work because an extra channel is not assigned to SLB during dimension reduction and SLB channel is synthesized digitally after beamspace construction.

The implementation of the SLB structure in beamspace is presented in Figure 5.12.

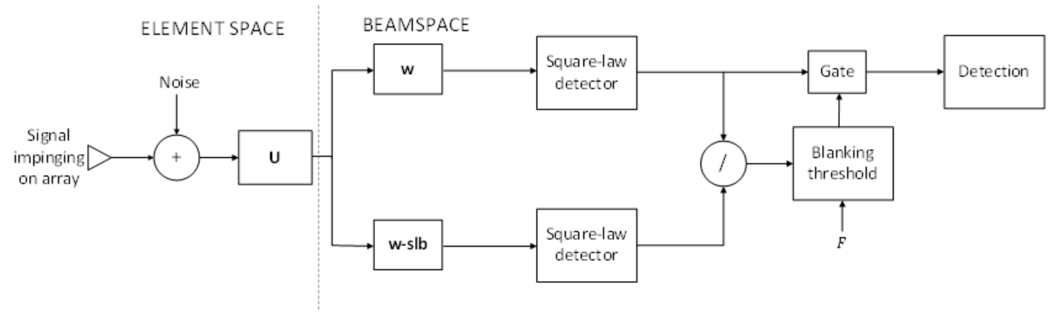

Figure 5.12: Sidelobe blanking structure in beamspace.

As explained in the previous part, outputs of the square-law detectors are evaluated considering the working principle of SLB. In order to provide a proper assessment, the beamspace SLB coefficients, w_{SLB}, have to be chosen carefully.

The auxiliary pattern in beamspace can be formulated considering the previously derived equations (4.4) and (4.8) as follows

$$\mathbf{P}_{\text{SLB}}(\phi) \;=\; \frac{\mid \mathbf{w}_{\text{SLB}}^{\mathbf{H}}\ \mathbf{U}^{\mathbf{H}}\ \mathbf{a}(\phi)\mid^2}{\|\ \mathbf{w}_{\text{SLB}}^{\mathbf{H}}\ \mathbf{U}^{\mathbf{H}}\ \|^2}. \tag{5.22}$$

where $\mathbf{w}_{\text{SLB}}$ refers to the beamspace auxiliary beamformer, $\mathbf{U}$ is the beamspace matrix and $\mathbf{a}(\phi)$ is the steering vector belonging to the echos coming from ϕ.

Considering the beamspace width given in Table 3.1, the desired SLB pattern to be achieved is given in Figure 5.13.

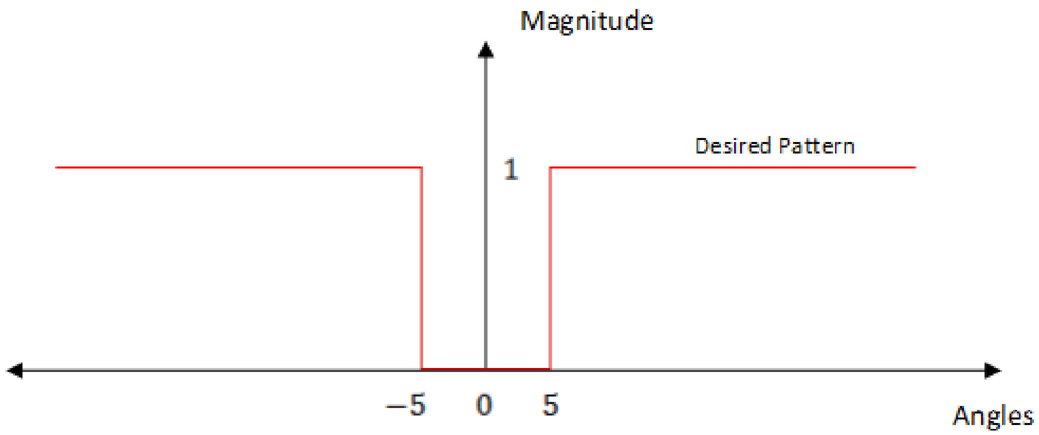

Figure 5.13: Desired sidelobe blanker pattern, $\text{P}_{\text{desired}}(\phi)$

$\mathbf{w}_{\text{SLB}}$ can be found by minimizing the difference between the desired and the calculated SLB pattern

$$\begin{aligned} &\min_{\mathbf{w}_{\text{SLB}}}\ \max_{\phi}\ \text{G}_{\phi}(\mathbf{w}_{\text{SLB}}) \\ \text{G}_{\phi}(\mathbf{w}_{\text{SLB}}) &= \mid \text{P}_{\text{desired}}(\phi) - \text{P}_{\text{SLB}}(\phi, \mathbf{w}_{\text{SLB}}) \mid \end{aligned} \tag{5.23}$$

where $\text{P}_{\text{SLB}}(\phi, \mathbf{w}_{\text{SLB}})$ means SLB pattern evaluated at $\mathbf{w}_{\text{SLB}}$ and ϕ. To realize that MATLAB-fminimax optimization tool is used. Figure 5.14 shows the resulting optimized pattern for various dimensions.

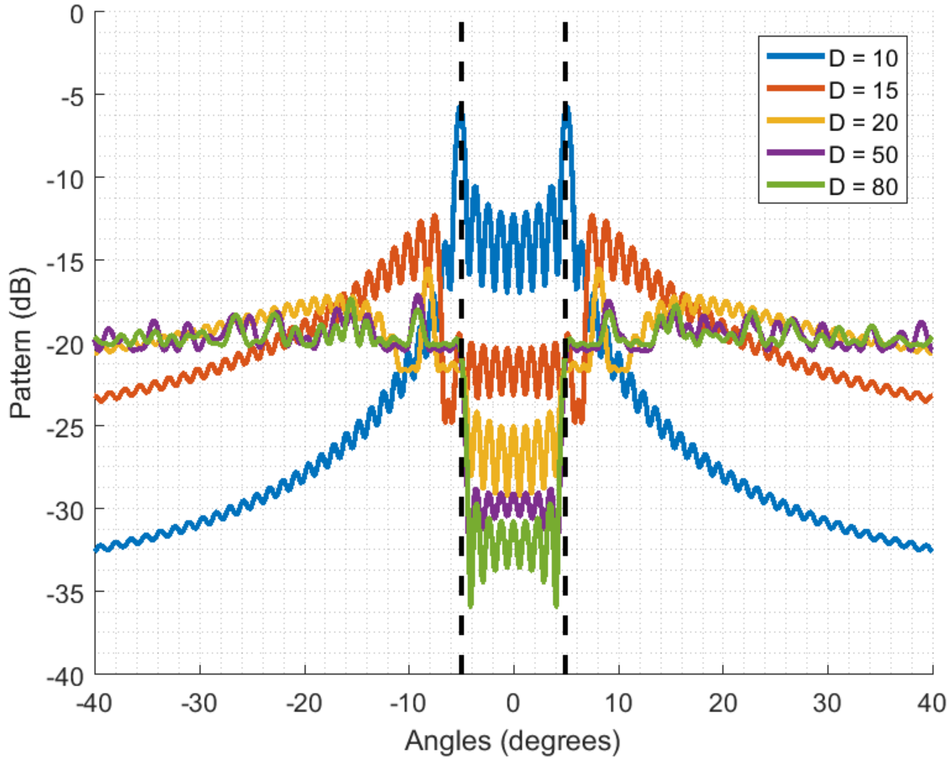

Figure 5.14: Designed auxiliary pattern in beamspace for various dimensions.

Notice that since the array has 100 elements, normalized omnidirectional pattern can only be provided at -20 dB. Due to the reduced number of channels, the optimization cannot provide a smooth pattern as the desired one. As the number of reduced dimensions increases, optimized beamspace SLB pattern begins to converge to the desired one.

In the foregoing part, a proper auxiliary pattern is generated to be used in SLB system. Now, the idea of constructing SLB pattern in beamspace is extended to a more realizable case where tapering is applied. Tapering was discussed in Chapter 4. It was stated that tapering is the underlying remedy to deal with the interferers. However, it was also noted that applying only tapering might be inadequate in the presence strong interferers and thereby SLB process was proposed.

In Chapter 4, tapering was examined in two ways, namely tapering before dimension reduction and tapering after dimension reduction. Tapering before dimension reduction refers to the conventional tapering in the element space.

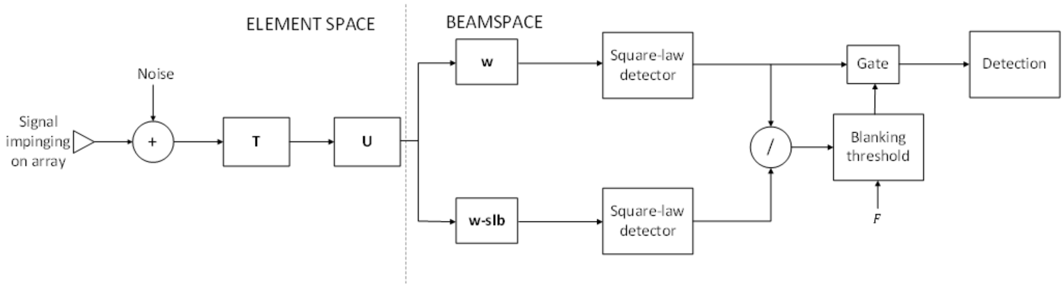

Figure 5.15: Sidelobe blanking structure in tapered beamspace.

Then, tapered data is used to form the reduced dimensional space. Therefore, this method provides tapered channels in beamspace and the auxiliary pattern design is to be realized via these tapered channels. Tapering after dimension reduction method, on the other hand, utilizes beamspace channels constructed with no tapering information. That allows forming the auxiliary pattern from non-tapered channels, contrary to tapering before dimension reduction method. In other words, since tapering is performed in beamspace, the auxiliary pattern is not affected by the tapering operation. Hence, the formulation of the auxiliary pattern can be taken as in (5.22). However, when the method of tapering before dimension reduction is employed, the pattern of the auxiliary channel changes and can be formulated as

$$\mathbf{P}_{\mathrm{TSLB}}(\phi) \;=\; \frac{\mid \mathbf{w}_{\mathrm{TSLB}}^{\mathbf{H}}\ \mathbf{U}^{\mathbf{H}}\ \mathbf{T}^{\mathbf{H}}\ \mathbf{a}(\phi)\mid^{2}}{\left\| \mathbf{w}_{\mathrm{TSLB}}^{\mathbf{H}}\ \mathbf{U}^{\mathbf{H}}\ \mathbf{T}^{\mathbf{H}} \right\|^{2}}, \tag{5.24}$$

where, $\mathbf{P}_{\mathrm{TSLB}}$ refers to the pattern of the auxiliary channel generated using tapered subspace. (5.24) differs from (5.22) by a diagonal tapering matrix, $\mathbf{T}$. Since an additional diagonal tapering matrix appeared in the formula, optimization routine is revised as follows:

$$\begin{aligned} &\min_{\mathbf{w}_{\mathrm{SLB}}}\ \max_{\phi}\ \mathrm{G}_{\phi}(\mathbf{w}_{\mathrm{TSLB}}) \\ \mathrm{G}_{\phi}(\mathbf{w}_{\mathrm{TSLB}}) &= \mid \mathrm{P}_{\mathrm{desired}}(\phi) - \mathrm{P}_{\mathrm{TSLB}}(\phi, \mathbf{w}_{\mathrm{TSLB}}) \mid. \end{aligned} \tag{5.25}$$

Figure 5.16 demonstrates the effect of tapering by comparing the auxiliary patterns of the tapered and non-tapered beamspaces for various number of dimensions.

In Figure 5.16, it is indicated that the resultant auxiliary pattern obtained using the conventional tapering, i.e. tapering before dimension reduction, has

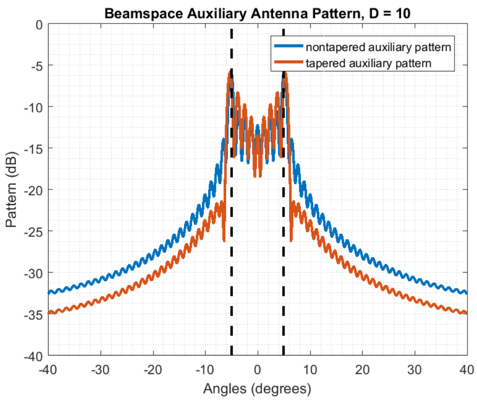

(a) Beamspace auxiliary patterns vs angles when D = 10

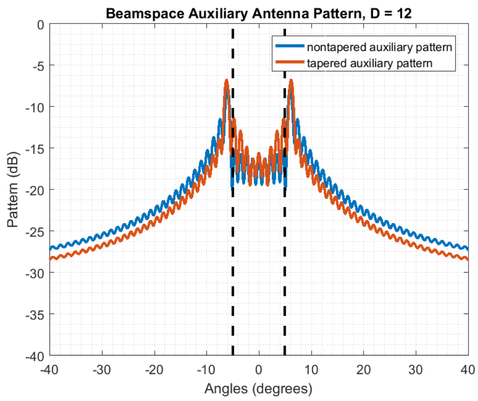

(b) Beamspace auxiliary patterns vs angles when D = 12

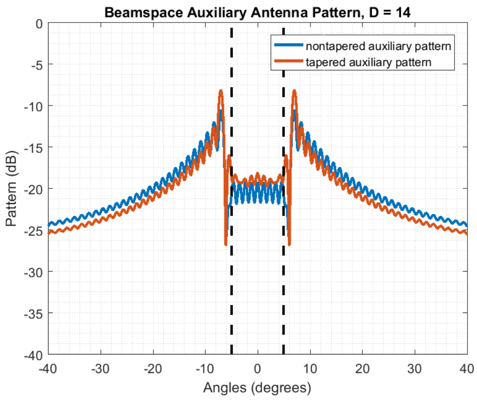

(c) Beamspace auxiliary patterns vs angles when D = 14

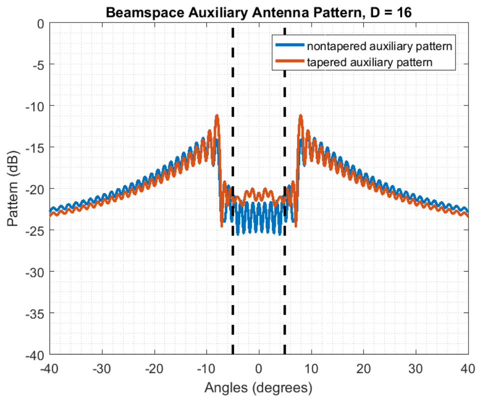

(d) Beamspace auxiliary patterns vs angles when D = 16

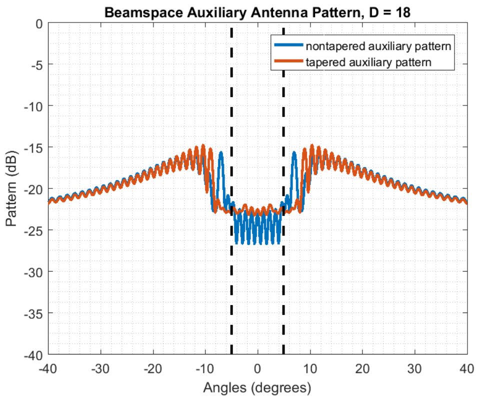

(e) Beamspace auxiliary patterns vs angles when D = 18

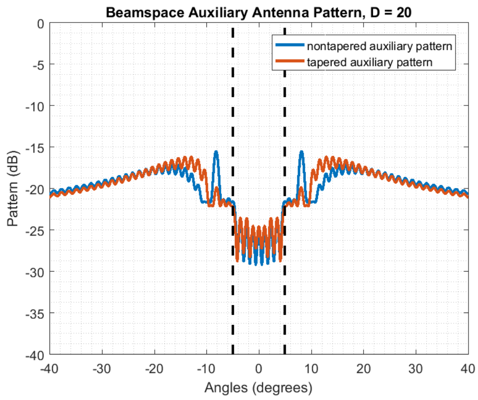

(f) Beamspace auxiliary patterns vs angles when D = 20

Figure 5.16: Auxiliary patterns designed in tapered and nontapered beamspaces for various number of dimensions.

lower sidelobes and higher main lobe compared to the non-tapered one, i.e. tapering after dimension reduction. That is an expected result since tapering phenomenon causes information loss outside the sector by minimizing the sidelobes of the beamspace vectors. However, it can also be observed that as the number of dimensions increases, the offset between the auxiliary pattern levels of both tapered and nontapered beamspaces reduces and they both converge to the desired pattern.

In order to observe the effect of beamspace dimension on the pattern of the auxiliary channel in tapered beamspace clearly, Figure 5.17 is provided. It is

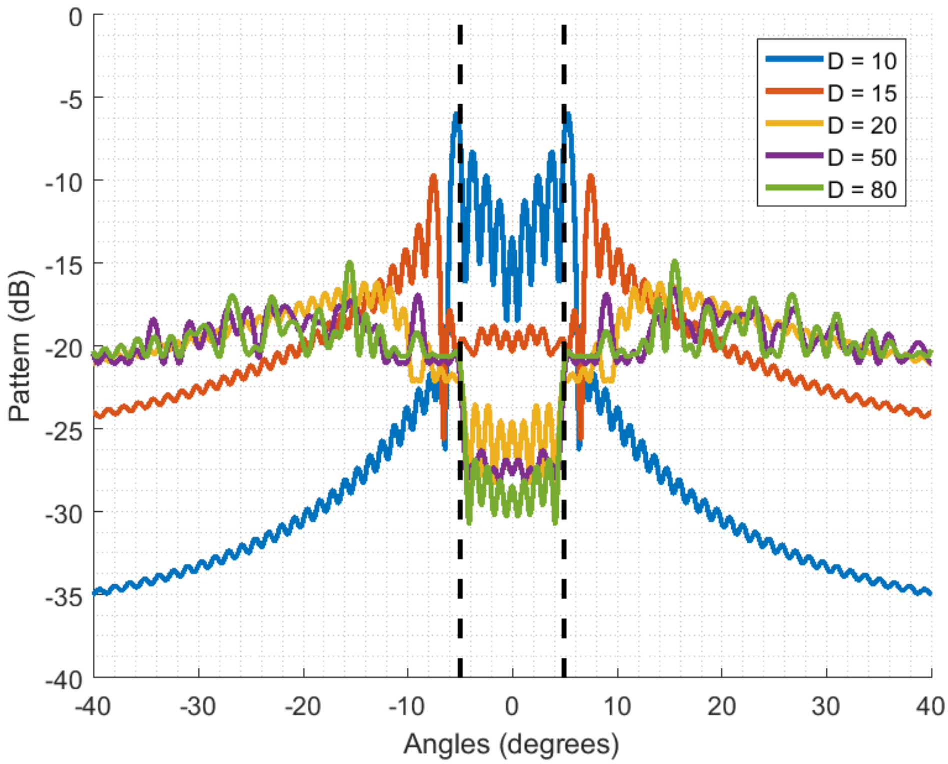

Figure 5.17: Designed auxiliary patterns in tapered beamspace for various number of dimensions.

inferred from Figure 5.17 that even though tapering is employed before forming the beamspace, the desired auxiliary pattern can be achieved if the number of reduced beampsace channels is increased towards the full dimension. However, comparing Figure 5.14 and 5.17, it can also be seen that even if the beamspace dimension is increased too much, nontapered beamspace auxiliary pattern converges to the desired pattern better than the tapered one.

In order to give an insight into the SLB performance, the main beam and the auxiliary beam should be evaluated jointly. Therefore, Figure 5.18 and 5.19 are plotted to demonstrate the detection and the auxiliary patterns for both tapering after dimension reduction and tapering before dimension reduction methods. To develop a feeling about the importance of the beamspace dimension, detection beam is steered towards the edge of the sector as in Chapter 4. Figure 5.18 indicates that employing 10 channels is not enough to implement SLB in beamspace for the case where the angular width is taken as 10 degree. 12 or higher number of reduced dimensions seems quite enough for SLB to work properly. In Figure 5.19, on the other hand, at least 16 beamspace dimensions are required for the SLB to function in beamspace. In fact, tapering after beamspace dimension requires more dimension than tapering before beamspace operation. That requirement was also mentioned in Chapter 4. In Figure 4.6, it was observed that beamspace after dimension reduction method needs excessive number of additional channels to construct detection beams properly. It is worthy of note that as stated in Chapter 4, at least 13 dimensions are necessary for tapering before dimension reduction. In this analysis, this requisite is preserved and shown that axuiliary pattern can be designed with 13 number of channels. Besides, the dimension requirement for tapering after dimension reduction method was declared as 17 in Chapter 4. Although the auxiliary pattern can be well designed in smaller dimensions with tapering after dimension reduction, 17 dimensions are required to implement SLB since detection beam cannot be formed otherwise.

In summary, the aim of implementing SLB in beamspace and the generation of the auxiliary pattern using the reduced number of dimensions is achieved. Moreover, the effect of tapering on the SLB processing in beamspace is evaluated. It has been inferred that even if there is a performance gap when compared to the full dimension, employing SLB in beamspace and designing the axuiliary pattern using beamspace channels can work properly in many cases and be preferred for many practical purposes.

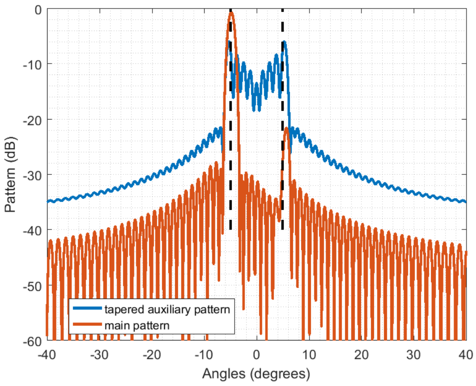

(a) Beamspace main and auxiliary patterns vs angles when D = 10

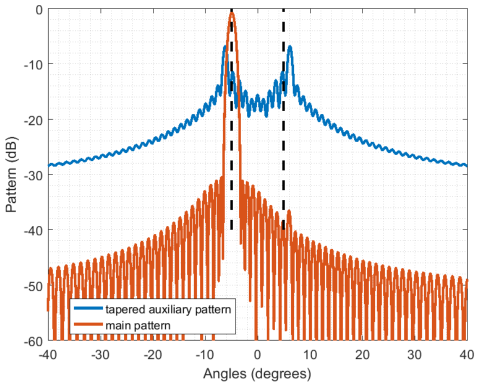

(b) Beamspace main and auxiliary patterns vs angles when D = 12

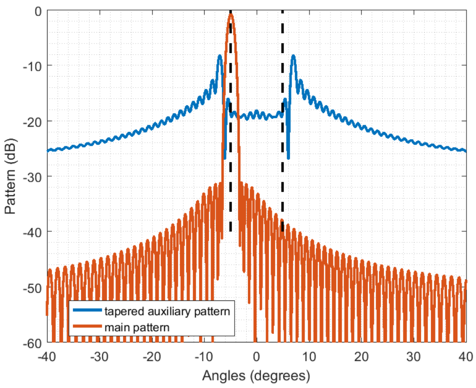

(c) Beamspace main and auxiliary patterns vs angles when D = 14

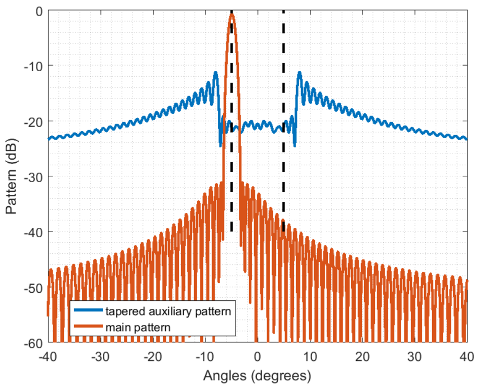

(d) Beamspace main and auxiliary patterns vs angles when D = 16

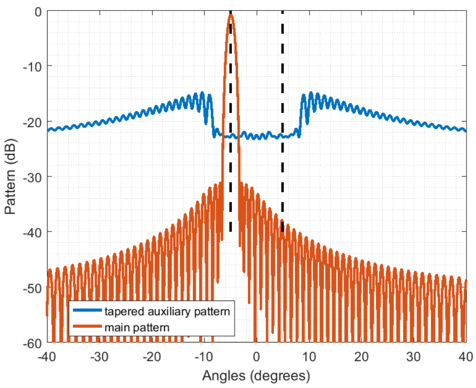

(e) Beamspace main and auxiliary patterns vs angles when D = 18

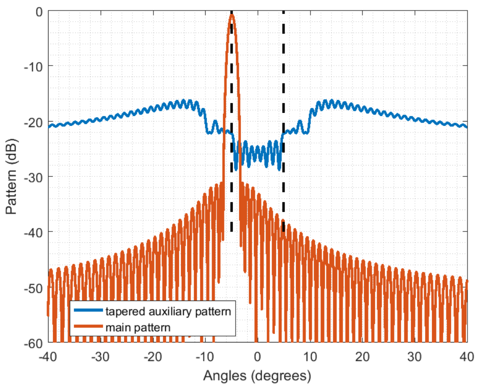

(f) Beamspace main and auxiliary patterns vs angles when D = 20

Figure 5.18: Main and auxiliary patterns designed in tapered (tapering in element space) beamspace for various number of dimensions.

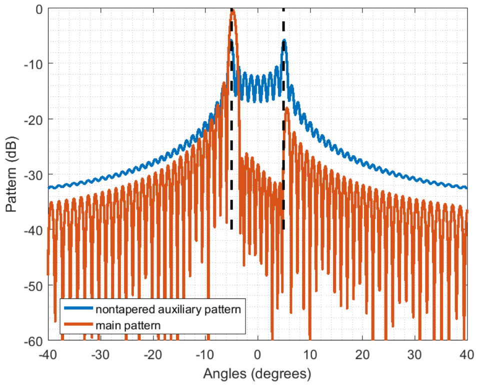

(a) Beamspace main and auxiliary patterns vs angles when D = 10

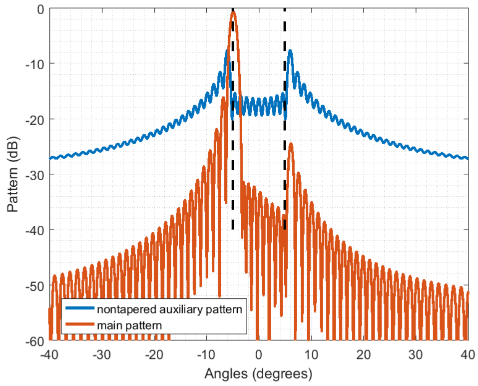

(b) Beamspace main and auxiliary patterns vs angles when D = 12

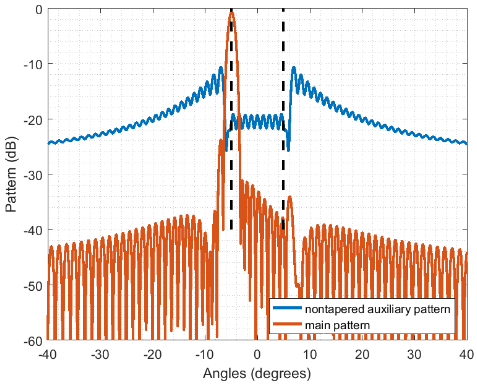

(c) Beamspace main and auxiliary patterns vs angles when D = 14

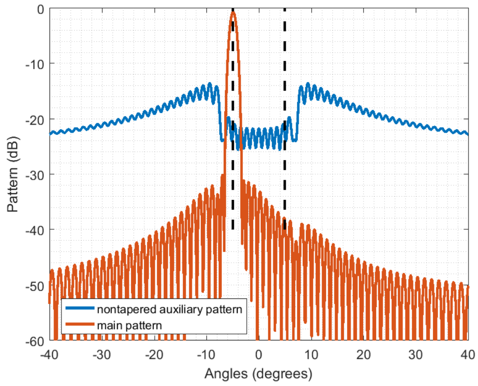

(d) Beamspace main and auxiliary patterns vs angles when D = 16

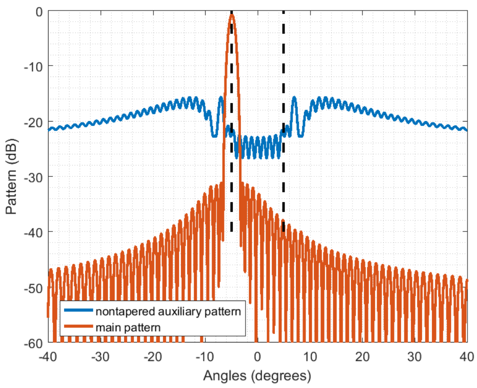

(e) Beamspace main and auxiliary patterns vs angles when D = 18

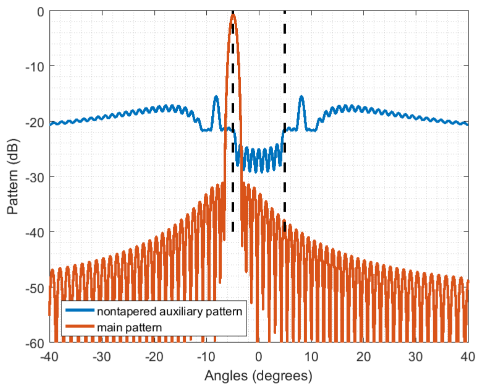

(f) Beamspace main and auxiliary patterns vs angles when D = 20

Figure 5.19: Main and auxiliary patterns designed in tapered (tapering in beamspace) beamspace for various number of dimensions.

CHAPTER 6

CONCLUSIONS

6.1 Thesis Summary

In this thesis, the subspace based phased array radar system enabling the processing of large dimensional arrays' data is studied and its performance is analyzed in terms of detection and parameter estimation criteria. In addition, several radar signal processing methods have been developed for array tapering and sidelobe blanking in accordance with the subspace reduction operation. The main objective of this thesis is to find a set of basis that can capture the essence of the information in a predefined sector by investigating the eigenvector and Fourier basis of that region of space. The second objective is to apply to the well-known spatial operations, namely array tapering and sidelobe blanking, in the reduced dimensional subspace.

Research on dimension reduction for large arrays shows that mapping the full dimensional data to the subspace can be performed by linear combinations of array elements with non-adaptive weights. This process is named as the reduced dimension beamspace processing which can be performed by projecting the large arrays' data via the beamspace matrix consisting of basis vectors of the subspace. In the scope of this thesis, two different bases, namely eigenvector and Fourier bases, have been investigated. It is seen that there is no conventional way to decide the number of reduced dimensions. Hence, a rule is proposed to determine the number of reduced dimensions which calculates the average energy in the sector and assigns a threshold. The number of beams satisfying that threshold is taken as subspace dimension. Then, the eigenvector beamformer and DFT beamformer are implemented regarding to this rule and qualitative comparison between them is presented considering their detection and parameter estimation performances. The results indicate that eigenvector beamformers achieve the optimum criterion in the MSE sense, i.e. the minimum average SNR loss in the sector can be attained by eigenvector beamformer. It is proved that eigenvector beamformer can provide the optimum subspace in the MSE sense, while it is illustrated that DFT beamformer can achieve better results in minimax sense. In other words, the maximum SNR loss in the sector can be minimized by DFT beams. It is worth to underline that minimax performance of DFT beamformer can only be achieved when DFT beams are chosen properly. It is observed that when the beams do not cover the whole sector, the ability of the DFT beamformer to detect targets situated in some angular regions of the sector decreases. Even if they attain different optimality criteria, simulations performed in 3.6 illustrate that both eigenvector beamformer and DFT beamformer exhibit quite similar detection performances. In order to evaluate parameter estimation performances of each beamformers, the Cramer Rao Lower Bound analysis is performed. It is seen that both beamformers provide similar results especially when DFT beams are placed with the appropriate angular intervals as in detection case. Hence, it can be inferred that for non-adaptive operations, both beamspace methods give close results to each other in terms of detection and parameter estimation criteria.

High clutter, chaff and jamming powers can degrade detection performance of the array and it is found out that low sidelobe pattern can eliminate these hazardous factors in a considerable manner. Hence, a well known spatial operation, array tapering, is employed together with subspace operation to handle with them. It is seen that conventional array tapering can be applied with subspace operation by weighting the data at the elements of the array and projecting them onto the beamspace matrix. However, in order to overcome with the non-reversible effect of conventional array tapering, which can be explained as deficiency in detection and parameter estimation performance, a new tapering method is developed to be employed in subspace. Tapering operations realized in element space and beamspace are called as tapering before and after dimension reduction, respectively. Pattern performance of these methods are analyzed and results show that tapering operation requires additional dimensions to be implemented properly. Besides, analysis performed in Section 4.3 demonstrated that both subspace tapering methods have different dimension requirements. It is observed that tapering before dimension reduction method needs less additional dimension than tapering after dimension reduction method. As expected, beam patterns with tapering before dimension reduction method converge to the desired tapered pattern rapidly since it uses full dimensional array information. In contrast, the pattern generated using tapering after dimension reduction method achieves the desired pattern after addition of several dimensions to the subspace basis. It is worthy of note that even though tapering before and after dimension reduction methods require additional channels to operate accurately, when the simulations are performed for a challenging scenario, it is shown that their detection success is better than non tapered beamspace method even if additional dimensions are not used. Moreover, in order to examine the robustness of the proposed methods, phase errors are applied to the array elements and it is observed that both tapering methods are robust against imperfections that can be experienced in practice. Overall, it is inferred that array tapering can be successfully applied with the dimension reduction operation.

Strong interferers entering from the sidelobes of the beam can cause major direction finding errors and tapering operation can be insufficient against such cases. Sidelobe blanker, which is a well-known spatial operation, is examined to deal with these type of interferences. Firstly, a new auxiliary antenna pattern configuration is proposed to overcome with the coupling between the probability of blanking and probablility of target blanking in conventional Maisel's structure. Moreover, the performance of conventional Maisel's sidelobe blanker method is evaluated with the suggested auxiliary pattern. It is seen that there is a drastic improvement for arrays having poor sidelobe to mainlobe ratios. Especially, when the threshold parameter is taken at its maximum, the performance improved in a considerable manner. However, it is noted that the contribution of the new auxiliary pattern to the performance of the sidelobe blanker becomes negligible with increasing peak to sidelobe ratio of the array pattern.

Secondly, the subspace implementation of sidelobe blanker is investigated and it is seen that the conventional sidelobe blanker method needs an additional auxiliary antenna to identify the interferers entering from the sidelobe. However, it is shown that auxiliary antenna pattern can also be designed in subspace by optimizing the combinations of the subspace basis vectors in a convenient manner.

Finally, implementation of both tapering and sidelobe blanking together with dimension reduction is studied and it is seen that both operations can be performed in subspace without any need for and additional channel. It is inferred that the dimensions required for tapering operation is sufficient to design properly functioning tapering and sidelobe blanking structures in subspace.

6.2 Future Work

Some research topics that could not be investigated within the scope of this thesis are listed as follows:

1. Effect of multipath on subspace based detection and estimation performance.
2. Implementation of adaptive beamforming methods (such as MVDR and Capon) in reduced dimensions together with array tapering and sidelobe blanking methods.
3. Evaluation of the detection and estimation performance of subspace after employing the adaptive beamforming methods.

REFERENCES

[1] H. L. Van Trees, *Optimum array processing.* New York: Wily-Interscience, 2002.

[2] B. D. Van Veen and B. G. Williams, "Dimensionality reduction in high resolution direction of arrival estimation," in *Proceedings of Asilomar Conference on Signals, Systems and Computers.* IEEE, 1998.

[3] P. Forster and G. Vezzosi, "Application of spheroidal sequences to array processing," in *Proceedings of International Conference on Acoustics, Speech, and Signal Processing*, vol. 12. IEEE, 1987, pp. 2268–2271.

[4] D. Slepian, "Prolate spheroidal wave functions, fourier analysis, and uncertainty—V: the discrete case," *The Bell System Technical Journal*, vol. 57, no. 5, pp. 1371–1430, May-June 1978.

[5] M. Viberg and B. Ottersten, "Sensor array processing based on subspace fitting," *IEEE Transactions on Signal Processing*, vol. 39, no. 5, pp. 1110–1121, May 1991.

[6] S. Anderson, "Optimal dimension reduction for sensor array signal processing," in *Proceedings of Asilomar Conference on Signals, Systems, and Computers*, vol. 2. IEEE, 1991, pp. 918–922.

[7] P. Stoica and A. Nehorai, "Mode, maximum likelihood and Cramer-Rao bound: bonditional and unconditional results," in *Proceedings of International Conference on Acoustics, Speech, and Signal Processing.* IEEE, 1990.

[8] B. Van Veen and B. Williams, "Structured covariance matrices and dimensionality reduction in array processing," in *Proceedings of Fourth Annual ASSP Workshop on Spectrum Estimation and Modeling.* IEEE, 1988, pp. 168–171.

[9] M. G. Guvensen, C. Candan, S. Koc, and U. Orguner, "On generalized eigenvector space for target detection in reduced dimensions," in *Proceedings of IEEE Radar Conference.* IEEE, 2015, pp. 1316–1321.

[10] C. W. Therrien, *Discrete Random Signals and Statistical Signal Processing.* New Jersey: Prentice Hall, 1992.

[11] C. A. Balanis, *Antenna theory, analysis and design.* New York: John Wiley & Sons, 1997.

[12] A. Farina, *Antenna-based signal processing techniques for radar systems.* London: Artech House, 1992.

[13] M. A. Richards, J. A. Scheer, and W. A. Holm, *Principles of modern radar: basic principles.* London: Artech House, 1992.

[14] M. I. Skolnik, *Introduction to radar systems*, 2nd ed. New York: McGraw-Hill, 1980.

[15] G. M. Guvensen and F. Canatan, *Tapered beamforming*, April 2015.

[16] L. Maisel, "Performance of sidelobe blanking systems," *IEEE Transactions on Aerospace and Electronic Systems*, vol. AES-4, no. 2, pp. 174–180, March 1968.

[17] D. H. Harvey and T. L. Wood, "Designs for sidelobe blanking systems," in *Proceedings of IEEE Radar Conference.* IEEE, 1980, pp. 410–416.

[18] M. R. O'Sullivan, "A comparison of sidelobe blanking systems," in *Proceedings of IEEE Radar Conference.* IEEE, 1987, pp. 345–349.

[19] A. Farina and F. Gini, "Calculation of blanking probability for the sidelobe blanking for two interference statistical models," *IEEE Signal Processing Letters*, vol. 5, no. 2, pp. 98–100, April 1998.

[20] O. Coskun and C. Candan, "Design of maisel sidelobe blankers with a guarantee on the gap to optimality," *IET Radar, Sonar & Navigation*, vol. 10, no. 9, pp. 1619–1626, December 2016.

[21] A. Koc, "Spectral estimation lecture notes," METU, Ankara, 2015.

[22] E. T. Tuncer, "Sensor array signal processing lecture notes," METU, Ankara, 2015.

[23] R. M. Gary, *Toeplitz and circulant matrices: a review.* Delft: now, 2006.

[24] A. V. Oppenheim, R. W. Schafer, and J. R. Buck, *Optimum array processing*, 2nd ed. New Jersey: Prentice Hall, 1999.

[25] P. Rajmic, Z. Prusa, and C. Wiesmeyr, "Computational cost of chirp z-transform and generalized goertzel algorithm," in *Proceedings of the 22nd European Signal Processing Conference (EUSIPCO).* IEEE, 2014.

[26] L. Rabiner, R. Schafer, and C. Rader, "The chirp-z transform algorithm," *IEEE Transactions on Audio and Electroacoustics*, vol. 17, no. 2, pp. 86–92, June 1969.

[27] D. H. Bailey and P. N. Swarztrauber, "The fractional fourier transform and applications," in *SIAM Review*, vol. 33, 1991, pp. 389–404.

[28] W. T. Patton, "Low sidelobe antennas for tactical radars," in *Proceedings of IEEE Radar Conference*. IEEE, 1980, pp. 243–247.

[29] H. E. Schrank, *Aspects of modern radar*. Norwood: Artech House, 1988, ch. Low-sidelobe phased array and reflector antennas.

[30] A. Farina and F. Gini, "Design of SLB systems in the presence of correlated ground clutter," *IEE Proceedings on Radar, Sonar and Navigation*, vol. 147, no. 4, pp. 199–207, August 2000.

[31] F. Bandiera, A. Farina, D. Orlando, and G. Ricci, "Detection algorithms to discriminate between radar targets and ECM signals," *IEEE Transactions on Signal Processing*, vol. 58, no. 12, pp. 5984–5993, September 2010.

[32] P. Swerling, "Probability of detection for fluctuating targets," *IRE Transactions on Information Theory*, vol. 6, no. 2, pp. 269–308, April 1960.

[33] H. L. Van Trees, *Detection, Estimation and Modulation Theory Part 1*. John Wiley & Sons, 1968.